博士論文

Suction vortices in a pump sump
~ their origin, formation and dynamics ~
（ポンプ吸込水槽における吸込渦の起源、形成およびダイナミクス）

Yoshinobu Yamade
（山出吉伸）

Dissertation Advisor: Chisachi Kato
（指導教員：加藤千幸）
The University of Tokyo
2019

ACKNOWLEDGEMENTS

Firstly, I would like to express my sincere gratitude to Prof. Chisachi Kato, who is my dissertation advisor in Institute of Industrial Science, The University of Tokyo. He has been giving me grateful directions and motivating me motivations in researches and/or projects since 2001. I am deeply grateful for his kind and thoughtful directions, especially in this research.

I would like to express my sincere gratitude to Prof. Jun Matsui in Faculty of Engineering, Yokohama National University and Dr. Takahide Nagahara in Hitachi Industrial Products, Ltd. They have been giving me grateful directions about suction vortices in a pump sump in this research.

I would like to express my sincere gratitude to many researchers in academic institutes and industrial companies, and co-workers in Mizuho Information & Research Institute, Inc. The flow solver, originally developed by Prof. Chisachi Kato, which was used in this study has been developed and validated with grateful helps in collaborations with them.

This research used computational resources of K computer provided by the RIKEN Advanced Institute for Computational Science through the HPCI System Research project (Project ID: hp170258, hp180190 and hp190153). I would like to thank to those involved in the K computer Project.

Finally, I would like to thank to my family (my wife and two sons) who have helped me for long years.

TABLE OF CONTENTS

NOMENCLATURE

C_{u}	Tangential velocity (m/s)
C_{z}	Vertical (axial) velocity (m/s)
C_{u0}	Maximum tangential velocity given at the inlet boundary of the simplified computational model (m/s)
C_{z0}	(Uniform) axial velocity given at the inlet boundary of the simplified computational model (m/s)
$C_{\mathrm{u0_{base}}}$	Maximum tangential velocity given at the inlet boundary of the simplified computational model of baseline case 2 (m/s)
$C_{\mathrm{z0_{base}}}$	(Uniform) axial velocity given at the inlet boundary of the simplified computational model of baseline case 2 (m/s)
$\mathrm{C_S}$	Smagorinsky coefficient [-]
D_{b}	Opening diameter of bellmouth (mm)
D_{p}	Diameter of outlet (suction) pipe (mm)
F_{D}	Froude number defined by average velocity at, and diameter of, bellmouth [-]
h	Water depth (mm)
h_1	Height under bellmouth inlet (mm)
h_2	Submergence of bellmouth inlet (mm)

$\mathrm{d}P$	Static pressure drop at the vortex core (Pa)
$\mathrm{d}C_{\mathrm{P}}$	Static pressure drop at the vortex core normalized by the dynamic pressure, $\frac{1}{2}\rho C_{\mathrm{u0}}^2$ [-]
P	Static pressure (Pa)
R	Radius [-]
R_0	Radius where the tangential velocity takes its maximum value (vortex-core radius) [-]
R_{e}	Initial Reynolds number defined by $R_{\mathrm{e}} \equiv \frac{C_{\mathrm{u0}} R_0}{\nu}$ [-]
S	Initial swirl number defined by $\mathrm{S} \equiv \frac{\int_0^{\mathrm{R_0}} 2\pi r^2 C_{\mathrm{z0}} C_{\mathrm{u}} \mathrm{d}r}{\int_0^{\mathrm{R_0}} 2\pi r \mathrm{R_0} C_{\mathrm{z0}} C_{\mathrm{z0}} \mathrm{d}r} = \frac{C_{\mathrm{u0_{base}}}}{C_{\mathrm{z0_{base}}}} \times \frac{\alpha}{2\beta}$ [-]
S_{ij}	Rate of strain (1/s)
t	Time (s)
u, v, w	Velocity components, respectively, in main-stream, lateral direction and vertical directions (m/s)
u_{i}	Velocity components, respectively, in x_{i} directions (m/s)
u_{in}	Inlet velocity of pump sump (m/s)
u_b	Average velocity at bellmouth inlet (m/s)
W	Width of pump sump (mm)
$\mathrm{X}, \mathrm{Y}, \mathrm{Z}$	Coordinates, respectively, in main-stream, lateral direction and vertical directions (mm)

x_{i}	Cartesian coordinates (mm)
α	C_{u0} normalized by that in baseline case 2 [-]
β	C_{z0} normalized by that in baseline case 2 [-]
Δ	Width of the grid-scale filter (m)
ν	Kinematic viscosity of the working fluid (water) (m^2/s)
ν_{SGS}	Sub-grid scale kinematic viscosity of the working fluid (water) (m^2/s)
ρ	Density of the working fluid (water) (kg/m^3)
$\omega_{\mathrm{x}}, \omega_{\mathrm{Y}}, \omega_Z$	Vorticity components, respectively, in main-stream, lateral direction and vertical directions (1/s)

LIST OF FIGURES

LIST OF TABLES

Abstract

Their origin, formation mechanism, and dynamics have been clarified by large-eddy simulation (LES) applied to two different computational models for suction vortices that appear in a pump sump. The first one is a pump-sump model composed of a 2,610 mm-long water channel of rectangular cross section with a width of 300 mm and a water depth of 100 mm and a vertical suction (outlet) pipe with a 100 mm diameter installed at its downstream end. At the upstream end of the channel, a uniform velocity of 0.37 m/s is given, and 2 billion hexahedral elements with maximum resolution of 0.225 mm are applied to the whole model pump-sump. LES with different wall boundary conditions have revealed that the origin of a submerged vortex is the mean shear of the approaching boundary layers that develop on the bottom and side walls of the pump sump. Detailed investigations of flow fields computed for a long time period have revealed that deviation of the mean flow that approaches under the suction pipe triggers conversion of the axis of the vorticity that is originally aligned to the lateral direction in the approaching boundary layers to that aligned to the vertical direction. The local acceleration of the vertical flow stretches the afore-mentioned vertical vortex, which results in formation of a submerged vortex. The separated flows downstream of the suction pipe generate vertical vorticity and forms an air-entrained vortex when such a vortex is sucked into the suction pipe. The second one is a simplified computational model composed of a paraboloid of revolution and aims to accurately simulate the stretch of the viscous core of a submerged vortex that has appeared under the suction pipe of the pump-sump model. It has a much higher grid resolution of 15 micrometres. While the viscous core of the submerged vortex computed by the whole pump-sump model has only reduced to a minimum radius of 3 mm and the minimum pressure has decreased by only 5 kPa, that computed by the simplified model has reduced to a minimum radius of 0.75 mm and the minimum pressure has decreased by as much as 100 kPa. This implies that cavitation could have been initiated in the viscous core, if it had been taken into account, as is observed in the pump-sump experiment at the same condition. Parametric studies with different initial swirl numbers varied from 0.12 to 16.3 have clarified the behavior of a submerged vortex. It is

found that a strong submerged vortex appears only at a relatively small range of the swirl-number from 1.25 to 3.

Chapter 1. Introductions

Submerged vortices and air-entrained vortices (hereafter, they are referred to as “suction vortices”) that appear in a pump sump may cause noise and vibrations, and at the worst case, damage the pump system. In particular, increase in the approaching flow velocity, which is often times adopted for reducing the construction cost of a pump sump, significantly increases the risk for suction vortices to be formed. Therefore, at an early stage of its design, occurrence of the suction vortices must be considered for a pump sump.

Occurrences of suction vortices have been conventionally evaluated by model pump-sump experiments. By recent speedup of high-end computers, numerical methods have also been applied to the prediction of the suction vortices in a pump sump. Table 1 lists the numerical investigations of pump-sump flows published recently. Ansar et al. measured the velocity fields in a test pump sump by Acoustic Doppler Velocimeter (ADV) [1], and they showed that a potential-flow analysis could predict the flow patterns in the test pump sump [2] (see Figure 1.1). Reynolds Averaged Navier-Stokes Simulation (RANS), which is a method on a time-average basis, has been mainly adopted [3-6]. In computations based on RANS, occurrence of suction vortices is judged typically by visualizing streamlines, distribution of the static pressure and/or that of the vorticity for the computed steady flow field. Constantinescu et al. investigated accuracy of the flow fields in a test pump sump predicted by several two-equation RANS models, all based on linear eddy viscosity model [3]. Okamura et al. performed benchmark tests by model-sump experiments and numerical simulations based on several RANS turbulence models [4] and identified those conditions under which submerged and/or air-entrained vortices occurred in their experiments. Shin investigated the effects of the flow rate and the water level on air-entrained vortices by measurements and numerical simulations based on k-omega SST turbulence model and a Volume of Fraction (VOF) method. He showed that a larger flow rate and a lower water level enhanced generations of air-entrained vortices [5]. Wu et al. also performed VOF computations of three pump-sump flows with different flow rates and water levels combined with Detached Eddy Simulation (DES) and unsteady RANS [6]. They showed that DES had

a better accuracy for predicting the internal flow and the free surface of the pump sumps because DES could capture dynamics of energetically important eddies in the pump-sump. With a few exceptions described shortly, most of the recent numerical investigations of a pump-sump flow found in the literature adopted two-equation RANS turbulence models. However, as Strasser pointed out in [7], this class of turbulence model has a shortcoming that it lacks in the ability to accurately represent the anisotropic nature of turbulence caused by a strong curvature of the streamlines and/or rapid changes in the strain rate, both of which seem crucial in a pump-sump flow.

A time-averaged method may become a useful tool for evaluating the possibility of suction vortices occurrence because it can compute relatively large-scale flow structures that depend on the geometries of a pump sump, and the occurrence of suction vortices are presumably determined by such flow structures. However, it is less likely that a time-averaged method can accurately predict the behavior of suction vortices, which are essentially in unsteady motion, and it is obvious that appearance or disappearance of suction vortices cannot be predicted by such a time-average method.

As a more advanced numerical method, a Large-Eddy Simulation (LES) approach has also been applied to the prediction of the unsteady flows in a pump sump [8-11]. Computations with LES have realized better predictions of the velocity fields of the approaching flow in pump sumps and succeeded in predicting unsteady suction vortices. For example, Qiang et al showed that the locations, shapes and sizes of suction vortices could be predicted by comparing measurements and flow fields computed by LES. They found secondary vortex were generated around primary vortex by analyzing dynamics of vortices motions (see Figure 1.2).

As mentioned above, RANS approach has successfully presented suction vortices occurrence, and LES approach could simulate dynamic of suction vortices. However, neither the fundamental origin of suction vortices nor their formation/dissipation processes have been clarified in the previous reports. The objective of this research is to clarify the origin, formation/dissipation and dynamics of suction vortices in a pump sump. As will be shown in this paper, it is also essential to capture the dynamics of the viscous vortex core to accurately predict the velocity profile and the static-pressure drop in a suction vortex, which requires use of a very high grid resolution. For using high grid resolution , we perform LES using a

computational grid of up to 2 billion grids, which is about hundred times larger than the latest other researches (Table 1.1), in this research.

To further investigate suction vortices in a pump sump, Wall-Resolved Large-Eddy Simulations (WR-LES), which uses a maximum of 2 billion grids, have been applied to two different computational models in the present study. The first one is a pump-sump model. LES performed for a long period of time with different wall boundary conditions have clearly identified the origin and formation process both of a submerged vortex and an air-entrained vortex. The second one is a simplified computational model composed of a paraboloid of revolution and aims to accurately simulate the stretch of the viscous core of a submerged vortex that has appeared under the suction pipe of the above-mentioned pump-sump model. It has a much higher grid resolution than the pump-sump model and can resolve the dynamics of the viscous core of a submerged vortex. Parametric studies with different initial swirl numbers varied from 0.12 to 16.3 have clarified the behavior of a submerged vortex, and those condition under which a strong submerged vortex is formed.

Table 1.1. Numerical investigations of pump-sump flows published recently [2-6, 8-11].

Authors	Year	Turbulence Model	Free-surface Method	Number of Grids	Reference No.
Ansar et al.	2002	Inviscid	-	7.8×10^4	[2]
Constantinescu et al.	2000	RANS	-	5.5×10^5	[3]
Okamura et al.	2007	RANS	-	2.7×10^6	[4]
Shin	2018	RANS	VOF	8.5×10^5	[5]
Wu et al.	2019	RANS/DES	VOF	6.7×10^6	[6]
Tokyay et al.	2006	LES	-	5.0×10^6	[8]
Nakayama et al.	2010	LES	-	4.6×10^5	[9]
Chuang et al.	2014	LES	VOF	2.0×10^6	[10]
Qiang et al.	2019	LES	-	1.2×10^7	[11]

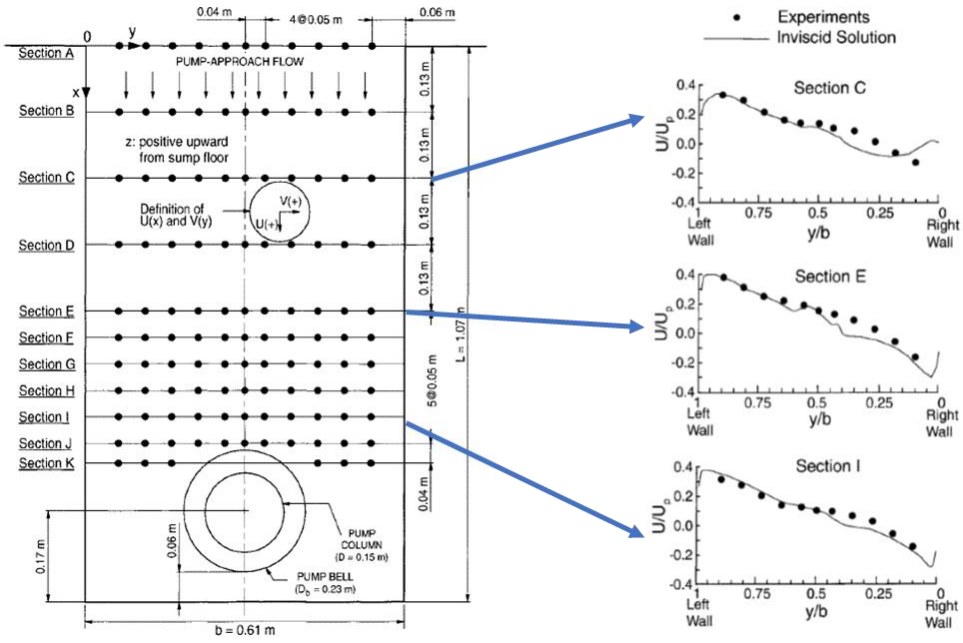

Figure 1.1. Measurement points of velocity (left) and comparison of velocity profiles (right) in a pump sump model [1, 2].

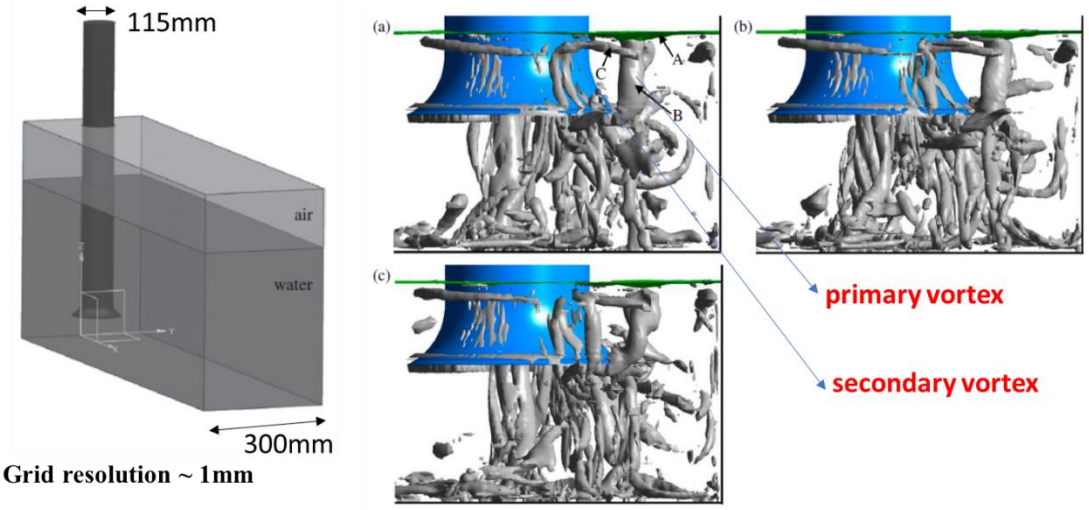

Figure 1.2. Computational model (left) and vortices structures visualized by the 2nd invariance (right) computed by large-eddy simulation [11].

Chapter 2. Prediction Methods

The unsteady flows in a pump-sump model and a simplified model, which will be explained in detail, respectively, in "Chapter 3 Origin and Formation of Suction Vortices" and "Chapter 4 Dynamics of a Submerged Vortex", is predicted by solving numerically the continuity and Navier-Stokes equations of an incompressible fluid for spatially filtered velocity components and static pressure as shown below:

$$\frac{\partial \bar{u}_\mathrm{i}}{\partial x_\mathrm{i}} = 0 \tag{1}$$

$$\frac{\partial \bar{u}_\mathrm{i}}{\partial t} + \frac{\partial}{\partial x_\mathrm{j}}(\bar{u}_\mathrm{i}\bar{u}_\mathrm{j}) = -\frac{1}{\rho}\frac{\partial \bar{p}}{x_\mathrm{i}} + \frac{\partial}{\partial x_\mathrm{j}}\left\{(\nu + \nu_\mathrm{SGS})\left(\frac{\partial \bar{u}_\mathrm{i}}{\partial x_\mathrm{j}} + \frac{\partial \bar{u}_\mathrm{j}}{\partial x_\mathrm{i}}\right)\right\} \tag{2}$$

where $\bar{u}_i$are the grid-scale velocity components represented in the Cartesian coordinates and $\bar{p}$ is the grid-scale static pressure. ρ and ν respectively denote the density and kinematic viscosity of the fluid. ν_{SGS} is the sub-grid scale eddy viscosity and modeled after Smagorinsky as follows:

$$\nu_\mathrm{SGS} = (\mathrm{C_S}\Delta)^2(2\bar{S}_\mathrm{ij}\bar{S}_\mathrm{ij})^{0.5} \tag{3}$$

$$\bar{S}_{ij} = \frac{1}{2}\left(\frac{\partial \bar{u}_i}{\partial x_j} + \frac{\partial \bar{u}_j}{\partial x_i}\right) \tag{4}$$

where $\bar{S}_{ij}$ denotes the rate of strain, and Δ is the width of the grid-scale filter. Smagorinsky coefficient, C_s, is computed as a function of time and space, based on the Dynamic Smagorinsky Model (DSM), originally proposed by Germano et al. [12], and later modified by Lilly [13]. DSM has been known to have a problem associated with its numerical instability, which is primary caused by negative values computed for the Smagorinsky

coefficient, C_s, by this model. Several methods to avoid this numerical instability associated with DSM have been proposed in the literature, which includes to clip a negative value of C_s (lower-bound C_s by zero) [14] and to apply spatial averaging to C_s [15]. In the present application of DSM, local (spatial) averaging is first applied to the values of C_s computed by DSM and second clipping is also applied after the local averaging is done.

As mentioned already, one of the objectives of the present study is to clarify the dynamics of the viscous core of a submerged vortex. The work done to the viscous core primarily balances the sum of the increase in the kinetic energy and dissipation to heat. The minimum radius of the viscous core is realized when all the work done to the viscous core balances the dissipation. With this regard, the sub-grid scale eddy viscosity should appropriately be dampened in the viscous core region, which, we have confirmed, is achieved by the DSM.

For solving the above-mentioned set of equations, we use Front Flow/ Blue (FFB), a general-purpose LES solver based on the Finite Element Method (FEM) and developed by one of the authors, Kato et al. [16, 17]. The fractional-step method is applied to solve for the pressure, and the Crank–Nicholson method is used to integrate the spatially-filtered Navier-Stokes equations for implicit time march. The numerical method has the second-order accuracy both in space and time. Detailed descriptions on the flow solver are given by Kato et al. [16, 17]. The leading truncating error associated with a second-order scheme in space is, in general, the third-order dispersion error, namely, error in the phase velocity. Dispersion error often times become a serious problem, in particular, for computing propagation of sound waves. For such a case, spectral methods [e.g. 18] and/or a high-order compact scheme [19] are often times used because these methods produce no or little dispersion/dissipation errors. It is, however, difficult to apply a spectral method or a high-order compact scheme to industrial problems with complicated geometries as in the present study. On the other hand, we have proved, through many applications to various engineering flows, that LES with second-order accuracy both in time and space can produce a solution with a satisfactory accuracy if the numerical grids are sufficiently fine to adequately resolve the turbulent eddies responsible to the production of turbulence in the boundary layer. These applications include turbomachinery flows [20, 21], automobile flows [22, 23], ship-hydrodynamics flows and others [24, 25, 26]. The use of the second-order method to the present numerical investigations thus can be justified.

A submerged vortex formed in the model pump sump as well as in actual pump sumps is normally identified by occurrence of cavitation in its core region, which may also be influenced by the air resolved in the water to a certain extent. On the other hand, air is entrained in the core of an air-entrained vortex as its name implies. In the present study, however, we investigate the drop of the static pressure due solely to the vortical dynamics by applying single-phase LES, and neither the effects of cavitation nor the free-surface is taken into account. These effects on the vortical dynamics still remain as an open question.

Chapter 3. Origin and formation of suction vortices

As mentioned above, the origin and formation mechanism of suction vortices that appear in a pump sump will firstly be investigated by large-eddy simulations applied to a model pump sump, which will be described in this section.

3.1 Model Pump Sump and Operating Condition

The model pump sump that Okamura et al. examined [4] is set as the benchmark case in the present study. Figure 3.1 and Table 3.2, respectively, show the specifications of the model pump sump and photos of the experimental apparatus together with suction vortices visualized in their experiment [4]. Among those cases studied by Okamura et al. [4], the operation condition with an inlet velocity u_{in} of 0.37 m/s and the water depth h of 150 mm is selected in the present study. The opening diameter of the bellmouth, D_b , is 150 mm, and the average inlet velocity there, u_b, is 0.94 m/s, except for Cases E and F, which results in the Froude number F_D, defined by the opening diameter of the bellmouth and the average velocity there, of 0.78. Hereafter, the non-dimensional length normalized by using the opening diameter of the bellmouth (D_b=150 mm) will also be presented for reference. The height under the bellmouth inlet, h_1, is set to 100 mm ($0.67\,D_b$), and therefore, the submergence of the bellmouth inlet, h_2 (the distance between the bellmouth inlet and the water surface) is 50 mm ($0.33D_b$). For this condition, both submerged and air-entrained vortices are confirmed to take place in their experiment [4]. In addition to this case, a large-eddy simulation with a different height under the bellmouth inlet, h_1, and that with a different submergence of the bellmouth inlet, h_2, are performed in order to confirm the formation processes of suction vortices that have been identified in this study.

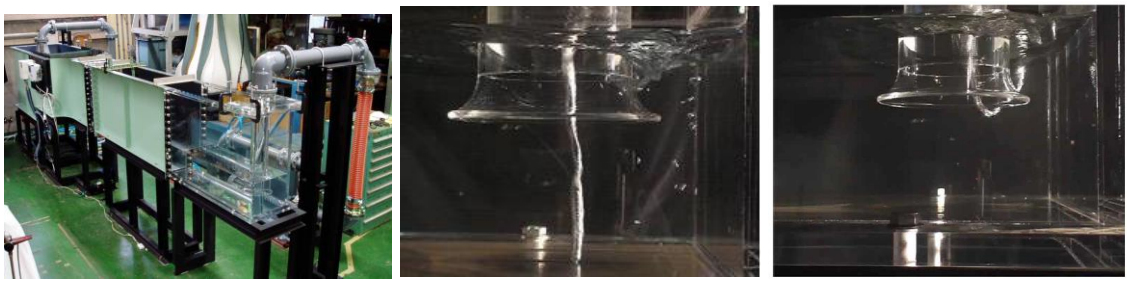

Figure 3.1. Model pump sump (left) and visualized submerged (middle) and air-entrained (right) vortices taken from Okamura et al., 2007 [4].

Table 3.2. Specifications of test pump sump.

Diameter of bellmouth opening D_b	150 mm
Diameter of outlet (suction) pipe D_p	100 mm ($0.67D_\mathrm{b}$)
Width of pump sump W	300 mm ($2.00D_\mathrm{b}$)
Water depth h	150 mm ($1.00D_\mathrm{b}$)
Height under bellmouth inlet h_1	100 mm ($0.67D_\mathrm{b}$)
Submergence of bellmouth inlet h_2	50 mm ($0.33D_\mathrm{b}$)
Inlet velocity of pump sump u_in	0.37 m/s
Average velocity at bellmouth inlet u_b	0.94 m/s
Froude number F_D defined by D_b and u_b	0.78

3.2 Computational Model

Figure 3.2 shows the computational model of the pump sump. The X coordinate is set in parallel to the centerline of the rectangular channel, and its origin is set at the projected center of the axis of the suction pipe on the bottom of the channel. The Y, and Z axes are, respectively, set to the lateral and vertical directions. The inlet boundary is set at X=2,500 mm ($16.67\boldsymbol{D_b}$) where a uniform velocity of 0.37 m/s is prescribed as in the experiment. As shown in Figure 3.2-(c), the suction pipe is installed 110 mm ($0.73\boldsymbol{D_b}$) upstream of the back wall of the rectangular channel with an offset of 10 mm ($0.067\boldsymbol{D_b}$) in the positive Y direction. In the present study, the pump in the suction pipe is not modeled, and instead, out-flow boundary conditions are prescribed at the outlet of the suction pipe at a height of Z = 2,000 mm ($13.33\boldsymbol{D_b}$), where the fluid traction and the static pressure are both assumed to be zero. As can be seen in Figure 3.1, the experimental pump-sump model is composed of an open channel, and therefore, it has a free water surface at the top. In the present numerical investigations, however, the effects of the free water surface are not taken into account, and therefore, the effects of the gravity force are not considered, either. Instead, the slip boundary condition is given at the top boundary of the rectangular channel set at a height of Z = 150 mm ($1.00\boldsymbol{D_b}$). In the actual pump sump, the free water surface is most likely to influence the formation of an air-entrained vortex near the suction pipe. However, we believe that the origin and the formation mechanism of an air-entrained vortex, which will be identified and detailed in subsection “3. 9 Origin and Formation Mechanism of an Air-entrained Vortex”, is still valid at least to a certain extent. The no-slip boundary condition is given on the remaining boundaries of the computational model, namely, on the bottom, side, and end surfaces of the rectangular channel, and on the inner and outer surfaces of the suction pipe.

The Reynolds number defined by the uniform velocity given at the inlet boundary (=0.37 m/s) and the distance between the inlet boundary and the projected center of the axis of the suction pipe (=2,500 mm= $16.67D_b$) is approximately 1.0×10^6 with water at the ambient temperature. It is not certain if the boundary layers that develop on the bottom and side walls of the rectangular channel have become turbulent by the time when they approach

the suction pipe in the model pump-sump experiment, and therefore, both laminar boundary layer and turbulent boundary layer are considered in the present study. For the latter, at the bottom and side walls of the rectangular channel, the boundary layers are trapped by a step with a height of 5 mm ($0.033D_b$) and a width of 5 mm ($0.033D_b$) installed 300 mm ($2.00D_b$) downstream of the inlet boundary. Figure 3.3-(a) shows the computational mesh around the step. The height of the step is approximately the same as the thickness (4.5 mm=$0.03D_b$) of the approaching laminar boundary layer, estimated as being that of the Blasius solution [27] with an assumption that the pressure gradient in the main-stream direction is negligibly small. The size of the eddies of the production scale in the turbulent boundary layer is estimated as 2 mm ($0.013D_b$). The grid resolution of the present LES is 0.45 mm ($0.003D_b$) and 0.225 mm ($0.0015D_b$), which we believe is sufficiently fine to revolve the above-mentioned eddies in the turbulent boundary layers. Figure 3.3-(a) and 3-(b) show the computational grids, respectively near the bottom wall of the rectangular channel and near the bellmouth. For visibility, the computational mesh is shown every two and four grid lines, respectively, for the 0.45 mm ($0.003D_b$) resolution mesh and for the 0.225 mm ($0.0015D_b$) resolution mesh.

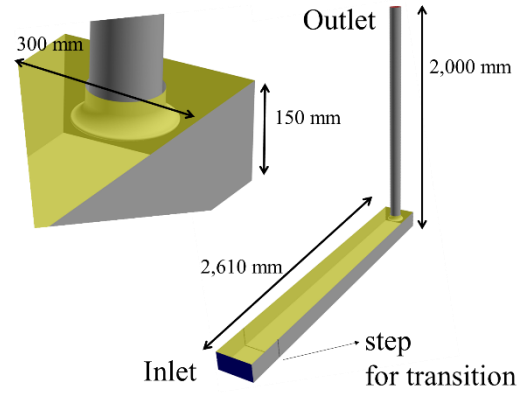

(a) Entire model and close-up view near bellmouth

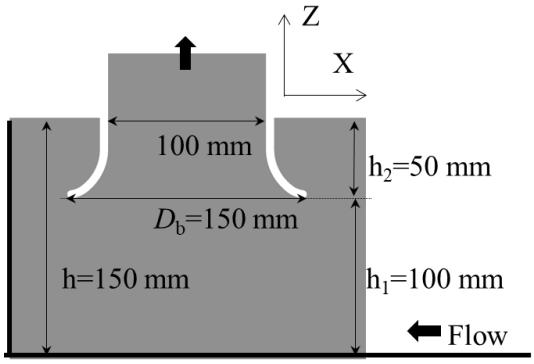

(b) X-Z section near the bellmouth

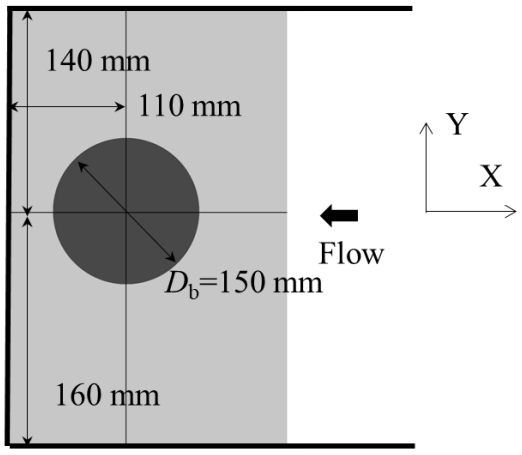

(c) X-Y section near the bellmouth

Figure 3.2. Computational model for LES of internal flows of test pump sump.

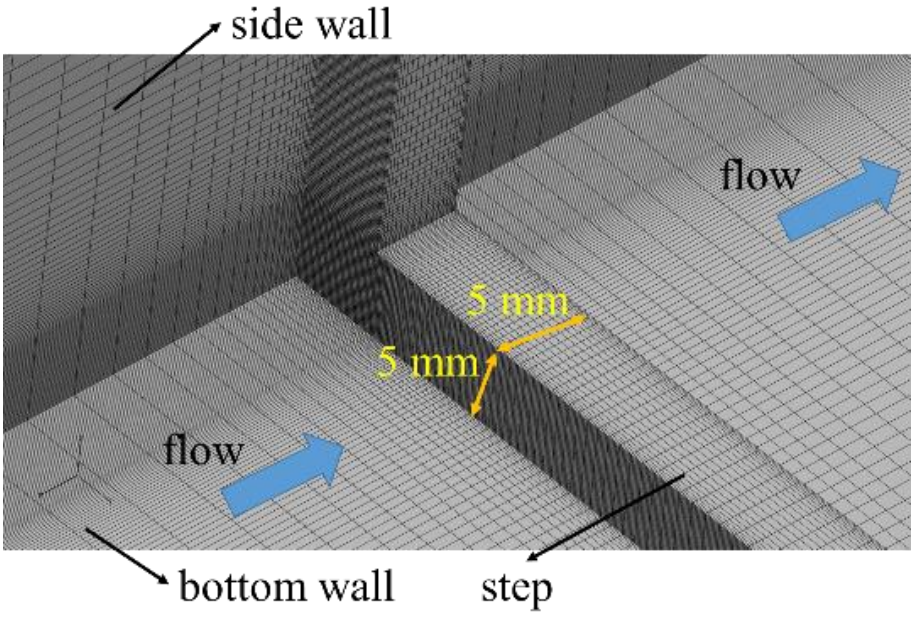

(a) bottom and side wall near the step

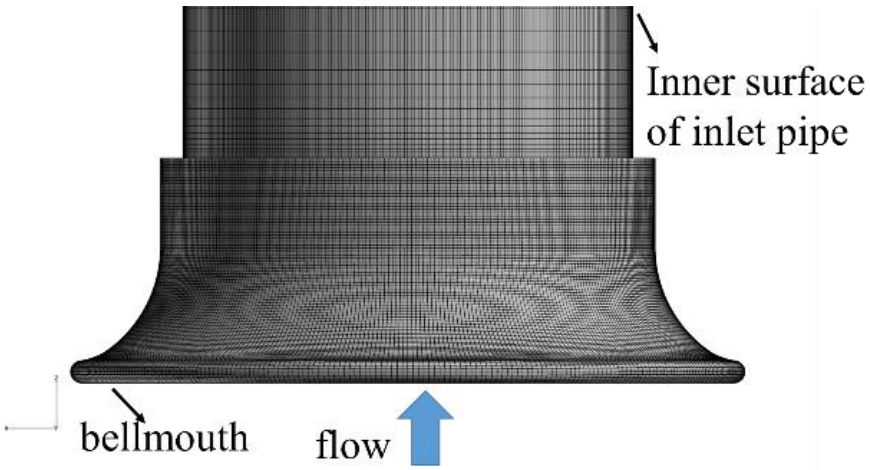

(b) bellmouth and intake pipe

Figure 3.3. Computational grids for LES of internal flows of test pump sump (thinning-out grids are plotted for visibility).

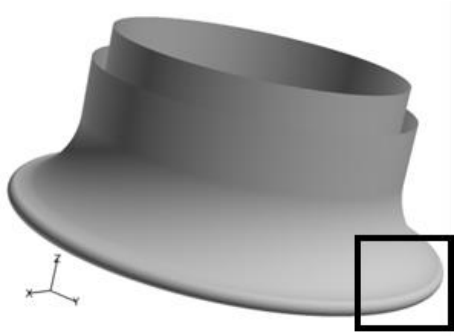

(a) Bellmouth

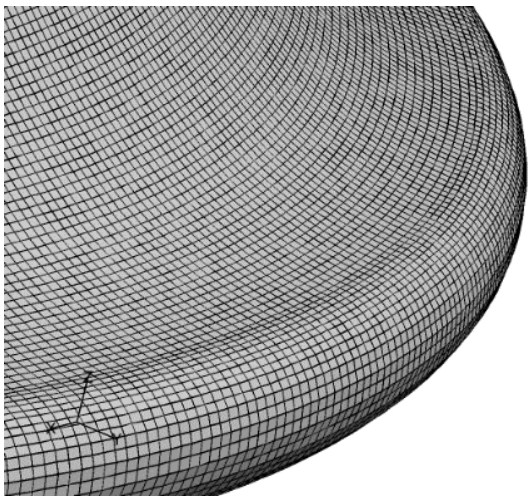

(b) Grids in Case A

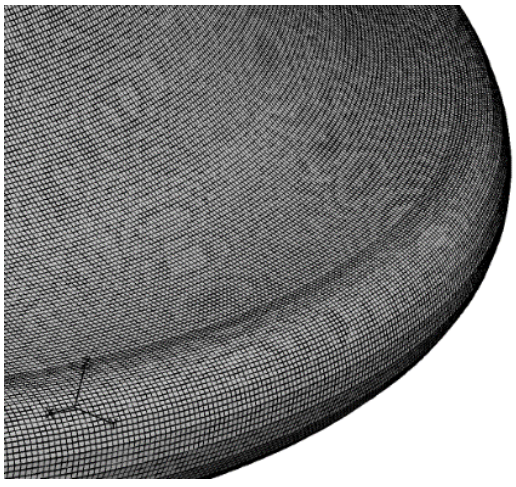

(c) Grids in Case D

Figure 3.4. Comparison of computational grids on bellmouth surface in Case A and Case D.

3.3 Computational Conditions

Table 3.3 summarizes all the cases studied by the large-eddy simulations for the pump sump. Case A is the baseline case and has a step to promote transition to turbulence, for which description has already been given. Case B does not have a step to prompt the boundary-layer transition, and therefore, the boundary layers on the bottom and side walls of the rectangular channel remain laminar until they approach the suction pipe. For Case C, the moving-wall boundary condition is set on the bottom and side walls of the rectangular channel, for which they move at the same velocity as the inlet velocity, and therefore, no boundary layer develops in this case. Cases A, B, and C are set for identifying the origin of a submerged vortex. In particular, by comparing the results obtained in Cases A and B, the contributions of the turbulent eddies in the approaching boundary layers to the formation of a submerged vortex will be identified. No turbulent eddies nor mean shear develop near the bottom and side walls in the rectangular channel for Case C, and therefore their contributions to the formation of a submerged vortex will be denied *if* a submerged vortex is formed in this case. Note that even in this case, the global shear that is caused by the asymmetry of the suction-pipe installation, as shown in Figure 3.2, exists.

The grid resolution is 0.45 mm ($0.003 D_b$) and identical for Cases A, B and C, which prevents effects of the grid resolution from influencing these results. The hexahedral elements are used in the present LES and the number of the elements is approximately 250 million in Cases A, B, and C. A time increment of 0.08 msec. is set for these cases. All the computations are continued for a time period of 3.2 seconds, which needed 40,000 time integrations (time steps) and corresponds to a non-dimensional time of 7.89 defined by the inlet velocity (0.37 m/s) given at the inlet boundary of the rectangular channel and the opening diameter of the bellmouth (150 mm), and occurrence of a submerged vortex and air-entrained vortex is investigated. In particular, the computation is continued for a longer time period of 16 seconds for Case A to investigate the appearance as well as the disappearance of the suction vortices.

All of the numerical investigations presented in this paper were made on "K-computer". K-computer was composed of 888,128 computing nodes (SPARC 64 VIIIfx), each of which accommodated 8 processing cores. One computing node had a theoretical peak performance of 128 GFLOPS. Cases A, B, and C took approximately 0.565 seconds per time step and these cases took a total of 6.3 hours for computing for 40,000 time steps with 4,092 computing nodes dedicated for each of the cases.

Case D has a twice-finer grid resolution than other cases and is intended to investigate the effects of the grid resolution on the behavior of the suction vortices. Finally, Cases E and F, respectively, have a different height under the bellmouth inlet, h_1, and a different submergence of the bellmouth inlet, h_2. These cases are set to confirm the formation processes of suction vortices that have been identified in this study, as already mentioned.

Table 3.3. Summary of test cases for pump-sump model LES.

Case Name	Num. of Grids	Grid Resolution	Approaching B.L.	h_1 [mm]	h_2 [mm]	Cal. Time [sec.]
Case A	0.25 billion	0.450 mm	Turbulent	100 ($0.67D_b$)	50 ($0.33D_b$)	16.00
Case B	0.25 billion	0.450 mm	Laminar	100 ($0.67D_b$)	50 ($0.33D_b$)	3.20
Case C	0.25 billion	0.450 mm	No B.L. (moving-wall)	100 ($0.67D_b$)	50 ($0.33D_b$)	3.20
Case D	2.00 billion	0.225 mm	Turbulent	100 ($0.67D_b$)	50 ($0.33D_b$)	0.34
Case E	0.25 billion	0.450 mm	Turbulent	150 ($1.00D_b$)	50 ($0.33D_b$)	0.65
Case F	0.25 billion	0.450 mm	Turbulent	100 ($1.00D_b$)	100 ($0.67D_b$)	0.65

3.4 Grid-independence Study

Although the grid resolution in all the cases is sufficiently fine to resolve the streamwise vortices in the turbulent boundary layers that develop (if they do) on the bottom and side walls of the rectangular channel, which used in Case D has twice finer grid resolution than other cases. By comparing results of Case A and Case D, for which all the computational conditions are identical and only their grid resolutions are different, the effects of the grid resolution on the behavior of the suction vortices will be identified. Figure 3.4 compares the surface grid near the bellmouth of the suction pipe for Case A and Case D. The grid size in the lateral direction is 0.225 mm ($0.0015D_{\mathrm{b}}$) and the number of the grids is approximately 2 billion in Case D. Figure 3.4-(b) and 4-(c) are enlarged view of the area enclosed by the rectangle in Figure 3.4-(a).

Computations both for Case A and Case D start from an identical flow field, in which a submerged vortex as well as two air-entrained vortices are confirmed to exist. Figure 3.5 compares an instantaneous flow field computed, respectively, by Case A (left) and Case D (right) after a sufficiently long period of time of 0.34 seconds has passed since their computations are initiated. By checking the temporal variations of the velocity components and the static pressure at several monitoring points set upstream of the suction pipe, it is confirmed that the flow computed for both Case A and Case D has reached, by this time, a statistically steady state. The instantaneous flow fields are visualized by iso-surfaces of the Laplacian of the static pressures colored by the vorticity component ω_{Z} in the vertical direction (hereafter, referred to as "vertical vorticity"). The value of the Laplacian of the static pressure used for iso-surface is 4.0×10^4 normalized by inflow velocity of 0.37 m/s and the width of the pump sump, 0.3 m in Figure 3.5. We confirmed that occurrence of suction vortices could be presented with the value of the normalized Laplacian of the static pressure between 1.0×10^4 and 1.6×10^5 (see Figure 3.6). Hereafter we will use the value 4.0×10^4 for iso-surface of the Laplacian of the static pressure in this paper. The vorticity normalized by the inflow velocity of 0.37 m/s and the width of the pump sump, 0.3 m will be presented, hereafter throughout in this paper. The vortex colored in blue rotates in the clockwise direction when it is viewed from the top (positive Z axis), (hereafter, the sense of rotation of

a vortex will be described when it is viewed from the top unless otherwise stated) and those in red do in the counterclockwise direction. The same method to visualize suction vortices will be used in the following figures, and therefore, their caption will be simplified as "visualized vortices". It is confirmed that essentially identical vortical structures are computed in Case A and Case D. Although not shown in a figure, no substantial difference is confirmed between the vortices visualized in Case A and those in Case D at other instances.

To quantitatively compare their results, Figure 3.7 shows, on its left, the distributions of the average tangential velocities on a horizontal plane at a height of 90 mm ($0.6D_{\mathrm{b}}$) from the bottom wall of the rectangular channel, obtained in Case A and Case D. The average is taken for the flow fields computed after the computed time of 0.34 seconds for both cases in the following manner. For each instantaneous flow field at this horizontal plane, the point where the static pressure is minimum is firstly identified and regarded as the center of the submerged vortex. Then, the tangential velocity at an individual radius is regarded as the circumferential velocity of the vortex and it is averaged in the circumferential direction as well as in time for 200 instantaneous flow fields separated by 4 msec interval.

As is inferred from Figure 6, the averaged distributions in the circumferential velocities obtained in Case A and Case D are essentially identical. Figure 3.8 compares the temporal variations of the minimum static pressure on the same horizontal plane computed in Case A and Case D. In the time period shown in this figure, a submerged vortex stably exists in both Case A and Case D, and therefore, the minimum static pressure appears at the center of the submerged vortex. The origin of the horizontal axis ($t = 0$) denotes the time when the computations are initiated from the given initial flow field. At $t = 0.16$ seconds, the minimum static pressures computed in Case A and Case D start to deviate, and that computed in Case D, which has a higher grid resolution, is lower by a maximum difference of about 600 Pa than that computed in Case A. This means that the submerged vortex is stretched more in Case D than in Case A. But, the drops in the static pressure are approximately 3 kPa in both cases, which is about only 3% of the atmospheric pressure.

From these grid-independence studies, it is concluded that the computational grid in Cases A, B, and C is sufficiently fine to predict large vortical structures that develop in the model pump sump, and to investigate the origin and formation/dissipation mechanism of the suction vortices. However, please recall that the generation of vapor phase, namely, the occurrence

of cavitation at the vortex core, is not taken into account. Therefore, even if the minimum static pressure becomes lower than the saturated vapor pressure at the ambient temperature, the viscous core would not expand, and the tangential velocity would not decrease. Meanwhile, the static pressure computed at the viscous core only reduces by 3% of the atmospheric pressure as already mentioned. This pressure drop is far smaller than the one for which the initiation of cavitation can be expected. The results from the grid-independence studies described above do not necessarily guarantee that the present numerical grid is sufficiently fine to accurately predict the stretch of the viscous core, and the stretch of the viscous core is most likely to have been underpredicted in the present large-eddy simulations applied to the whole pump-sump model. This can also be confirmed by the fact that the minimum static pressure computed in Case D is lower than that computed in Case A (see Figure 3.7) although the tangential velocities are almost the same for both cases (see Figure 3.8). The dynamics of the viscous core of a submerged vortex will be investigated in detail by the large-eddy simulations applied to the simplified computational model described in the next chapter.

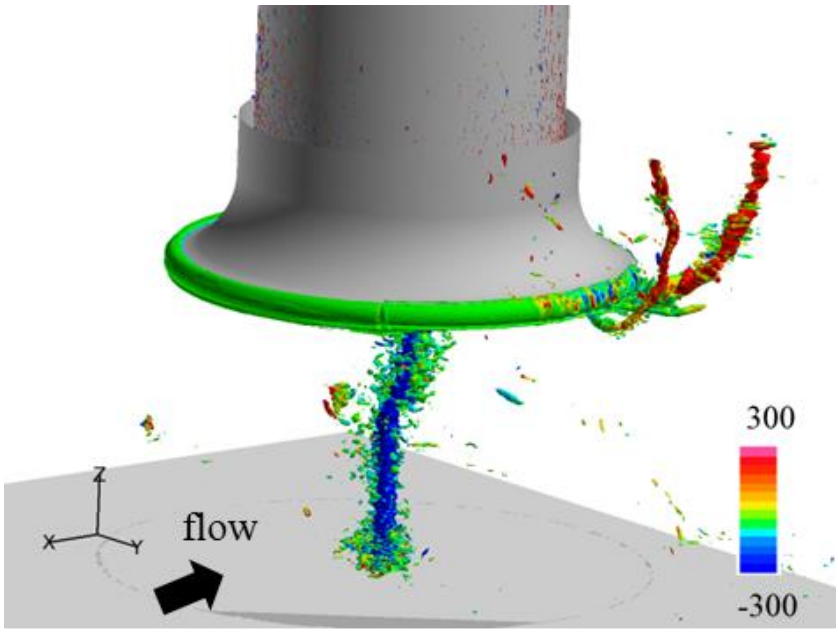

(a) Case A

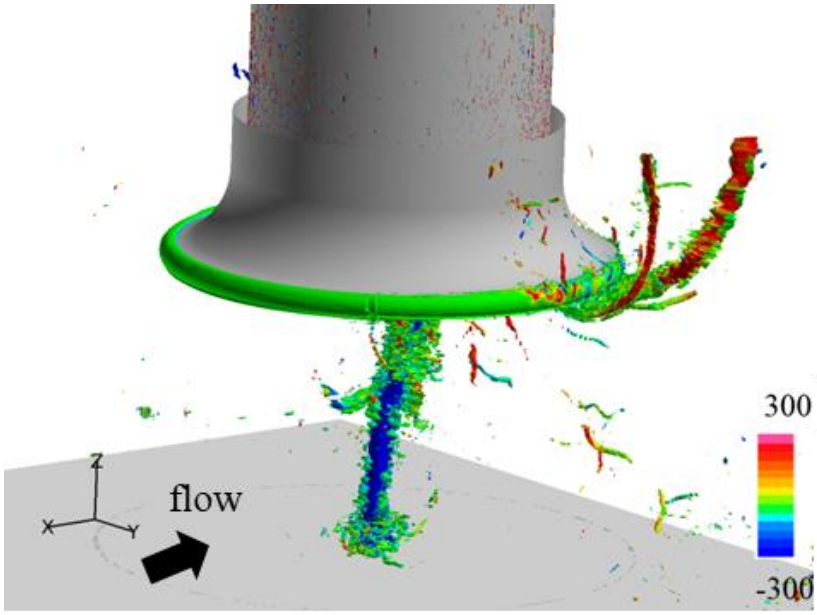

(b) Case D

Figure 3.5. Instantaneous flow fields visualized by iso-surfaces of Laplacian of static pressure colored by vertical vorticity computed for Case A (top) and Case D (bottom) at t= 0.34 sec..

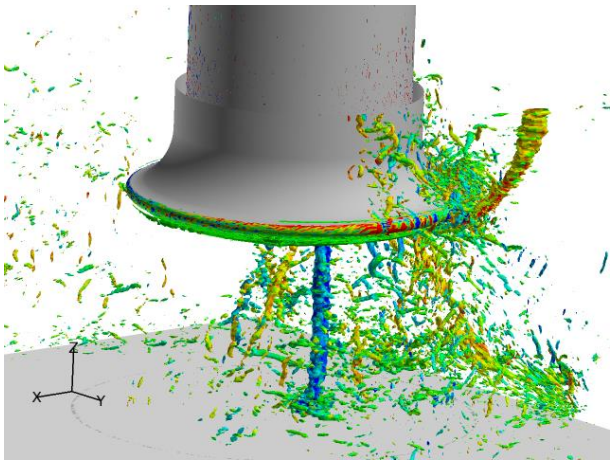

(a) $\Delta p = 1.0 \times 10^4$

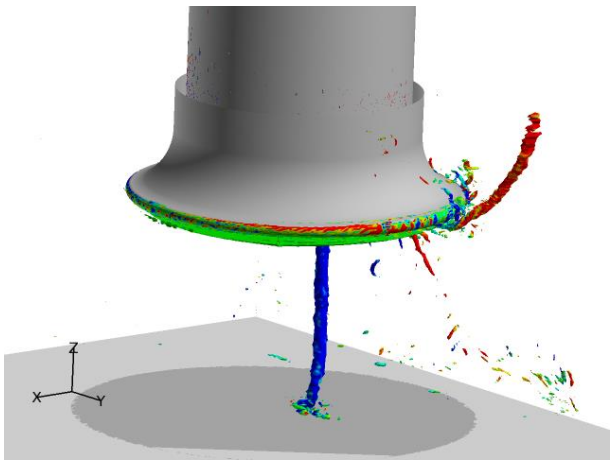

(b) $\Delta p = 4.0 \times 10^4$

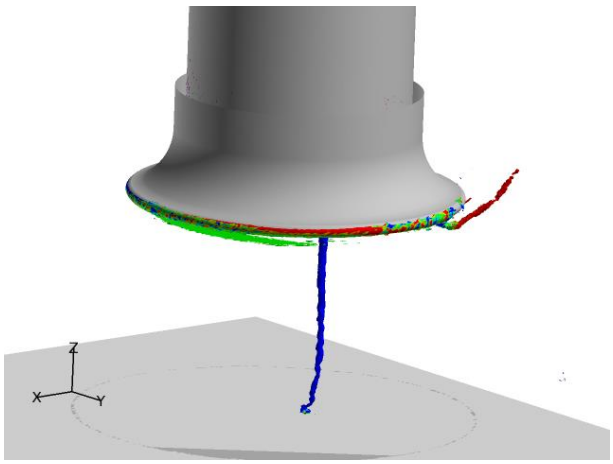

(c) $\Delta p = 1.6 \times 10^5$

Figure 3.6. Visualized suction vortices by iso-surface of Laplacian of pressure Δp with different its values in Case A.

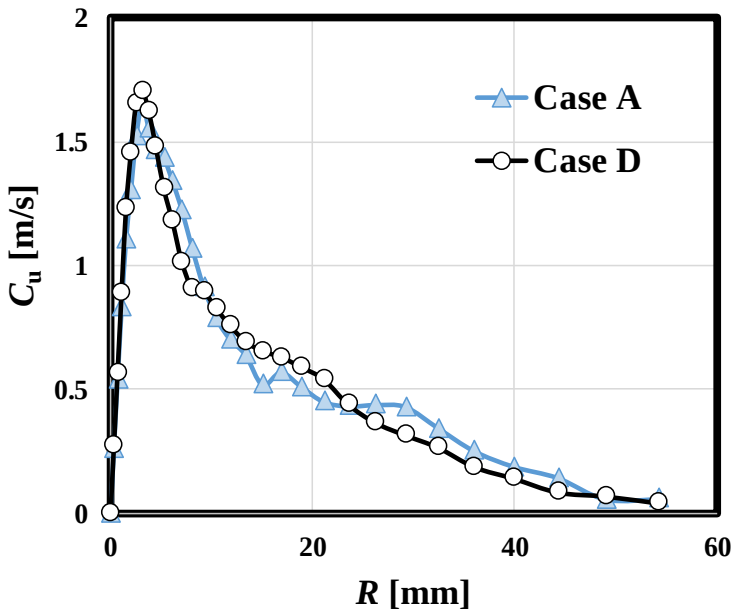

Figure 3.7. Averaged radial distributions of tangential velocity around center of a submerged vortex for Case A and Case D.

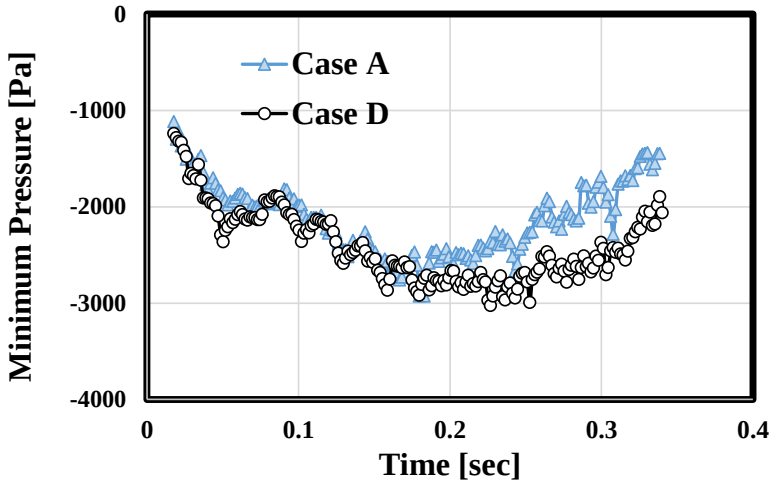

Figure 3.8. Temporal variation of minimum static pressure (right) computed on a horizontal plane 90 mm ($0.4D_b$) above the bottom wall of model pump sump for Case A and Case D.

3.5 Origin of a Submerged Vortex

As mentioned in “3.3 Computational Conditions”, Cases A, B, and C have different wall boundary conditions and are intended to identify the origin of a submerged vortex. Figure 3.9 compares instantaneous distributions of streamwise vorticity, ω_x, computed in Case A on a cross section at X=2,100 mm (=14.0D_b, Figure 3.9 -(a)), X=1,200 mm (=8.0D_b, Figure 3.9 -(b)), and X=300 mm (=2.0D_b, Figure 3.9 -(c)), and that computed in Case B on a cross section at X=300 mm (=2.0D_b, Figure 3.9 -(d)). Streamwise vortices with a diameter of approximately 2 mm (0.013D_b) and a separation of approximately 10 mm (0.067D_b) are confirmed to exist in the boundary layer computed in Case A downstream of the step, and its time-averaged velocity profile also confirms that the boundary layer computed in Case A becomes turbulent downstream of the step (not shown in this paper). As they approach the suction pipe, the size of the streamwise vortices becomes larger because the upward flow towards the suction pipe decreases the velocity shear near the bottom wall. To the contrary, no streamwise vortices are confirmed in the boundary layers computed in Case B, and its time-averaged velocity profiles also confirm that the boundary layer computed in Case B remains laminar (not shown in this paper). Although not shown in a figure, the velocity profiles computed in Case C have no velocity shear near the bottom and side walls of the rectangular channel.

Figure 3.10 shows typical suction vortices computed and visualized in each of Cases A, B, and C. In Cases A and B, for which the boundary layer develops on the bottom wall of the pump sump, a submerged vortex that has its one end of the vortex line on the bottom wall is formed. On the other hand, no submerged vortex is confirmed in Case C for which no velocity shear exists near the bottom wall of the pump sump. During the entire period of time investigated in this study, no submerged vortex is formed in Case C. From these observations, the origin of a submerged vortex has been identified to be the mean shear of the velocity profiles in the boundary layer that develops on the bottom wall of the pump sump, and it is concluded that the streamwise vortices in the turbulent boundary layer make no direct contribution to the formation of a submerged vortex. Please note, however, that the

submerged vortex computed in Case A is apparently stronger than that computed in Case B. This is presumably because the mean velocity shear near the bottom wall of the pump sump computed in Case A, where the boundary layer on the bottom wall is turbulent, is stronger than that computed in Case B, where the boundary layer on the bottom wall is laminar. With this regard, the mechanism for a submerged vortex to be formed from the mean shear in the boundary layer will be detailed in the next subsection. In this case study, the suction pipe is installed near the side wall of the pump sump, and in such a case, a submerged vortex that is formed from the mean shear in the boundary layer on the side wall is likely to be formed. Further research may be warranted to investigate formation of a submerged vortex with such an origin.

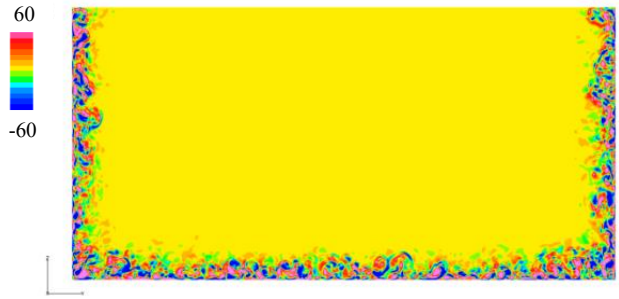

(a) Vorticity ω_x at X=2,100 mm in Case A

(b) Vorticity ω_x at X=1,200 mm in Case A

(c) Vorticity ω_x at X=300 mm in Case A

(d) Vorticity ω_x at X=300 mm in Case B

Figure 3.9. Instantaneous streamwise vorticities computed in Case A ((a)-(c)) and Case B (d).

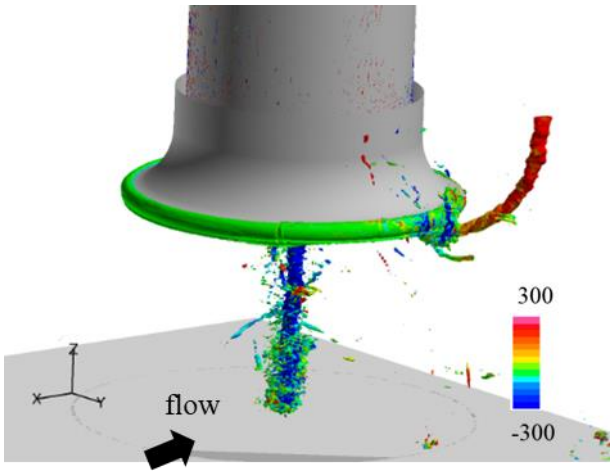

(a) Turbulent boundary layer (Case A)

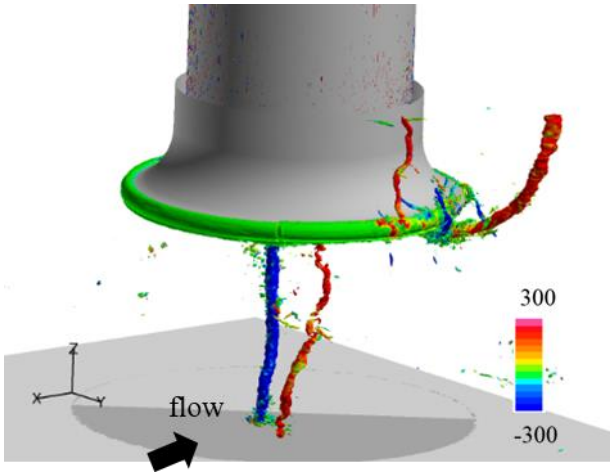

(b) Laminar boundary layer (Case B)

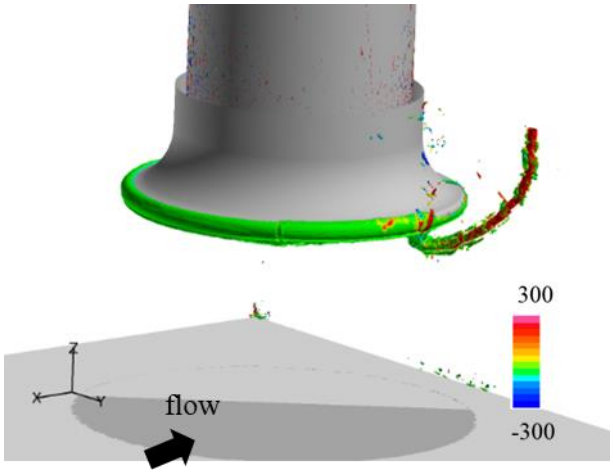

(c) No boundary layer (Case C)

Figure 3.10. Visualized suction vortices in Case A, Case B and Case C.

3.6 Formation Mechanism of a Sub-merged Vortex

The mechanism for a submerged vortex to be formed will be investigated in detail in this subsection. The approaching boundary layer that develops in an actual pump sump has a Reynolds number at least by one order higher than that studied in this paper, and is most likely turbulent. To investigate the formation mechanism of a submerged vortex, the large-eddy simulation in Case A is performed for a long time period and the computed flow fields are investigated in detail. Please note that turbulent boundary layers develop on the bottom and side walls of the pump sump in this case and virtually the same vortical structures are computed as those computed in Case D, which has twice finer grid resolution as shown in Figure 3.5. The computation is continued for 200,000 time steps (16 seconds) with a time increment of 0.08 msec., which corresponds to a dimensionless time of approximately 40 based on the inlet velocity given for the rectangular channel (0.37 m/s) and the opening diameter of the bellmouth (150 mm). A total of 4,000 instantaneous flow fields are output every 50 time steps with an interval of 4 msec. for subsequent investigations.

As already mentioned, the origin of a submerged vortex is the local shear in the boundary layers that develop in the pump sump, and turbulent eddies make no direct contributions to the formation of a submerged vortex. It is also confirmed in the large-eddy simulation performed for a long period of time that once they are formed, submerged vortices stably exist for a long time, and therefore, the unsteadiness of the flow is not presumably playing an essential role in the formation of a submerged vortex.

The boundary layer on the bottom wall of the pump sump has a mean velocity shear with a vorticity in the lateral direction, ω_Y. For a submerged vortex to be formed from this lateral vorticity, ω_Y, it is necessary for this to be converted to a vertical vorticity, ω_Z, and the vortex is stretched in its axial direction. We will therefore investigate this mechanism by using the transport equation of the vorticity vector, obtained by taking rotation of the Navier-Stokes equation as shown below, and applying them to the time averaged flow.

$$(\vec{u} \cdot \nabla)\vec{\omega} = (\vec{\omega} \cdot \nabla)\vec{u} + \nu\nabla^2\vec{\omega} \tag{5}$$

where $\vec{u}$, and $\vec{\omega}$ respectively denote the velocity and vorticity vectors in the time average flow.

The left-hand side of equation (5) represents the change of the vorticity vector along a streamline while the first and second terms in the right-hand side, respectively, represent the change of the axis of the vortex and dissipation of the vorticity vector due to the viscous diffusion. As already stated, in the time-averaged boundary layer profile on the bottom wall of the pump sump, only the lateral vorticity component, ω_{Y}, exists. For the vertical vorticity, ω_{Z}, to be produced, the axis of the vorticity vector should have been converted from the lateral direction to the vertical direction. The viscous diffusion term, namely, the second term in the right-hand side of equation (4), does not have such a function, and also the effects of viscous diffusion is negligibly small in a large-scale flow. Therefore, the vertical vorticity, ω_{Z}, should have been produced by the right-hand terms in the following equation (6).

$$u\frac{\partial \omega_Z}{\partial x} + v\frac{\partial \omega_Z}{\partial y} + w\frac{\partial \omega_Z}{\partial z} = \omega_{\mathrm{X}}\frac{\partial w}{\partial x} + \omega_{\mathrm{Y}}\frac{\partial w}{\partial y} + \omega_{\mathrm{Z}}\frac{\partial w}{\partial z} \tag{6}$$

where u, v and w are, respectively, the streamwise, lateral, and vertical velocity components, and ω_{Z} is the vertical vorticity component.

Figure 3.11 shows distributions of each of the vorticity components and the gradients of the vertical velocity on a horizontal plane 1 mm ($0.0067D_{\mathrm{b}}$) above the bottom wall of the pump sump, which compose the right-hand side of equation (6). The flow fields are averaged during a time period from t=0.0 sec to t=0.8 sec. where a submerged vortex rotating in the clockwise direction stably exists. The two circles in these figures are the projected lines of the inner and outer walls the suction pipe, and the main-flow direction is from the right to the left (negative X directions). The rounded rectangles in the bottom figure are drawn to clearly identify the sign of the gradients of the vertical velocity. The distributions of ω_{X} and ω_{Y} take the minimum and maximum values at a radius approximately one-third of the inner radius of the suction pipe from its center, which indicates that vorticity vector is aligned in the radial direction on this plane. On the other hand, the gradients of the vertical velocity shown at the bottom figures indicate that the vertical velocity is accelerated from all the peripheral directions toward the center of the suction pipe. From these observations, it is concluded that

the lateral vorticity ω_Y that originally exists in the approaching boundary layer on the bottom wall rotates around the axis of the suction pipe due to the asymmetry of the pump sump, and forms vorticity vector with its axis aligned to the radial direction around the projected center of the suction pipe. This vorticity vector is then turned to the vertical direction due to the radial gradients of the vertical velocity (denoted by the first and second terms in equation (6)), and forms vertical vorticity, ω_Z. The vertical vorticity ω_Z is finally increased due to the acceleration of the vertical velocity denoted by $\partial w/\partial z$. Namely, the vortex is stretched in the vertical direction. This is the mechanism for a submerged vortex to be formed from the lateral vorticity, which originally exists in the approaching boundary layer on the bottom wall of the pump sump.

Further detailed studies are made to clarify the mechanism for the velocity vector with its axis aligned to the radial direction to be formed around the projected center of the suction pipe near the bottom wall of the pump sump. As shown in the top left figure in Figure 3.11, the streamwise vorticity, ω_X, takes the positive maximum value upstream of the projected center of the suction pipe (right-hand side of the white circles in bottom figures). The change in the streamwise vorticity ω_X along a streamline is represented by the following equation (7).

$$u\frac{\partial \omega_X}{\partial x} + v\frac{\partial \omega_X}{\partial y} + w\frac{\partial \omega_X}{\partial z} = \omega_X\frac{\partial u}{\partial x} + \omega_Y\frac{\partial u}{\partial y} + \omega_Z\frac{\partial u}{\partial z} \tag{7}$$

Apart from the projected center of the suction pipe, only the second term exists in the right-hand side of this equation because both ω_X and ω_Z are initially zero. Figure 3.12 shows distributions of ω_Y and $\partial u/\partial y$, which compose the right-hand side of equation (7). The flow fields are averaged over the same period of time as for the previous figure (Figure 3.11), but, these distributions are presented in a wider region to understand the growth of each term.

The lateral gradient of the streamwise velocity is positive in the region enclosed by the rounded rectangle in the right figure. This means that more flow flows through the wider region (with negative Y coordinates) where the flow velocity becomes higher and less flow flows through the narrower region (with positive Y coordinates) where the flow velocity becomes lower. Please recall that the main-flow direction is the negative X direction. Mainly in this region, the streamwise vorticity ω_X is produced by the second term in equation (7). In

a similar manner, vorticity vector with its axis aligned in the radial direction is formed around the projected center of the suction pipe, due to the unevenness of the main flow.

To confirm the formation mechanism described above, the temporal evolution of the vorticity vector ω_Z with its axis aligned to the radial direction and that of acceleration of the vertical velocity are investigated in a time period when a submerged vortex is formed. Figure 3.13 shows the distributions of the vertical vorticity (top) and vertical acceleration of the vertical velocity (bottom) on a horizontal plane 1 mm ($0.0067D_b$) above the bottom wall of the pump sump as in the previous figures for subsequent three periods of time of 0.8 seconds. Iso-surfaces of the vertical vorticity is also superimposed in these figures. Please note that these iso-surfaces are identical in the top and bottom figures. During the time period of 4.8 sec to 5.6 sec (left), no submerged vortex is confirmed by the iso-surfaces of the vertical vorticity. A submerged vortex is formed in the time period of 5.6 sec to 6.4 sec (middle), and it grows in the time period of 6.4 sec to 7.2 sec (right). When the submerged vortex is formed and grows, ω_Z and $\partial w/\partial z$, also become large around the projected center of the suction pipe. In particular, it is interesting to note that ω_Z converted from ω_Y in a way explained above already exists near the bottom wall of the pump sump in the time period of 4.8 sec to 5.6 sec when a submerged vortex has not been formed. On the other hand, the region with vertical acceleration first appears near the inlet of the suction pipe, grows in the downward direction, and finally reaches the bottom wall, when the vortex with vertical vorticity ω_Z is stretched and a strong submerged vortex is formed.

From the temporal evolution of iso-surface of vertical vorticity shown in Figure 3.13, the formation of submerged vortex seems to be started from higher location and proceeded to the bottom wall. Figure 3.14 shows the temporal evolution of time-averaged vertical vorticity ω_Z on horizontal planes with a height of 1mm, 40mm and 80mm. At the beginning of the formation of the submerged vortex (T= 4.0 ~ 4.8 sec), strong vorticity (please see region colored by blue, which corresponds to negative vertical vorticity ω_Z) is appeared on only higher horizontal planes with 40mm and 80mm. Figure 3.15 shows the temporal evolution of time-averaged $\partial w/\partial z$ on those horizontal planes. The reason for larger vertical vorticity at higher location at the beginning of vortex formation is larger $\partial w/\partial z$ (vertical acceleration) there shown in Figure 3.15. The strong acceleration near the bottom wall at the time period T=5.6 ~ 6.4 and 6.4 ~ 7.2 shown in Figure 3.15 indicates that strong acceleration near the

bottom wall is essential for formation of submerged vortex. This analysis indicates that concentration of vertical vorticity near the bottom wall and stretch of vortex due to vertical acceleration are occurred at the same time, and finally a submerged vortex is generated by strong vertical acceleration near the bottom wall.

The formation mechanism of a submerged vortex identified in the present study supports, with a clear and logical basis, countermeasures for formation of a submerged vortex in a pump sump, such as reduction in the vertical velocity near the bottom wall, mitigation of the mean velocity shear in the approaching boundary layers, and prevention of the asymmetry that may trigger conversion of the axis of the vorticity. Although some of them may have been put into practice empirically, the authors believe that they can be used more effectively with these findings presented in this paper.

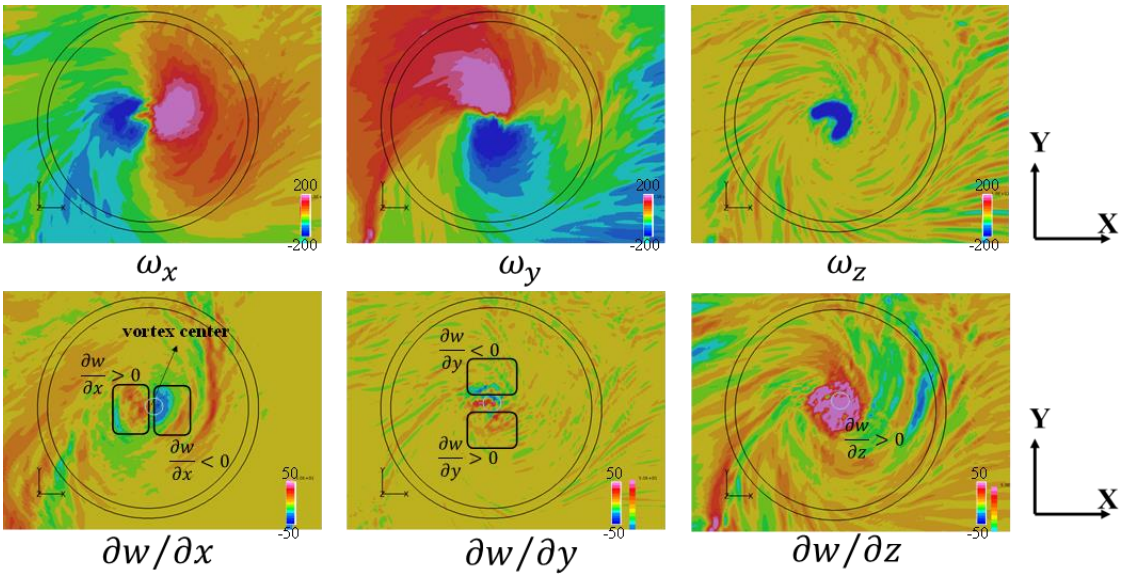

Figure 3.11. Distributions of vorticity (ω_i) and gradient of axial velocity ($\partial w/\partial x_i$) on horizontal plane with a height of 1mm ($0.0067D_b$), averaged during 0 sec and 0.8 sec when a clock-wise submerged vortex continues to exist.

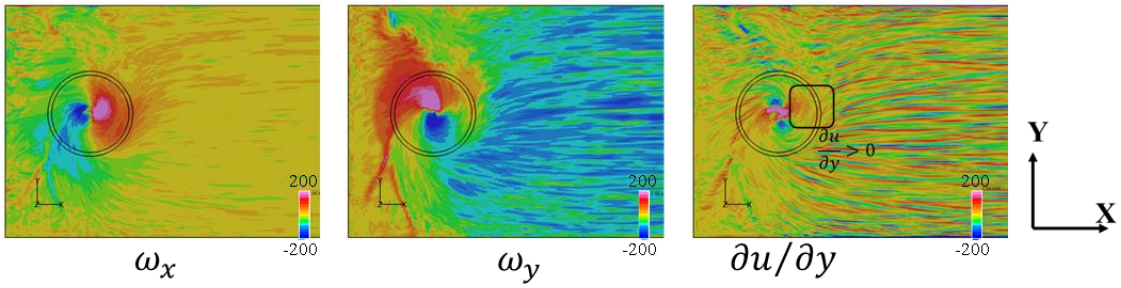

Figure 3.12. Distributions of vorticity components ω_x, ω_y and gradient of mainstream velocity ($\partial u/\partial y$) on horizontal plane with a height of 1mm ($0.0067D_b$), averaged during 0 sec and 0.8 sec when a clock-wise submerged vortex continues to exist.

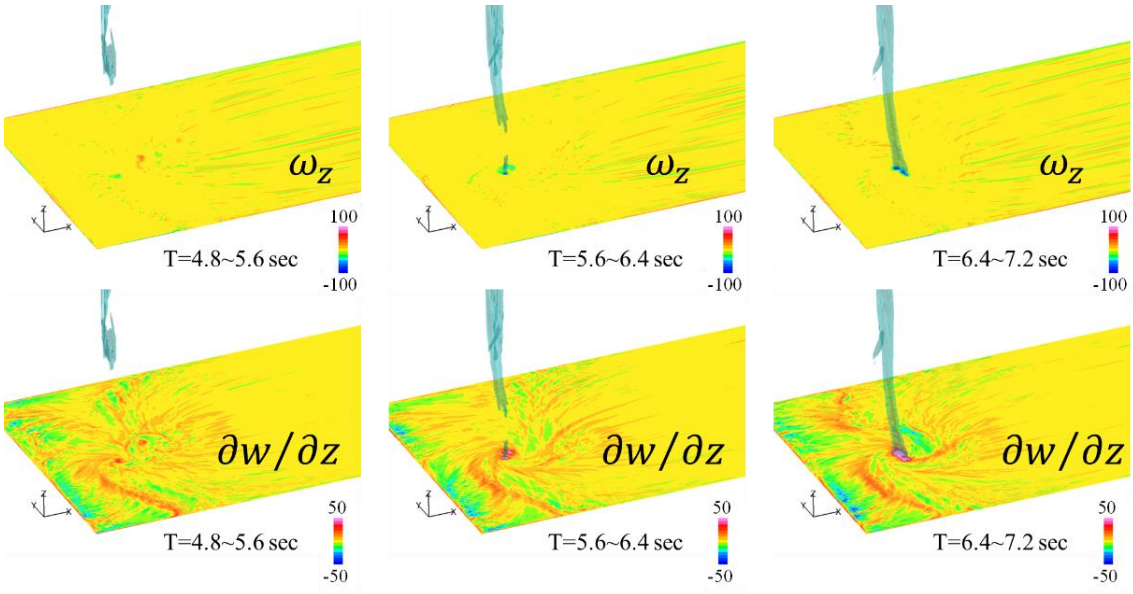

Figure 3.13. Temporal evolution of time-averaged ω_z (top) and $\partial w/\partial z$ (bottom) on horizontal plane with a height of 1mm ($0.0067D_b$), together with iso-surface of vertical vorticity ω_z during t = 4.8 sec and t = 7.2 sec.

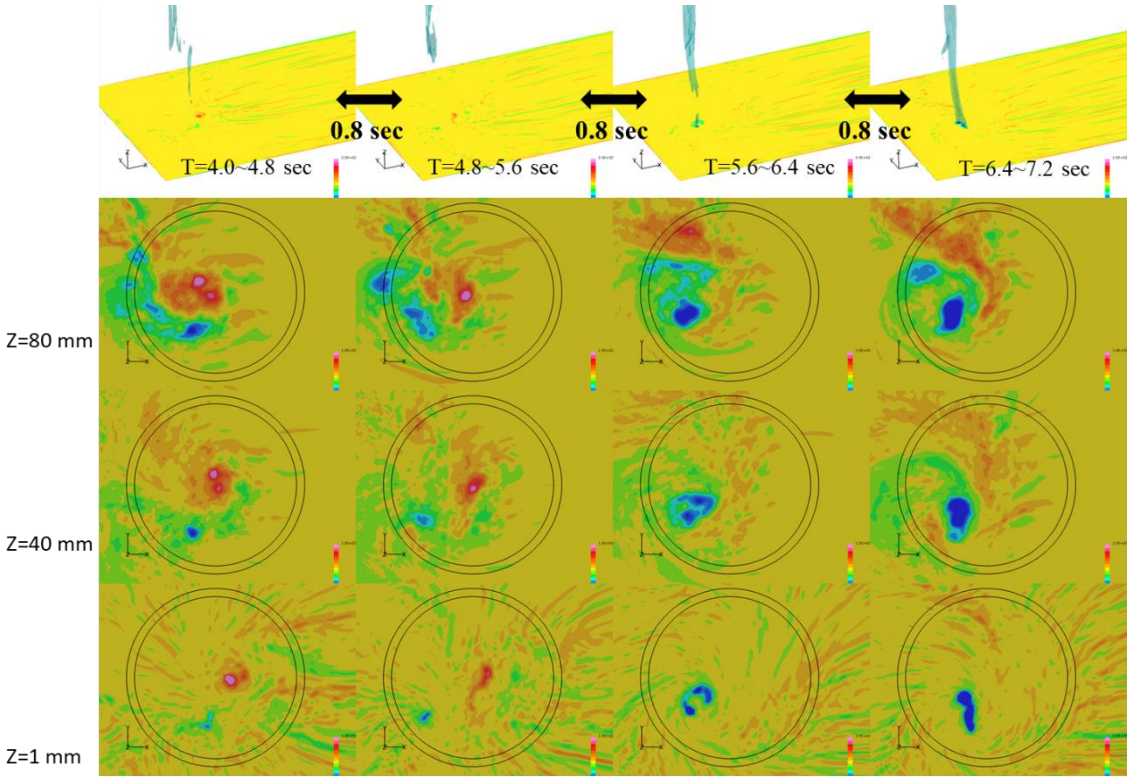

Figure 3.14. Temporal evolution of time-averaged ω_z on horizontal planes with a height of 1mm, 40mm and 80mm together with iso-surface of vertical vorticity ω_z during t = 4.0 sec and t = 7.2 sec.

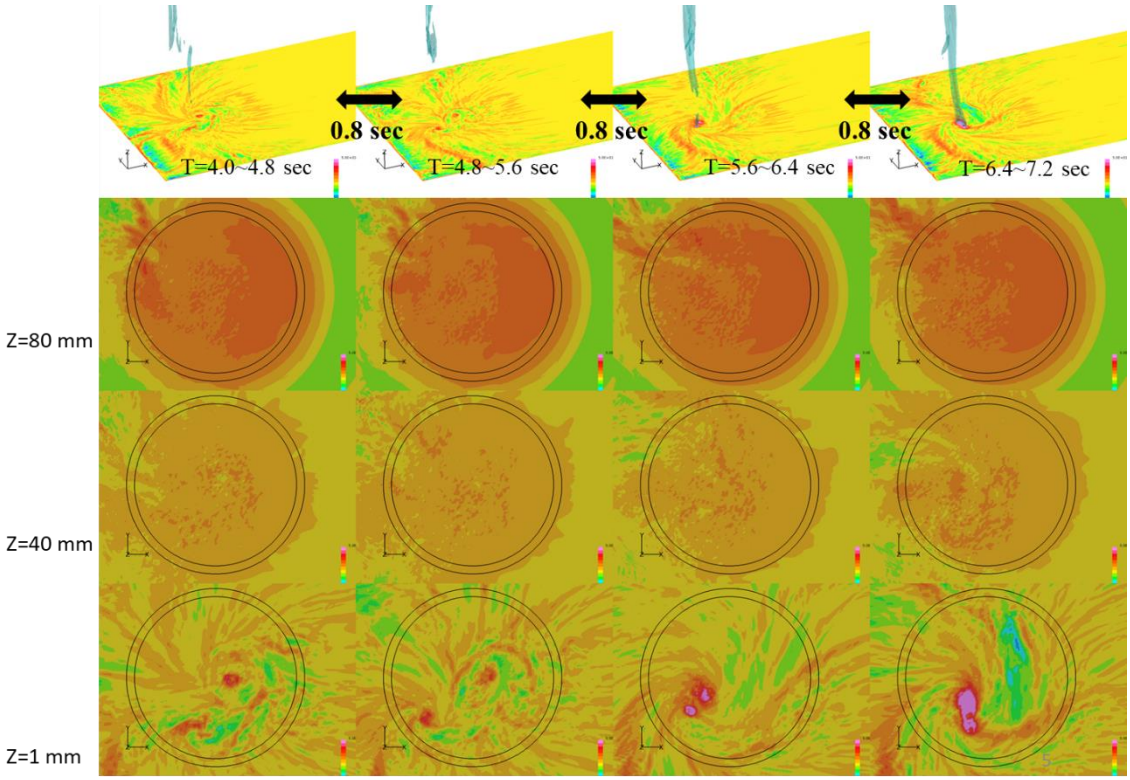

Figure 3.15. Temporal evolution of time-averaged $\partial w/\partial z$ on horizontal planes with a height of 1mm, 40mm and 80mm together with iso-surface of vertical vorticity ω_z during t = 4.0 sec and t = 7.2 sec.

3.7 Dissipation Mechanism of a Sub-merged Vortex

Case studies are also made using the flow fields obtained by the large-eddy simulation done in the long period of time to identify the mechanism for a submerged vortex once formed to be dissipated.

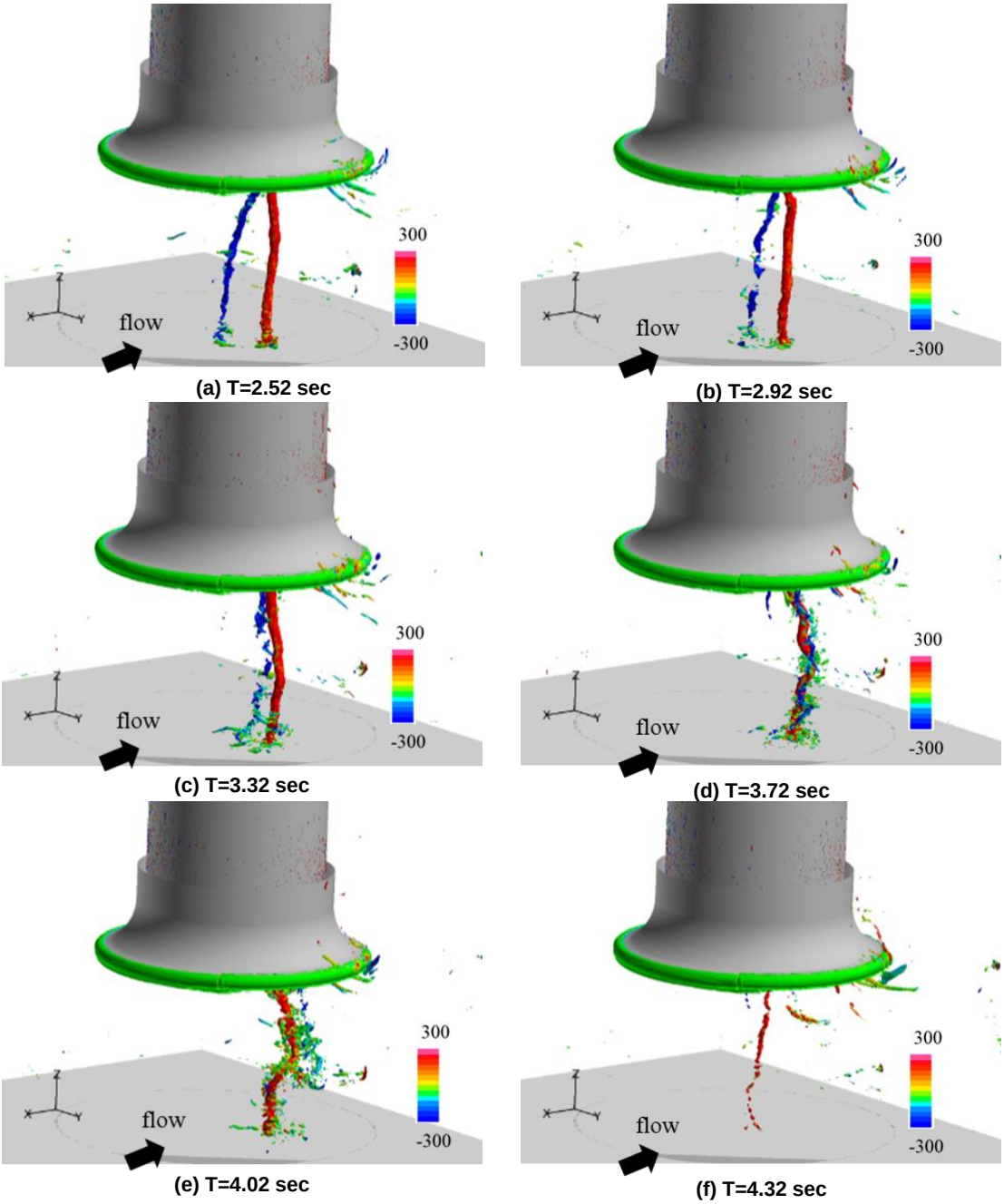

Figure 3.16 shows one such example when two counter-rotating submerged vortices approach

each other and finally, one of the two vortices is dissipated. In the time period of T=2.52 sec. to 3.32 sec., two counter-rotating vortices exist and approach each other. In the time period of T=3.72 sec. to 4.02 sec. they merge, and at the time of T=4.32 sec. after the merge, only the submerged vortex rotating in the counterclockwise direction shown in red exists and that rotating in the clockwise direction shown in blue is dissipated. The submerged vortex rotating in the counterclockwise direction is also weakened after the merge. In other cases, the submerged vortex rotating in the clockwise direction exists after the merge, or, both submerged vortices are dissipated after the merge. The merge of two counter-rotating submerged vortices is confirmed to be one of the causes of the dissipation of a submerged vortex. But, further investigation is needed to thoroughly understand the dissipation mechanism of a submerged vortex in a pump sump.

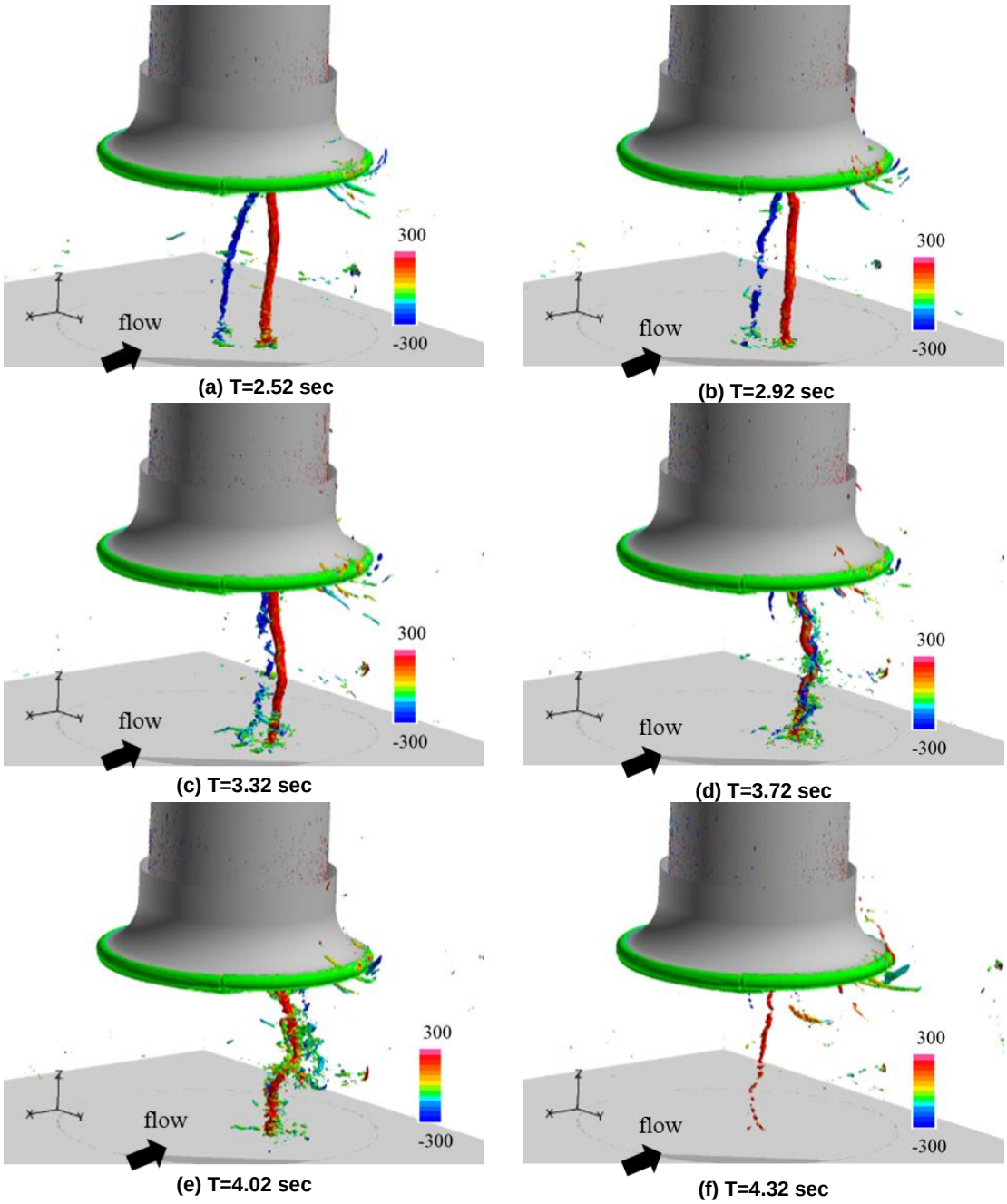

Figure 3.16. Visualized disappearance of two submerged vortices with clockwise (blue) and counter-clockwise (red) sense of rotation.

3.8 Correlation of Vertical Vorticity and Occurrence of a Submerged Vortex

To further investigate the formation and dissipation of a submerged vortex in a pump sump, the temporal variation of the maximum and minimum vertical vorticity on a horizontal plane at a high of 6 mm ($0.04D_b$), 30 mm ($0.20D_b$), and 60 mm ($0.40D_b$) are shown in Figure 13. The vertical vorticity has been normalized by the inflow velocity of the pump sump (0.37 m/s) and the width of the pump sump (0.3 m), as already mentioned. The blue and red lines, respectively, represent the minimum and maximum values, which correspond to the submerged vortex (if it exists) rotating in the clockwise and counterclockwise directions. The vertical vorticity with a clockwise sense of rotation shown in blue is generally stronger than that with a counterclockwise sense of rotation shown in red. This is because the suction pipe is installed with an offset of 10 mm ($0.067D_b$) in the positive Y direction, and therefore, more flow turns from the wider region (with negative Y coordinates) in the clockwise direction and flows toward the suction pipe, and less flow turns from the narrower region (with positive Y coordinates) in the counterclockwise direction and flows toward the suction pipe. Figure 3.18 shows the vortical structures visualized at T=3.20 sec. (left) and T=7.52 sec. (right), respectively when the vertical vorticity with the counterclockwise sense of rotation takes its maximum value and when that with the clockwise sense of rotation takes its minimum value. At both instances, a submerged vortex with a counterclockwise sense of rotation (left) and that with a clockwise sense of rotation (right) exist. It is confirmed, from the detailed investigations of the flow fields and the temporal variations in the vertical vorticity at other instances, that when the absolute value of the vertical vorticity near the bottom wall is high, a strong submerged vortex exists in the pump sump.

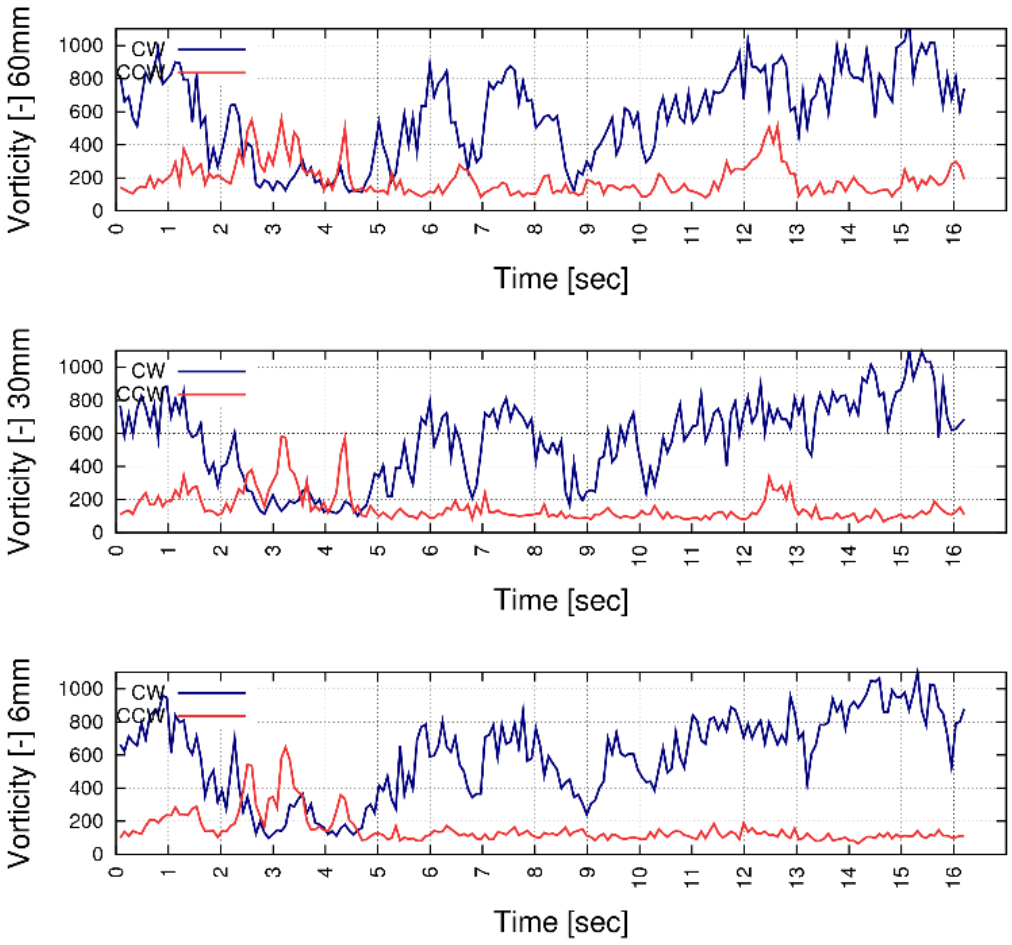

Figure 3.17. Temporal evolution of computed maximum vertical vorticity with clockwise (blue) and counterclockwise (red) rotation horizontal planes at Z=6 mm (=0.04D_b, bottom), 30 mm (=0.20D_b, middle) and 60 mm (=0.4D_b, top).

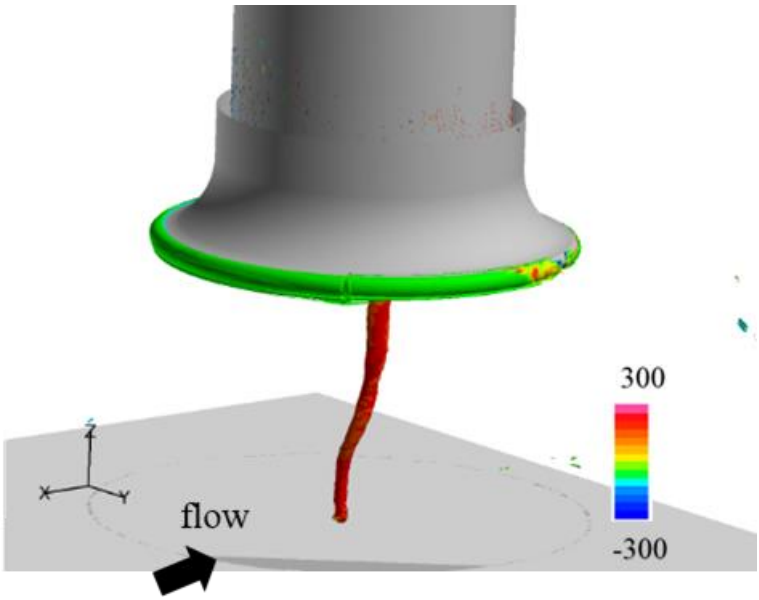

(a) T=3.30 sec

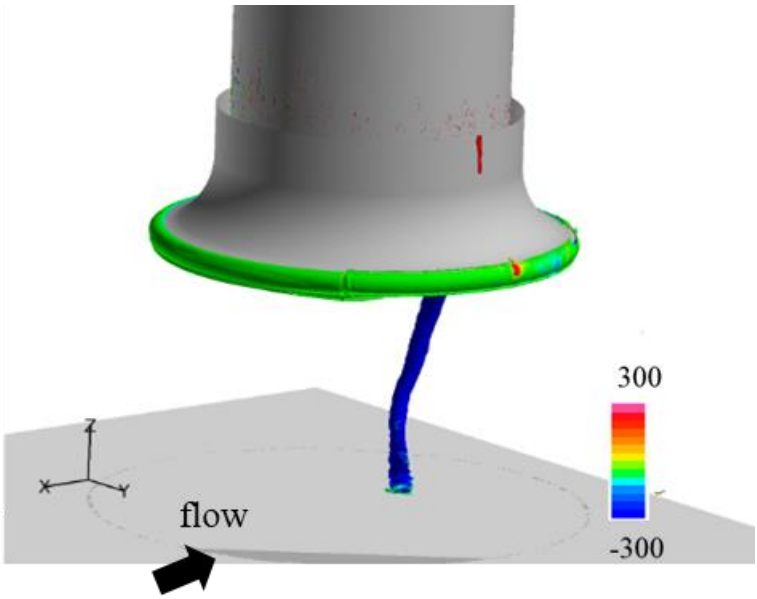

(b) T=7.52 sec

Figure 3.18. Submerged vortices visualized when vertical vorticities takes a maximum value on z=6 mm ($0.047D_b$) plane.

3.9 Origin and Formation Mechanism of an Air-entrained Vortex

Finally, the origin and formation mechanism of an air-entrained vortex will be described in this subsection. The instantaneous flow fields computed by the long-term large-eddy simulation (denoted as Case A) described in the previous subsections are also investigated to identify the origin and formation mechanism of an air-entrained vortex. For this case, the water depth h is set to 150 mm ($1.00D_{\mathrm{b}}$), the height under the bellmouth inlet, h_1, is set to 100 mm ($0.67D_{\mathrm{b}}$), and therefore the submergence of the bellmouth inlet (the distance between the bellmouth inlet and the water surface), h_2, is 50 mm ($0.33D_{\mathrm{b}}$), as shown in Figure 2 and Table 2.

Figure 15-(a) and (b) show air-entrained vortices visualized at two different instances, for each of which 200 flow fields are averaged over 0.8 seconds. The top figures show the vortical structures while the bottom figures show the distributions of the vertical vorticity on the top boundary of the computational domain, which corresponds to the water surface (hereafter, simply referred to as "water surface"). Please recall that as already described, the slip wall boundary condition is given on this surface and the effects of free water surface is not taken into account in this study. Red color indicates a positive vertical vorticity, namely, a vortex rotating in the counterclockwise direction while blue color indicates a negative vertical vorticity, namely, a vortex rotating in the clockwise direction. At the time T=1.52 sec. when the instantaneous distribution of the vertical vorticity on the water surface is shown in the bottom of Figure 3.19-(a), the maximum vertical vorticity with a counterclockwise sense of rotation is high in the region with positive Y coordinates on the water surface, and an air-entrained vortex is formed from the point where the vertical vorticity is the maximum on the water surface. At the same instance, the absolute value of the minimum vertical vorticity with a clockwise sense of rotation is also high in the region with negative Y coordinates, and another air-entrained vortex is formed behind the suction pipe. This air-entrained vortex is not visible in Figure 3.19-(a) because the suction pipe blocks its view. On the other hand, at T=2.32 sec. when the instantaneous distribution of the vertical vorticity on the water surface

is shown in the bottom of Figure 3.19-(b), the absolute value of the minimum vertical vorticities or the maximum vertical vorticities is high only in the region with negative Y coordinates and it is low in the region with positive Y coordinates. At this instance, an air-entrained vortex is formed only in the region with negative Y coordinates as is confirmed in the right of Figure 3.19-(c). This air-entrained vortex is not visible in Figure 3.19-(b) because the suction pipe blocks its view.

Figure 16 shows the temporal variations of absolute values of the maximum and minimum vertical vorticity (hereafter, simply referred to as “maximum vertical vorticity”) in the black rectangles shown in Figure 3.19-(a) and (b), for which the vertical vorticity is normalized by the inflow velocity (0.37 m/s) and the width of the pump sump (0.3 m), as already mentioned. Figure 3.20, at the upper figure, shows the variation of the maximum vertical vorticity in the narrower side (region with positive Y coordinates) while at the lower it shows that in the wider side (region with negative Y coordinates). The blue line denoted by “CW” shows negative vertical vorticity, namely, a vortex rotating in the clockwise direction while the red line denoted by “CCW” shows positive vertical vorticity, namely, a vortex rotating in the counterclockwise direction.

In the region with positive Y coordinates on the water surface, a trace of an air-entrained vortex rotating in the counterclockwise direction is identified in some instances, but, that of a vortex rotating in the clockwise direction is hardly confirmed. To the contrary, in the region with negative Y coordinates on the water surface, a trace of an air-entrained vortex rotating in the clockwise direction is identified in some instances, but, that of a vortex rotating in the counterclockwise direction is hardly confirmed.

Detailed investigations are made on the relation between the instantaneous distribution in the vertical vorticity on the water surface and occurrence of an air-entrained vortex for the entire period of time. It has been clarified that an air-entrained vortex is formed when the maximum vertical vorticity is high on the water surface, which appears to be the trace of its one end of the vortex line on the water surface. From these detailed investigations, the origin of an air-entrained vortex is the strong vertical vorticity that appears in the separated flow downstream of the suction pipe. When this is sucked by the flow towards the inlet of the suction pipe, and stretched in the direction of the vortical axis, an air-entrained vortex is formed.

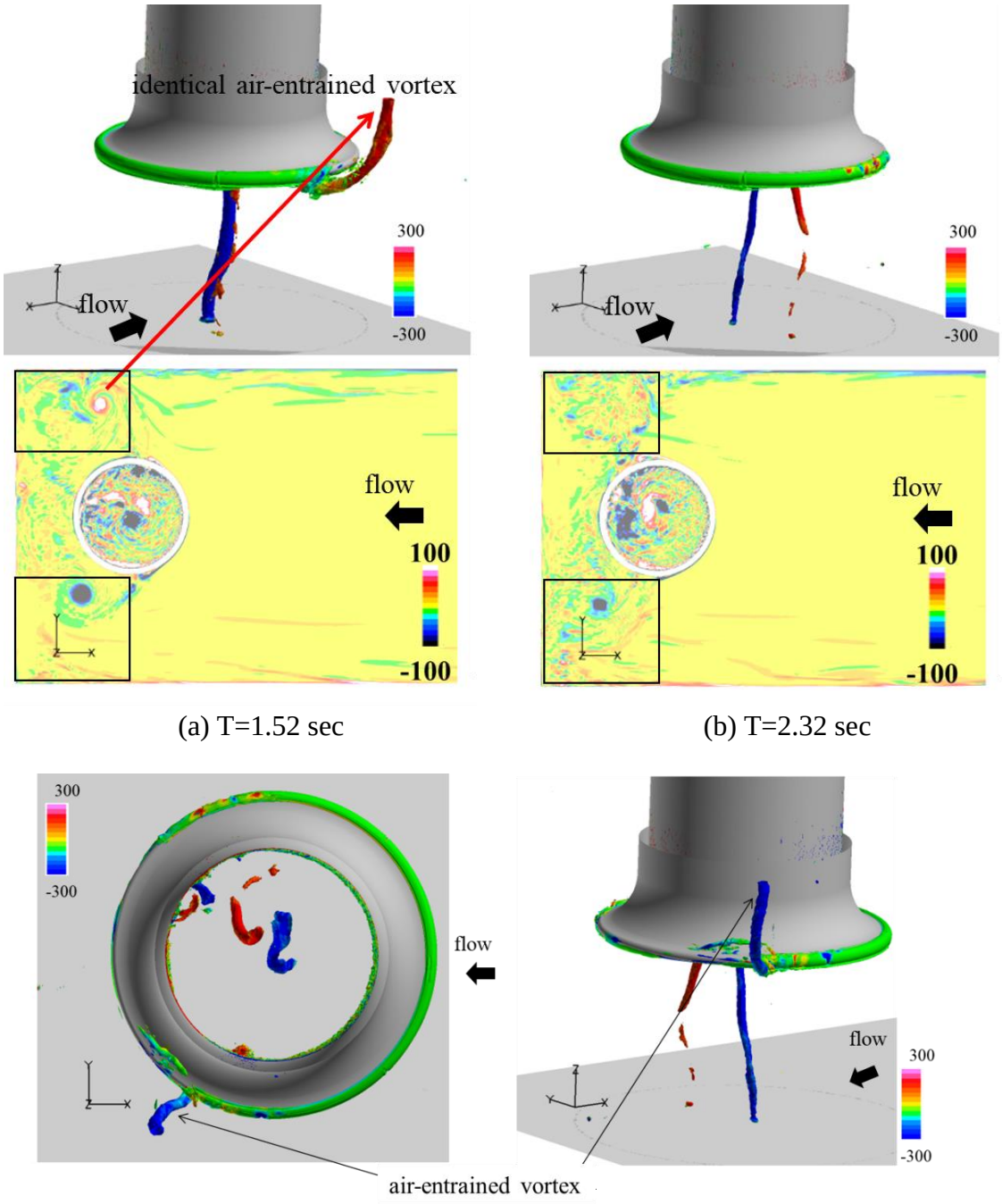

(a) T=1.52 sec

(b) T=2.32 sec

(c) T=2.32 sec (viewed from negative Y direction)

Figure 3.19. Air-entrained vortices and vertical vorticity on water surface visualized at two different instances.

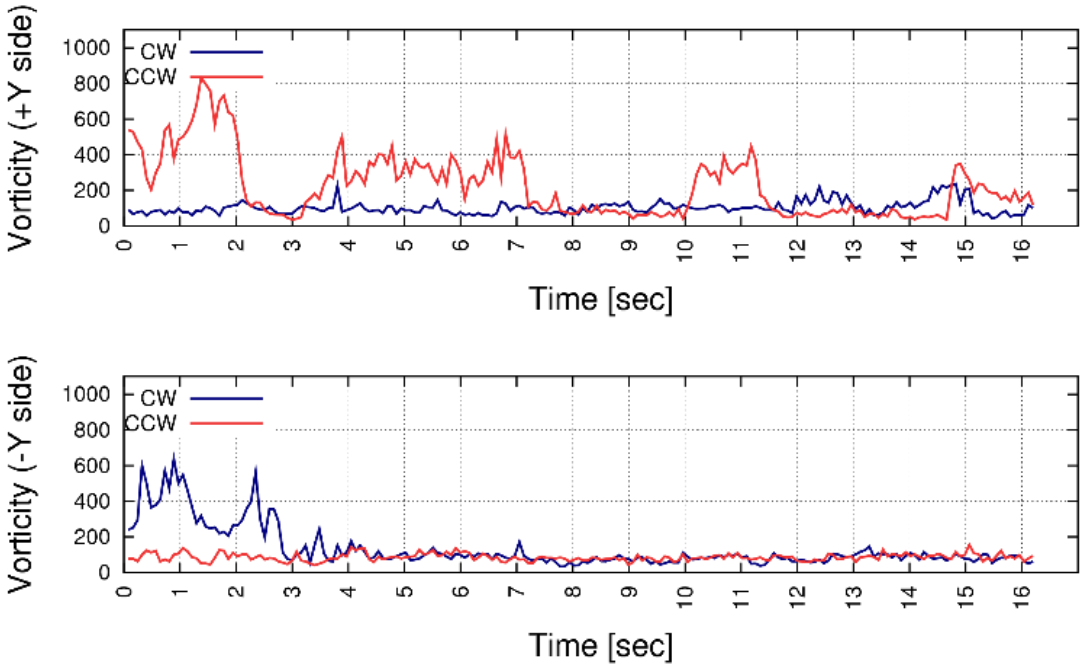

Figure 3.20. Temporal variation of maximum vertical vorticity on water surface enclosed by rectangles shown in Figure 3.16.

3.10 Effects of Height and Submergence of Bellmouth Inlet

To validate the formation mechanisms of a submerged vortex and an air-entrained vortex, large-eddy simulations with a different height and a different submergence of the bellmouth inlet are also performed in Case E and Case F as found in Table 3. In Case E, the height under bellmouth inlet, namely, the distance between the bottom wall and the inlet of the bellmouth inlet, h_1, is changed from 100 mm ($0.67D_\mathrm{b}$) to 150 mm ($1.00D_\mathrm{b}$) while in Case F, the submergence of bellmouth inlet, namely, the distance between the bellmouth inlet and the water surface , h_2, is changed from 50 mm ($0.33D_\mathrm{b}$) to 100 mm ($0.67D_\mathrm{b}$). In both cases, the water depth h is the same and it is 200 mm ($1.33D_\mathrm{b}$). Case E is intended to weaken the vertical acceleration near the projected center of the suction pipe on the bottom wall where the vertical vorticity is formed from the lateral vorticity in the boundary layer. Case F is intended to weaken the acceleration of the flow toward the inlet of the bellmouth from the water surface where the separated flow forms the origin of an air-entrained vortex.

Figure 3.21 represents typical vortical structures visualized in Case E (left) and Case F (right). As is expected, no submerged vortex exists in Case E while no air-entrained vortex exists in Case F. The vortex pointed by the arrow in Figure 3.21-(b) is not an air-entrained vortex, but, a submerged vortex with its one end on the side wall of the pump sump. These computations are continued for a time period of 0.65 seconds. But, no submerged vortex with its one end on the bottom wall of the pump sump is formed in Case E, and no air-entrained vortex is formed in Case F. Note however that the computed time of 0.65 seconds for Case E and Case F is shorter than that in Case A, for which the computation is continued for 16 seconds, and therefore, the conclusions presented in this subsection may include some uncertainty on the occurrence of a submerged vortex and that of an air-entrained vortex in Case E as well as in Case F.

Figure 3.22 compares the distribution in the vertical vorticity, ω_Z, and that in the vertical gradient of the vertical velocity, $\partial w/\partial z$, on a plane 1 mm ($0.067D_\mathrm{b}$) above the bottom wall. Iso-surfaces of the vertical vorticity is also superimposed in these figures. The results in Case

A are re-presentation of the right most of Figure 3.13. Flow fields are averaged over a time period from T=0.34 sec. to 0.64 sec. for Case E. Vorticity vector with its axis aligned to the radial direction and the vertical gradient of the vertical velocity are formed around the projected center of the suction pipe near the bottom wall in Case A while such flow structures are not confirmed in Case E, for which the distance between the bottom wall and the inlet of the suction pipe is increased by a half compared with Case A. This weakens the acceleration of the vertical velocity near the bottom wall of the pump sump. As clarified in the previous subsections, three major elements are needed for a submerged vortex to be formed in a pump sump: the mean shear in the approaching boundary layers, the change in the axis of the vorticity vector from the lateral to vertical directions, and finally, the acceleration of the flow in the vertical direction (stretch of the vortex with a vertical vorticity vector). In Case E, the final element is not met, and no submerged vortex is formed in this case.

Figure 3.23 compares, between Case A and Case F, the vortical structures in the pump sump and the distribution of the vertical vorticity on several horizontal planes at a height between the inlet of the bellmouth and the water surface. Both a submerged vortex and air-entrained vortex exist in Case A while only a submerged vortex exists and no air-entrained vortex exists in Case F. In both Case A and Case F, the main flow separates behind the suction pipe, and a region with a strong vertical vorticity appears in the separated flow in Case A (Figure 3.23-(a)) while such a region is not identified in Case F. The strong vertical vorticity that appears on the water surface is one end of an air-entrained vortex formed in the pump sump. Although further investigation with a longer computed time is needed to take the effects of water surface into account for the formation of an air-entrained vortex, the origin and formation mechanism of an air-entrained vortex identified in the present study seems still valid in an actual pump sump subjected to these effects of the water surface. In Case F, the flow toward the inlet of the suction pipe is weakened due to the longer distance between the inlet of the suction pipe and water surface, and as a result, no air-entrained vortex is formed in this case.

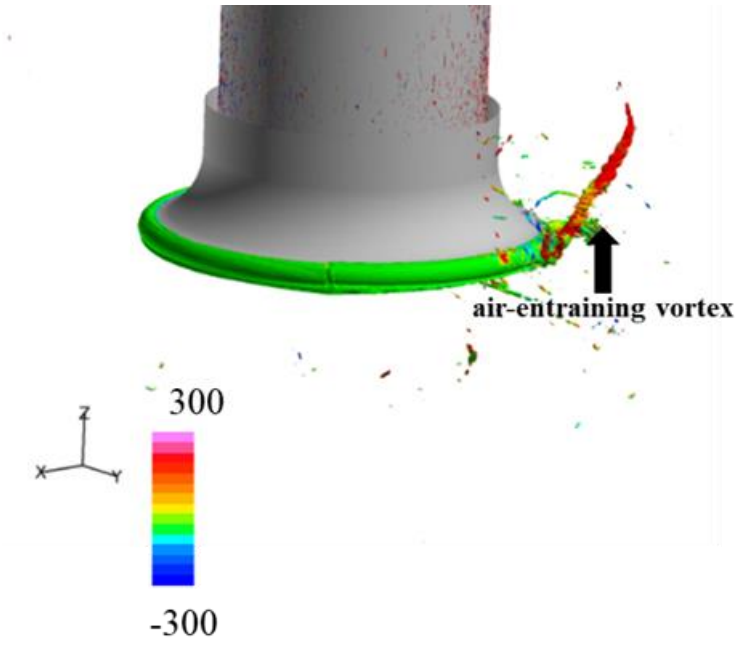

(a) Case E

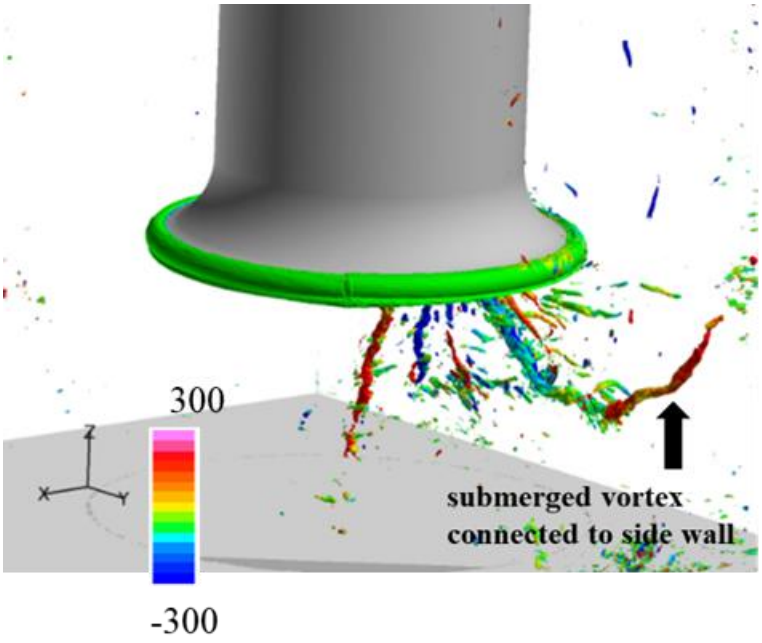

(b) Case F

Figure 3.21. Submerged and air-entrained vortices visualized in Case E and Case F.

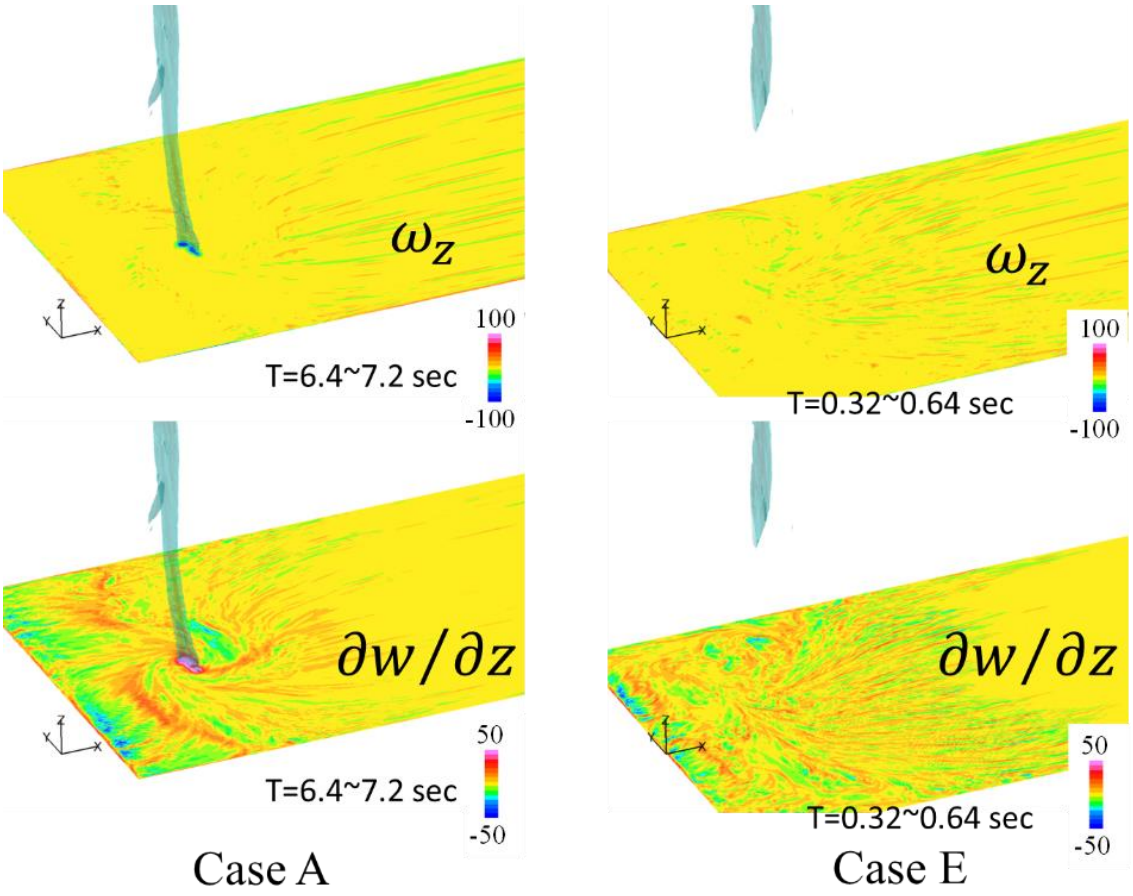

Figure 3.22. Time-averaged ω_z and $\partial w/\partial z$ on horizontal plane with a height of 1mm ($0.0067D_b$) together with iso-surface of vertical vorticity ω_z for Case A and Case E.

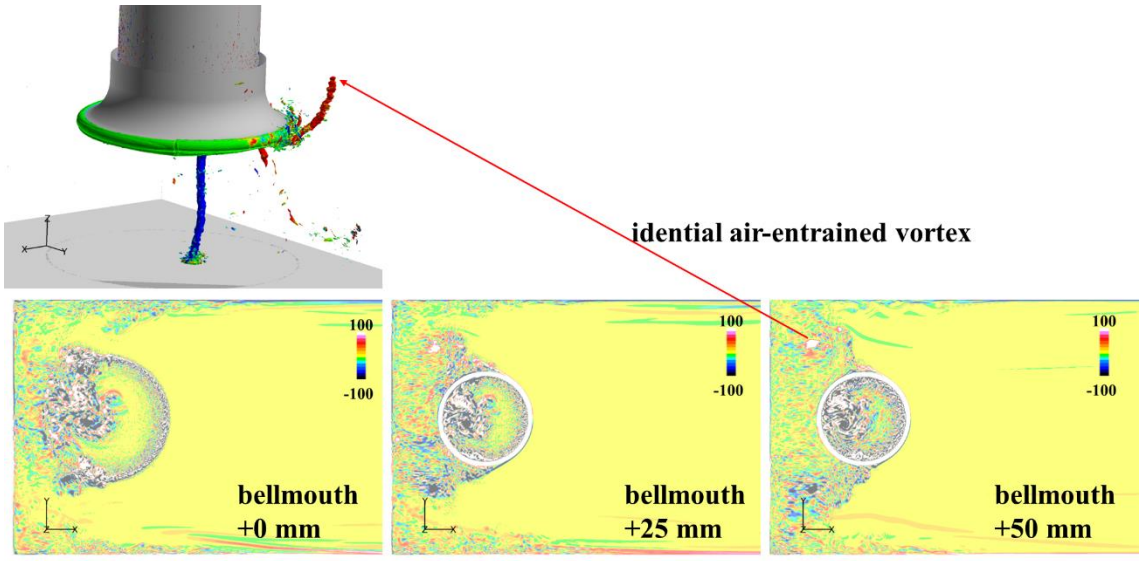

(a) Case A

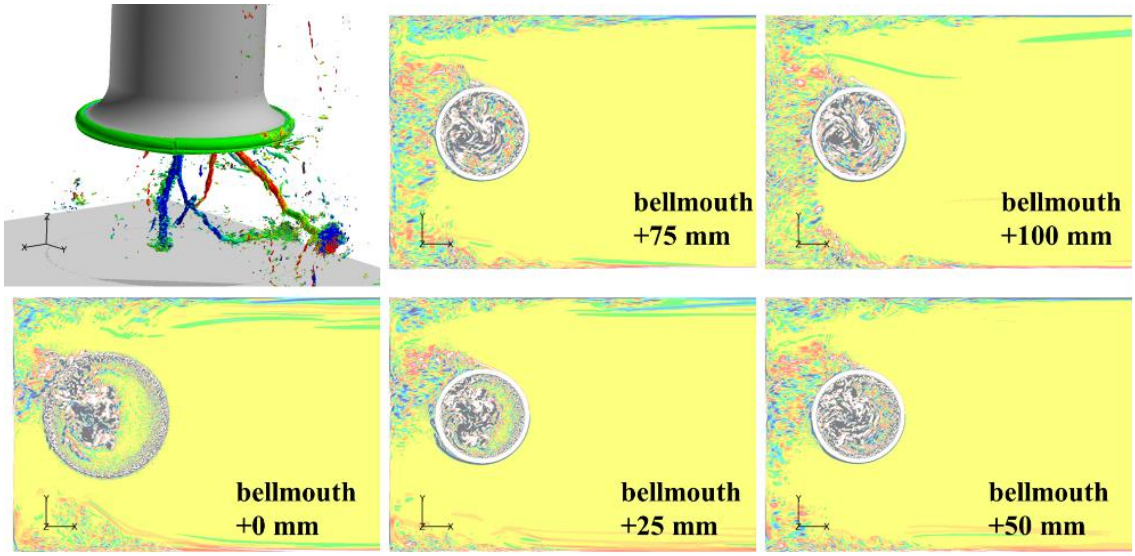

(b) Case F

Figure 3.23. Air-entrained vortices and vertical vorticity on horizontal cross sections for Case A and Case F.

Chapter 4. Dynamics of a submerged vortex

In the previous chapter, the origin and formation mechanism of a submerged vortex as well as those of an air-entrained vortex have been identified. In this chapter, the dynamics of a submerged vortex will be investigated in detail by large-eddy simulations applied to a simplified computational model, which is intended to represent the stretch of a submerged vortex under the suction pipe in the pump-sump model. A particular attention will be placed on the growth of the viscous core of the vortex, which results in the drop of the static pressure and on the effects of unsteady motion of the vortex on the growth of the viscous core.

4.1 Static-pressure Drop in Vortex Core in Model Pump Sump

To discuss its dynamics, the growth of the radial distributions of the velocity components and static pressure of a submerged vortex computed by the large-eddy simulation applied to the pump-sump model is investigated in detail. Figure 4.1 shows the radial distributions of the tangential and vertical velocities and the static pressure of a submerged vortex computed at heights of 6 mm ($0.04D_\mathrm{b}$), 30 mm ($0.20D_\mathrm{b}$) and 90 mm ($0.60D_\mathrm{b}$) from the bottom wall. These profiles are averaged over a sufficiently long period of time as well as for the circumferential direction around the center of the submerged vortex identified as the point where the static pressure is minimum. The submerged vortex that appears under the suction pipe is accelerated in the vertical direction. Namely, the vertical velocity of the vortex almost linearly increases with the increasing height from the bottom wall where it is zero. The distribution of the tangential velocity C_u is close to the one of the Rankine vortex composed of a combination of the forced vortex and the free vortex. The static pressure is the difference from a reference point at R = 54 mm ($0.36D_\mathrm{b}$), where it is not affected by the vortex. The static pressure becomes minimum at the center of the submerged vortex. The decrease in the

static pressure (hereafter, referred to simply as “pressure drop”) from the reference point is only 5 kPa, which corresponds to 5% of the atmospheric pressure. Occurrence of a submerged vortex is normally identified by the cavitation in model pump-sump experiments. In such a case, the pressure at the center of the vortex should have decreased to the saturated vapor pressure of water at the ambient temperature, and the pressure drop should be as big as approximately the atmospheric pressure. Therefore, the pressure drop of 5% of the atmospheric pressure is too small. One of the possible reasons of the underprediction of the pressure drop is the insufficient grid resolution. The radius where the tangential velocity reaches its maximum is about 3 ~ 4 mm ($0.020D_b$~ $0.027D_b$) in the computations. Hereafter, the region within this radius will be referred to as “vortex core”. The grid resolution (0.225 mm=$0.0015D_b$) of the large-eddy simulations applied to the whole pump-sump model is sufficiently fine to resolve the streamwise vortices in the turbulent boundary layers on the bottom and side walls of the pump-sump model. However, it is presumably insufficient to represent the sharp gradients of the tangential as well as axial velocities near the vortex core, which has motivated us to further investigate the dynamics of the submerged vortex by applying large-eddy simulations with even finer grid resolution as will be described below.

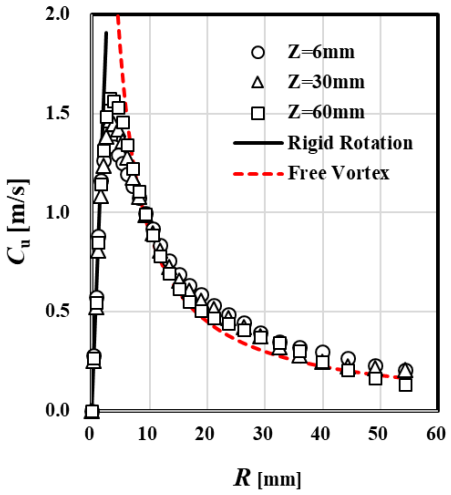

(a) Tangential velocity C_u

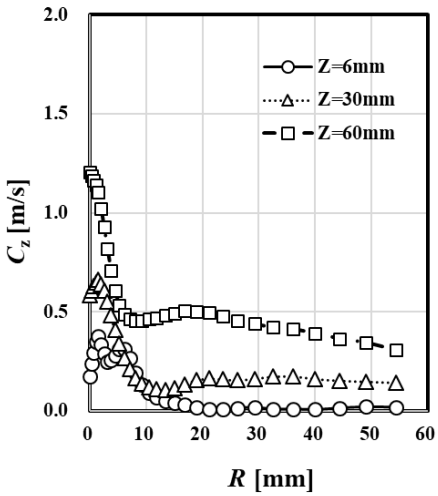

(b) Vertical velocity C_z

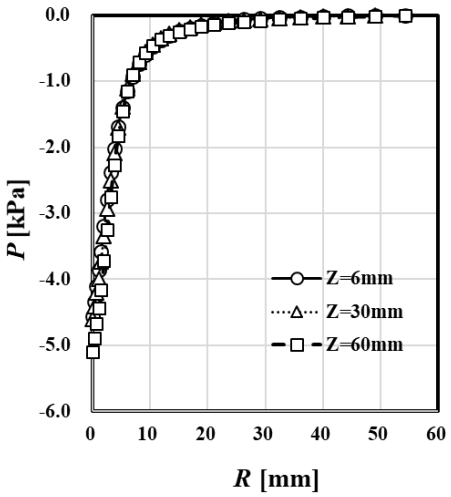

(c) Static pressure

Figure 4.1. Radial distributions of velocity components and static pressure of a submerged vortex computed in pump-sump model.

4.2 Computational Model

Large-eddy simulations of a submerged vortex with a grid resolution of 0.015 mm ($1.0 \times 10^{-4} D_b$), which is about fifteen times finer than those applied to the whole pump-sump model, are performed. If this grid resolution had been applied to the whole pump-sump model, the number of the computational grids would have exceeded 500 billion, which is not feasible, at least at this moment. Therefore, a simplified computational model, which is intended to represent the stretch of a submerged vortex under the suction pipe of the pump-sump model, is instead used in the present study. The simplified computational model is a paraboloid of revolution. With this shape, a constant gradient of the vertical velocity averaged over the cross section in the vertical direction is achieved, which represents the stretch of a submerged vortex formed near the bottom wall of the pump-sump model. The radius R of the paraboloid can be represented by the following function of the height Z.

$$R(Z) = R_1\sqrt{Z_1}/\sqrt{Z} \tag{8}$$

where R_1 and Z_1 are, respectively, the radius and the height of a reference horizontal plane set in the simplified computational model. As shown in Figure 4.2, this reference plane is set as the inlet boundary where the radius and the height are, respectively, R_1 = 30 mm ($0.20D_b$) and Z_1 = 30 mm ($0.20D_b$). This means that the inlet boundary of the simplified computational model has a radius of 30 mm ($0.20D_b$) and is placed at 30 mm ($0.20D_b$) above the bottom wall of the pump-sump model. The main region of the simplified computational model is from $Z = Z_1$ = 30 mm ($0.20D_b$) to Z = 100 mm ($0.33D_b$) where Z = 100 mm ($0.33D_b$) corresponds to the height $h_1$of the inlet of the suction pipe. The cross-sectional area at a height Z is inversely proportional to the height Z. Therefore, the averaged vertical velocity C_z is proportional to the height Z by the conservation of mass (i. e. by the continuity equation).

At the inlet boundary of the simplified computational model, the vertical velocity is set uniform, the radial velocity to zero, and the tangential velocity to that of a Rankine vortex as described by the following equation (9),

$$C_{z,inlet} = C_{z0}$$

$$C_{\mathrm{u,inlet}} = \begin{cases} C_{u0}\frac{r}{R_0} & (r < R_0) \\ C_{u0}\frac{R_0}{r} & (r \geq R_0) \end{cases} \tag{9}$$

$$C_{r,inlet} = 0$$

where C_{z0} is the axial velocity given at the inlet boundary, and is set to 0.6 m/s. R_0 is the radius at the interface between the forced-vortex and free-vortex regions while C_{u0} is the tangential velocity at the radius R_0. C_{u0} and R_0 are set, respectively, 2.94 m/s and 3.0 mm ($0.02\,D_b$). These boundary conditions represent the initial velocity distributions of the submerged vortex computed by the large-eddy simulation applied to the pump-sump model shown in Figure 4.1. Note that the tangential velocity C_{u0} of 2.94 m/s, prescribed at the inlet of the simplified model, is higher than the peak tangential velocity shown in Figure 4.1 (a). It is assumed that the vortex core is not accurately computed in the large-eddy simulation of the whole pump-sump model due to its insufficient grid resolution. Rather than taking the peak tangential velocity computed by the LES, tangential-velocity profile is reconstructed with an assumption that it is of the Rankine vortex. In this way, the tangential velocity at the interface between the forced- and free-vortex regions is determined.

For the initial flow field, both vertical velocity C_z and radial velocity are set to zero. The tangential velocity C_u is set to that of the Rankine vortex. The initial static pressure is set such that the radial pressure gradient and the centrifugal force balance with each other as shown in equation (10).

$$P_{initial} = \begin{cases} \frac{1}{2}\rho C_{u0}^2 \left(\frac{R}{R_0}\right)^2 & (r < R_0) \\ \frac{1}{2}\rho C_{u0}^2 \left\{2 - \left(\frac{R_0}{R}\right)^2\right\} & (r \geq R_0) \end{cases} \tag{10}$$

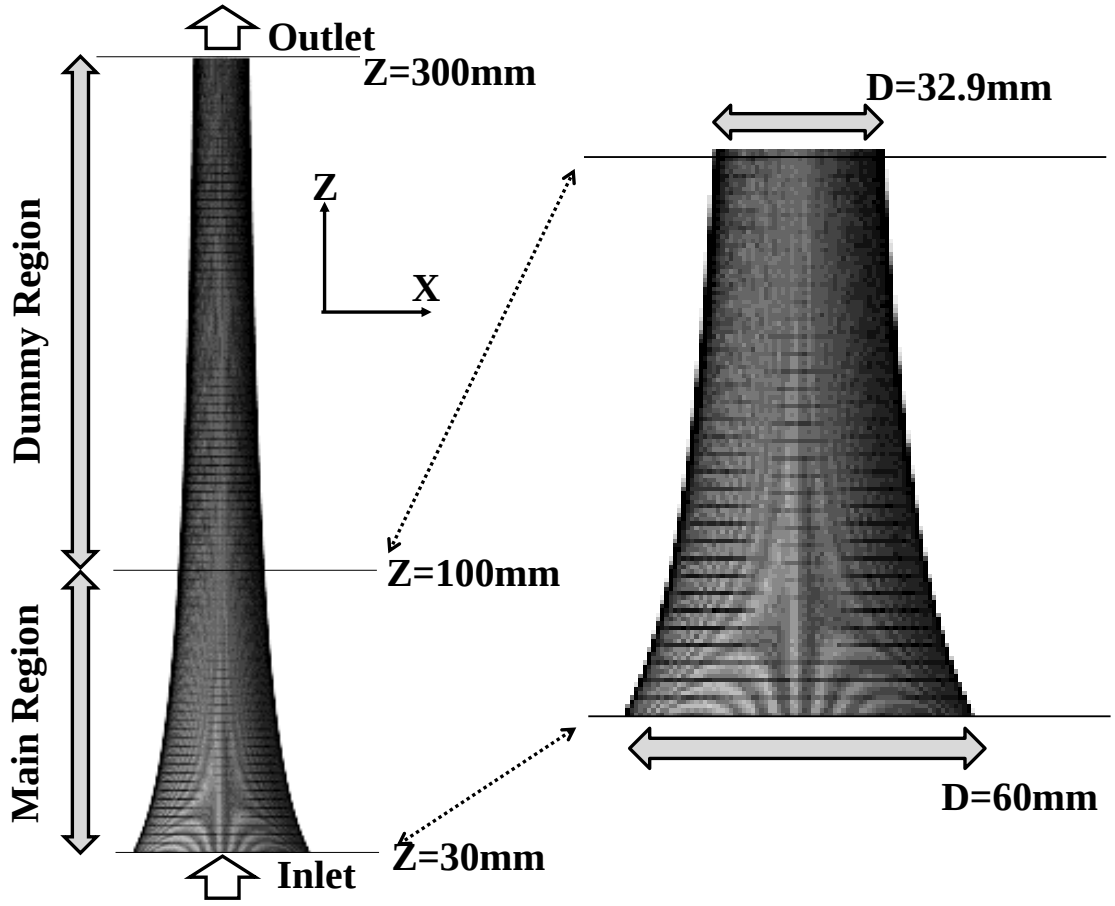

Figure 4.2. Simplified computational model for a single submerged vortex

4.3 Computational Conditions

Hereafter, the computation case described in the previous subsection will be referred to as the "baseline case 2", which is also named Case G (after the final Case F for the whole pump-sump LES). To investigate appropriate numerical parameters such as the grid resolution and the time increment, a parameter study regarding numerical conditions is firstly made for the baseline case 2. A grid-independence study, where the grid resolution is varied from 3.75 micrometers to 150 micrometres, has clarified that that grid resolution finer than 15 micrometres is required for an accurate prediction of the submerged vortex. The results of this grid-independence study will be described later in a following subsection. The effects of the time increment are also investigated by using different time increments of 3.1 micro seconds and 12 micro seconds with the grid resolution of 15 micrometres. It is found that a larger time increment (12 micro seconds) leads to underprediction of the pressure drop and that the time increment must be equal to or smaller than 3.1 microseconds to accurately predict the motions of the submerged vortex. Therefore, the grid resolution is set to 15 micrometres and the time increment is set to 3.1 microseconds for the baseline case 2 as well as for other cases described below.

In addition to the baseline case 2, the following two case studies are performed. In the first case, hereafter referred to as "Case H", the maximum tangential velocity given at the inlet boundary, C_{u0}, is varied, and in the second case, hereafter referred to as "Case I", the vertical velocity, C_{z0} is varied while the maximum tangential velocity is kept constant. In both cases, the swirl number, which is defined by the following equation (11) and represents the ratio of the angular momentum flux to the product of the radius of the vortex core and axial momentum flux, varies.

$$S \equiv \frac{\int_{r=0}^{r=R_0} 2\pi r^2 C_z C_u dr}{R_0 \int_{r=0}^{r=R_0} 2\pi r C_z C_z dr} \tag{11}$$

Case H and Case I will be, respectively, prescribed by the following parameters α and β, which are, respectively, the ratios of the tangential and vertical velocities given at the inlet

boundary to those for the baseline case 2 shown as follows.

$$\alpha \equiv C_{u0}/C_{u0\_base} \tag{12}$$

$$\beta \equiv C_{z0}/C_{z0\_base} \tag{13}$$

The swirl number defined by equation (11) increases when α is increased. Note that when α is changed, the Reynolds number, based on the initial radius of the vortex core and the initial maximum tangential velocity, as well as the dynamic pressure, based on the initial maximum tangential velocity, also changes. It is intended to investigate the effects only of the swirl number in Case I, by keeping the Reynolds number and the dynamic pressure constant. The computational cases of the large-eddy simulations of the simplified model are summarized in Table 4.4 while the swirl numbers and Reynolds numbers for Cases H and I are shown in Figure 4.3.

Table 4.4. Summary of test cases for simplified model LES.

Case Name	grid resolution [μ m]	time increment [sec.]	tangential -velocity ratio α	axial-velocity ratio β
Baseline case 2 (Case G)	15	3.1×10^{-6}	1.0 (C_{u0} = 2.94 m/s)	1.0 (C_{z0} = 0.6 m/s)
Case H	15	3.1×10^{-6}	0.05 ~ 1.50	1.0
Case I	15	3.1×10^{-6}	1.0	0.15 ~ 2.2

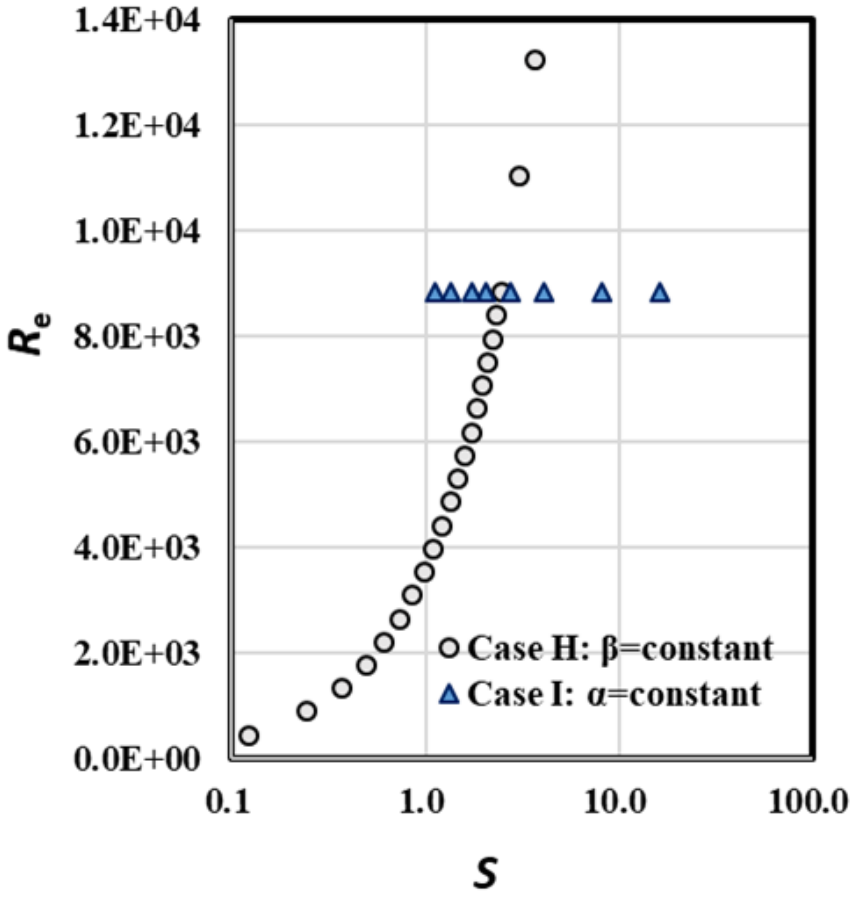

Figure 4.3. Swirl numbers and Reynolds numbers studied in Case G through Case I.

4.4 Results of Baseline Case 2

The results computed by the baseline case 2 with the grid resolution of 15 micrometres and the time increment of 3.1 microseconds will firstly be described in this subsection. The results of the parameter study made to determine the above-mentioned grid resolution and time increment will then be described in the next subsection, 4.5.

Figure 4.4 shows typical instantaneous distributions in the vertical (left) and tangential (right) velocities on the horizontal plane at a height of 60 mm ($0.40D_b$), namely 30 mm ($0.20D_b$) downstream of the inlet boundary of the simplified model, computed by the baseline case 2. The radius of the three circles shown in Figure 4.4. are, respectively, 0.6 mm ($0.004D_b$) , 1.5 mm ($0.01D_b$) and 3.0 mm ($0.02D_b$). Figure 4.5 shows variation of the difference in the static pressure at the center and that at a reference point located at a radius of 15 mm ($0.10D_b$) from the center. As mentioned above, the tangential-velocity distribution of a Rankine vortex with the core size of 3 mm ($0.02D_b$) is described at the inlet boundary. At 30 mm ($0.20D_b$) downstream of the inlet boundary, the radius of the vortex core has become smaller than 1 mm ($0.0067D_b$) and the maximum vertical velocity becomes about 5 time larger on the plane at the height of 60 mm (=$0.4D_b$), 30 mm (=$0.2D_b$) downstream of the inlet boundary, than that given at the inlet boundary. The center of the computed vortex is not located at the center of the computational domain, and is rotating similarly to the submerged vortex computed in the LES applied to the whole pump-sump model. Namely, the vortex computed by the simplified model is also in precession motion. The time averaged static-pressure drop shown in Figure 4.5 is 106.4 kPa and its root mean square (RMS) value is 3.93 kPa (3.7 % of the time-averaged value). The static pressure does not become below the vapor pressure in the experiments since cavitation takes place when the static pressure reaches the vapor pressure of water. The static pressure computed in this study becomes below the vapor pressure since the cavitation is not considered in this study as already mentioned.

Figure 4.6 compares the radial distributions of the time-averaged tangential velocity and static pressure on the horizontal plane at the height of 60 mm (=$0.4D_b$) computed in the LES

of the whole test pump sump and those in this simplified model. Note that the horizontal axis is plotted in the logarithmic scale to clarify the difference of the distributions in the vortex core. As shown in Figure 4.1, in the pump-sump computations, the size of the vortex core does not change between the horizontal planes at the heights of 30 mm ($0.2D_b$) and 60 mm ($0.4D_b$) from the bottom wall, and therefore the maximum tangential velocity does not increase between the two planes. As a result, the static pressure drops only by about 5 kPa. On the other hand, in the simplified computational model, the radius of the vortex core becomes about 0.75 mm ($0.005D_b$) on the plane at the height of 60 mm ($0.4D_b$), which is about one-fourth of that given at the inlet boundary. By the conservation of angular momentum, the tangential velocity therefore becomes 8 m/s, which is almost 5 times larger than that computed in the pump-sump model. The resulting pressure drop is 106.4 kPa, which is about 27 time larger than that computed in the pump-sump model.

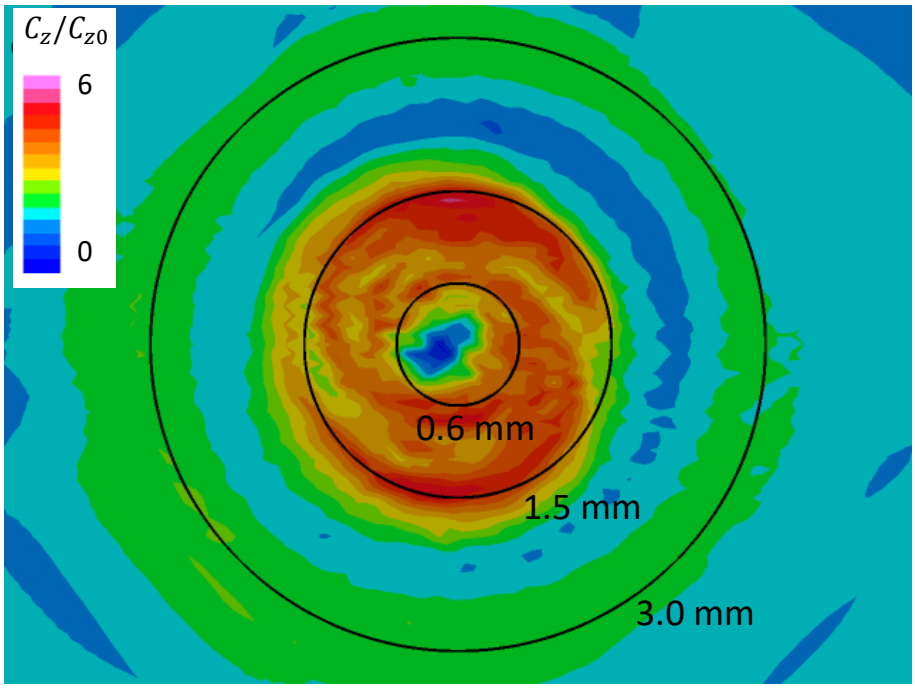

(a) vertical velocity C_z

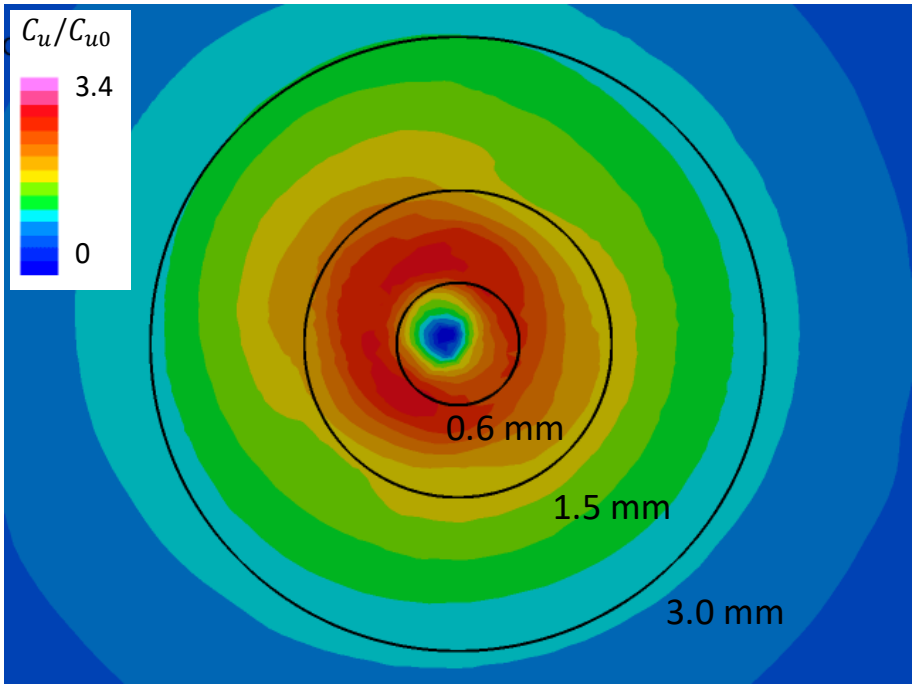

(b) tangential velocity C_u

Figure 4.4. Instantaneous vertical (left) and tangential (right) velocities on cross section at height z=60 mm ($0.4D_b$) in baseline case 2.

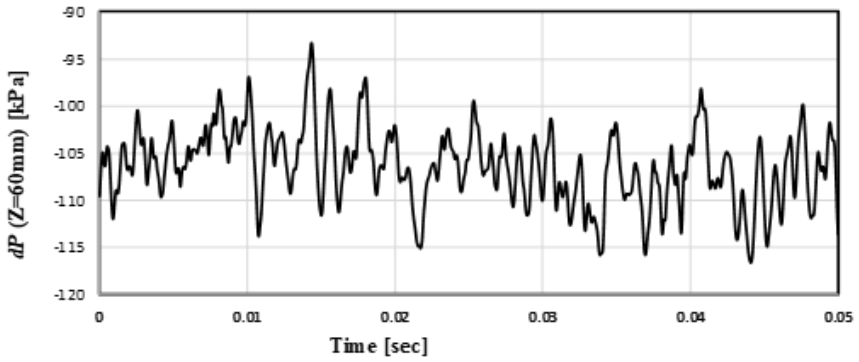

Figure 4.5. Time series of static pressure drop at center of computational domain at height of z=60 mm ($0.4D_b$) in baseline case 2.

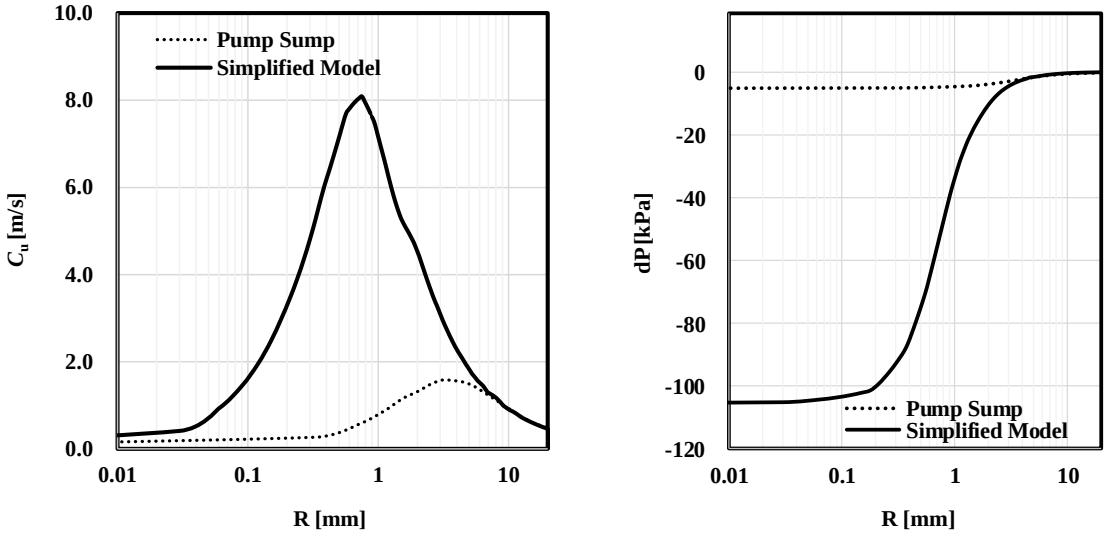

(a) tangential velocity C_u (b) static pressure

Figure 4.6. Comparisons of time and circumferentially averaged radial distribution of tangential velocity and static pressure drop on horizontal plane at Z = 60 mm ($0.4D_b$) in pump-sump (baseline case) and simplified model (baseline case2).

4.5 Effects of Grid Resolution and Time increment on Stretch of Submerged Vortex

The grid-dependence tests are performed for the baseline case 2 where the grid resolution is varied in a range of 3.75 ~ 150 micrometres. Figure 4.7 shows the time series of the pressure drops computed with different grid resolutions. The pressure drops are almost the same as that for the 15 micrometres case if the grid resolution is finer than 15 micrometres while they are considerably smaller than that with 15 micrometres case if the grid resolution is coarser than 30 micrometres. Figure 4.8 compres the static pressure drop with different grid resolutions in the pump sump model and the simplified model. It is therefore decided to use the computational grid with the resolution of 15 micrometres in this study.

While it is set to 3.1 micro seconds in the grid-dependence tests described above, the time increment is also varied to investigate its effects on the vortical dynamics. Figure 4.9 compares time series of the pressure drops computed with different time increments. In this test, grid resolution is set to 15 micrometres. The pressure drop is considerably decreased with the time increment of 12 micro seconds, which is about four times larger than the selected time increment of 3.1 micro seconds. Figure 4.10 compares the instantaneous distributions of the tangential velocity C_{u} on the cross section at height Z=60 mm ($0.4D_{\mathrm{b}}$). The vortex core is enlarged with the larger time increment where the tangential velocity is lower (right in Figure 4.10) than the one with the smaller time increment (left in Figure 4.10), which has resulted in the smaller pressure drop as confirmed In Figure 4.9. Figure 4.11 and Figure 4.12 respectively show a time series and frequency spectrum of the axial velocity at the center on the cross section at height of Z=60 mm ($0.4D_{\mathrm{b}}$). In Figure 4.11 and Figure 4.12, the axial velocity is normalized by the axial velocity, C_{z0}, given at the inlet boundary for baseline case 2. There is a peak of the velocity fluctuation at about 1 kHz in the case with the smaller time increment. This peak is shifted to a lower frequency and the amplitude of the peak increases in the case with the larger time increment. The motions of vortex cannot be resolved with the larger time increment, and as a result, the computed velocity fluctuation

has a larger scale (a lower frequency) and a larger amplitude. The larger velocity fluctuation has enlarged the vortex core.

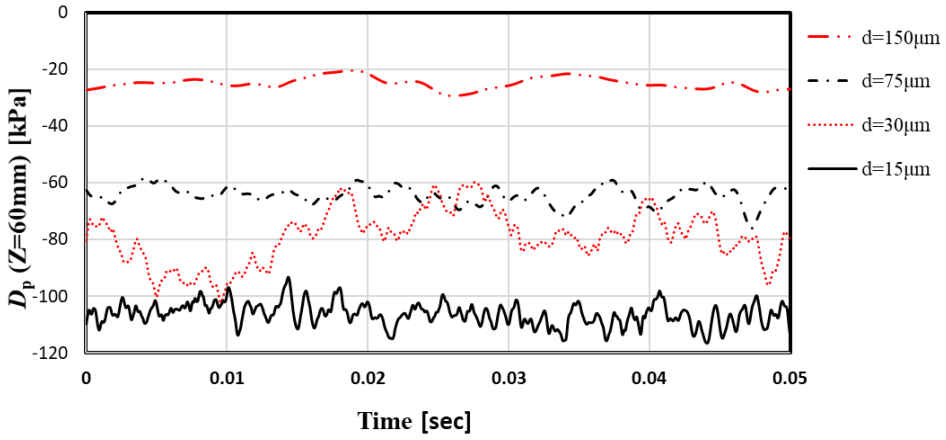

(a) grid resolution of 150, 75, 30 and 15 micrometres

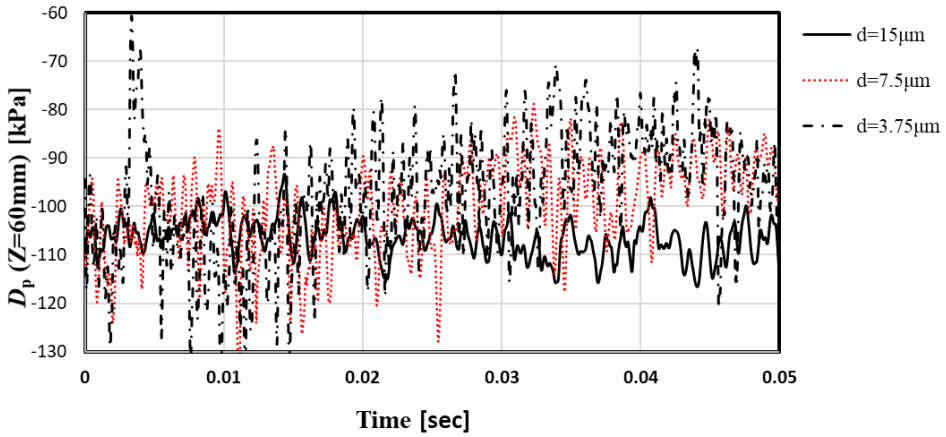

(b) grid resolution of 15, 7.5 and 3.75 micrometres

Figure 4.7. Time series of static pressure at center of computational domain at Z=60 mm ($0.4D_b$) in baseline case 2 with different grid resolutions.

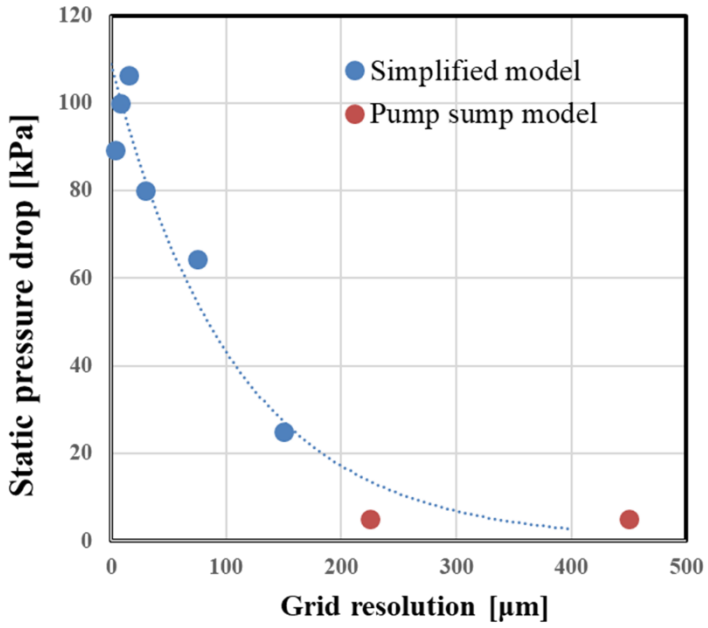

Figure 4.8. Static pressure drop at vortex core of a submerged vortex computed in the pump sump model and the simplified model

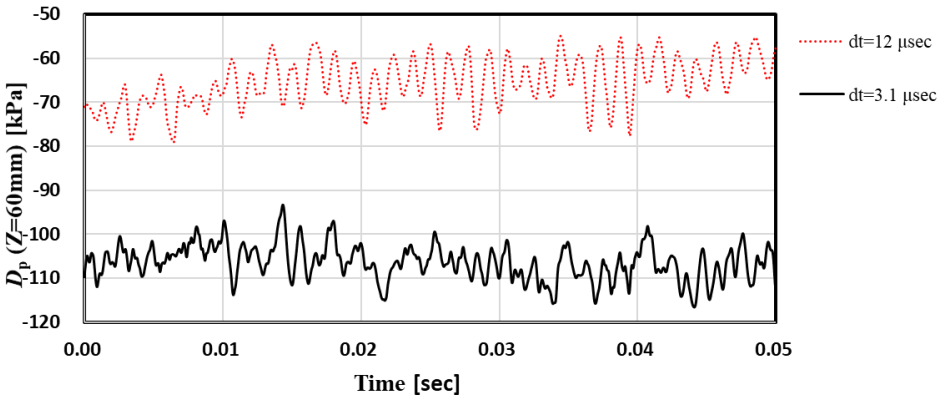

Figure 4.9. Time series of static pressure at center of computational domain at Z=60 mm ($0.4D_b$) in baseline case 2 with different time increments.

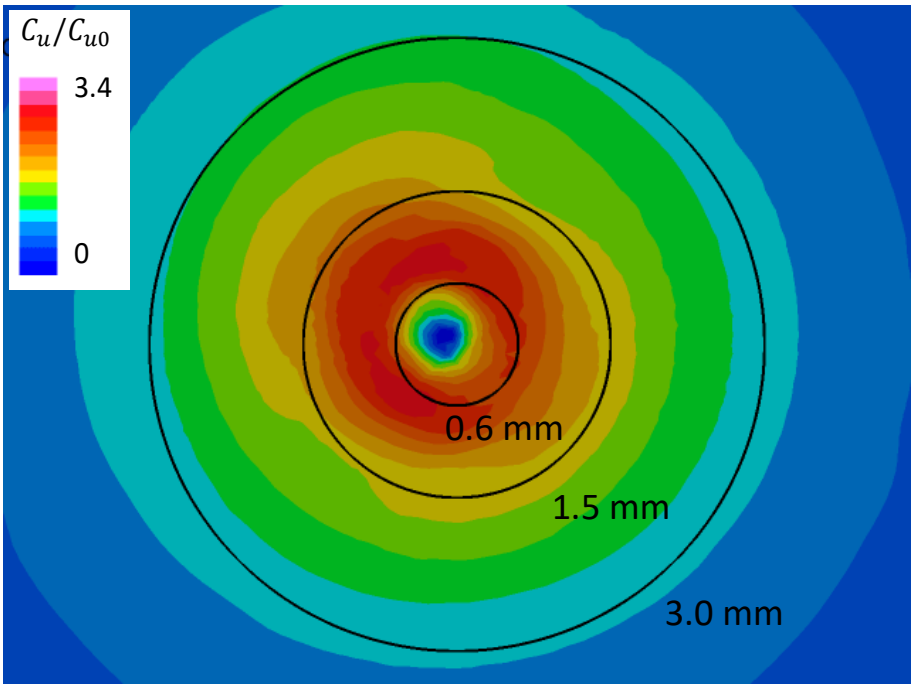

(a) dt = 3.1 microseconds

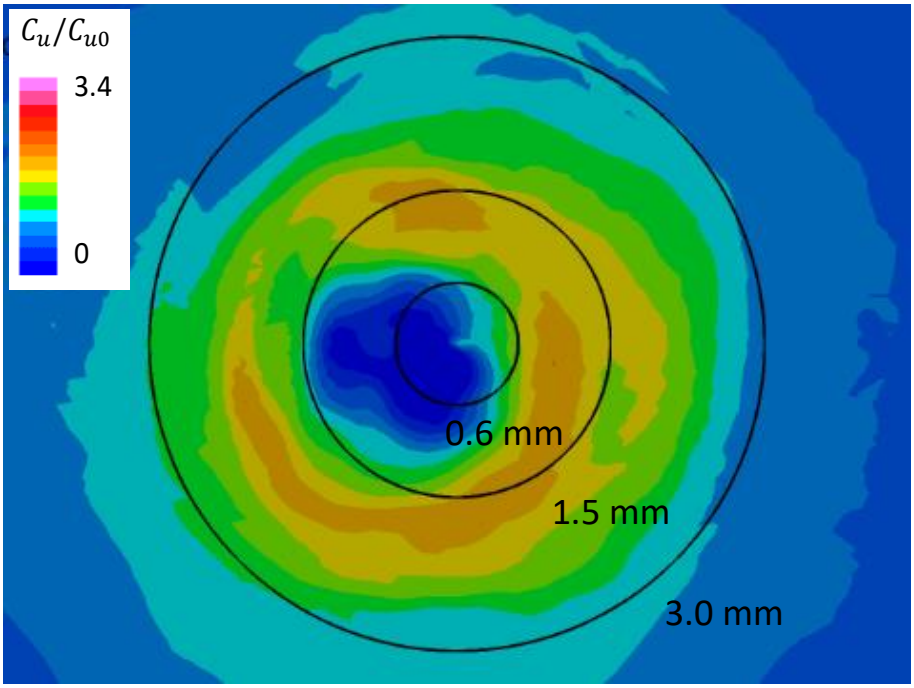

(b) dt = 12 microseconds

Figure 4.10. Instantaneous tangential velocity on cross section at height Z=60 mm ($0.4D_b$) in baseline case 2 with different time increment.

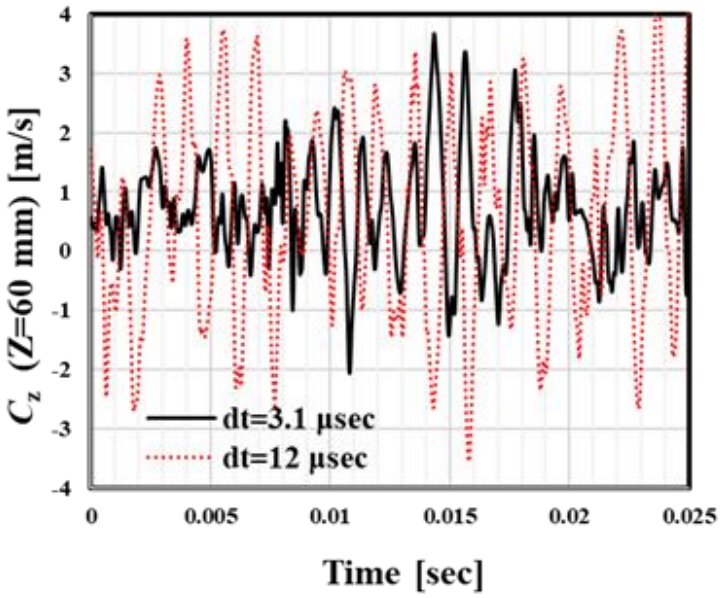

Figure 4.11. Fluctuations of axial velocity at the center on the cross section at height Z=60 mm ($0.4D_b$) in the baseline case 2 with the different time increment.

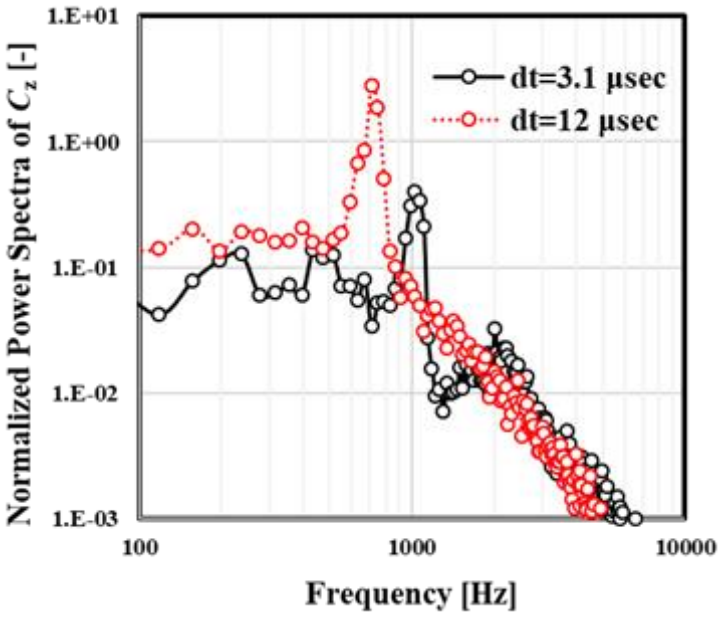

Figure 4.12. Frequency spectra of axial velocity at the center on the cross section at height Z=60 mm ($0.4D_b$) in the baseline case 2 with the different time increment.

4.6 Effects of Swirl Velocity on Growth of Vortex

The results computed by changing the maximum tangential velocity C_{u0} given at the inlet boundary will be described in this subsection to understand the formation condition of a submerged vortex in a pump sump. The parameter α, which represents the tangential-velocity ratio given at the inlet boundary as described in subsection 4. 3, is proportional to the swirl number S defined by equation (11). α is varied in a range of 0.05 ~ 1.5, which corresponds to the swirl-number range of S = 0.12 ~ 3.68. The Reynolds number and dynamic pressure both defined by the initial maximum tangential velocity also change with the change of α. Figure 4.13 shows the relationships between the static-pressure drop on the plane at the height of 60 mm ($0.4D_b$) and the value of parameter α. Figure 4.13 (a) shows the absolute value of the pressure drop while Figure 4.13 (b) shows the pressure drop normalized by the dynamic pressure computed by the given maximum tangential velocity C_{u0} for each case.

The radial distributions of the tangential and vertical velocities and static pressure are analyzed in detail for typical 12 cases (out of 22 total cases computed). Figure 4.14 shows the time averaged tangential (left) and vertical (right) velocity on the horizontal plane at the height of 60 mm ($0.4D_b$). The tangential and vertical velocities are, respectively, normalized by C_{u0} and C_{z0} given at the inlet boundary in each case. The tangential-velocity distributions of the free vortex and Burgers vortex [28] are also plotted for reference in these figures. Burgers vortex is an asymptotic solution of the vortex stretched under a constant vertical-velocity gradient and is given by the following equation.

$$C_u = \frac{C_{u0}R_0}{R}\left\{1 - exp\left(-\frac{R^2}{R_1^2}\right)\right\} \tag{14}$$

$$R_1^2 = \frac{4\nu}{\left(\frac{\partial C_z}{\partial z}\right)} \tag{15}$$

where R_0 and C_{u0} is the initial radius of the vortex core and the tangential velocity at the radius of R_0. Burgers vortex is an ideal vortex that is fully stretched in the vertical direction, and thus equation (14) does not depend on the height Z. The velocity distribution computed

by this study should have become the one represented by Burgers vortex if the simplified model had an enough length for the stretch of the vortex and the steady state were maintained. However, the velocity distributions of the vortex computed in the simplified model are remarkably different from the one of Burgers vortex as will be detailed later in this subsection.

Figure 4.15 shows the time-averaged distributions of the static pressure difference between the center and a reference point at a radius of 10 mm ($0.067D_b$) on the horizontal plane at the height of 60 mm ($0.4D_b$) in these 12 cases. The absolute values of the pressure drop are plotted in the left figures while those normalized by the dynamic pressure that corresponds to the maximum tangential velocity C_{u0} given at the inlet boundary are plotted in the right figures. By analyzing these plots, it is found that the following equation, which represents the balance between the pressure gradient and the centrifugal force, holds for all the cases.

$$\frac{\partial P}{\partial r} \cong -\rho \frac{C_u^2}{r} \tag{16}$$

The static pressure at radius R can be obtained by integrating equation (16) and it is represented by the following equation (17).

$$P(R) \cong -\int_{r=R}^{r=\infty} \rho \frac{C_u^2}{r} dr \tag{17}$$

The larger the tangential velocity is, the larger the pressure drop at the center becomes. In these case studies, the maximum tangential velocity C_{u0}, given at the same radius R_0 on the inlet boundary, becomes larger with increasing value of α. The absolute value of the pressure drop plotted in the left figures represents combined effects of the increase in the maximum tangential velocity given at the inlet boundary and those of the vortex stretch while the normalized pressure drop plotted in the right figures purely represent those of the vortex stretch. By carefully investigating the changes in these distributions of the velocities and static pressure, and change in the flow fields by movies (not shown in this paper), the conditions of formation process of a submerged vortex can be classified into the following four regimes:

(1) Steady-state condition

The vortex keeps a steady state for α smaller than 0.4, which corresponds to the swirl number smaller than 0.98. The distribution of the tangential velocity can be represented by that of the Rankine vortex. With increasing value of α, the radius of the vortex core becomes smaller and for the maximum α of 0.4, it becomes about 2 mm ($0.013D_b$). At the radius of about 2 mm ($0.013D_b$), which is outside the vortex core, the tangential velocities are about 2.6 times larger than the vertical velocity for α = 0.4. The pressure drop is 4 kPa for α = 0.4, which is only 4 % of the atmospheric pressure.

(2) Transitional-state condition

For α larger than 0.45, the vortex starts precession motion and it simultaneously starts alternative stretching and shrinking in the vertical direction. The stretching leads to a smaller radius of the vortex core, resulting in a considerably larger tangential velocity and pressure drop. Under this condition, the tangential-velocity distribution can no longer be represented by that of the Rankine vortex, and the radius where the tangential velocity takes its maximum moves towards the center, and it becomes substantially smaller (0.5 mm =$0.033D_b$ ~ 1.5 mm=$0.010D_b$) than that of the Rankine vortex. As a result, the pressure drop rapidly increases with increasing value of α. The pressure drop for α = 0.6 is about 40 kPa, which is ten times larger than that under the steady-state condition. However, the pressure drop in this condition is still smaller than the atmospheric pressure.

(3) Equilibrium-state condition

For α = 0.65 ~ 0.85, which corresponds to the swirl number of 1.59 ~ 2.08, the absolute value of the pressure drop keeps increasing with increasing value of α. On the other hand, the normalized pressure drops are almost constant and the radius where the tangential velocity takes its maximum does not move. The normalized tangential velocity becomes constant with increasing value of α. Under this condition, the effects of the vortex stretch due to the vertical acceleration and those of the centrifugal force presumably balance with each other, and therefore, no further shrink of the vortex core occurs.

(4) Expanding-state conditions

For α = 1.00 ~ 1.50, which corresponds to the swirl number of 2.45 ~ 3.68, the absolute values of the pressure drop slightly increase with increasing value of α. However, the size of the vortex core increases with increasing value of α, resulting in a sudden decrease of the normalized pressure drop. The tangential-velocity distributions return to the one close

to the Rankine vortex as is under the steady-state condition for α smaller than 0.4. Note that α = 1.0 corresponds to the baseline case 2 described in subsection 4.4. Figure 4.16 shows the change in the radius of the vortex core on the horizontal plane at the height of 60 mm (=0.4D_b) with the change in the value of α.

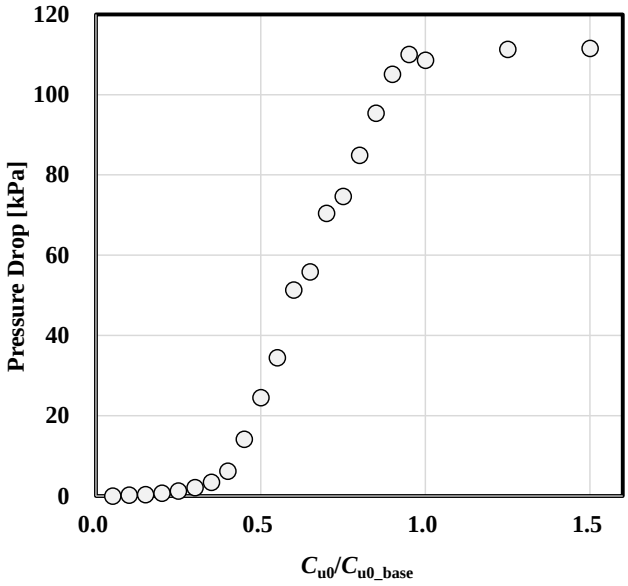

(a) Pressure drop

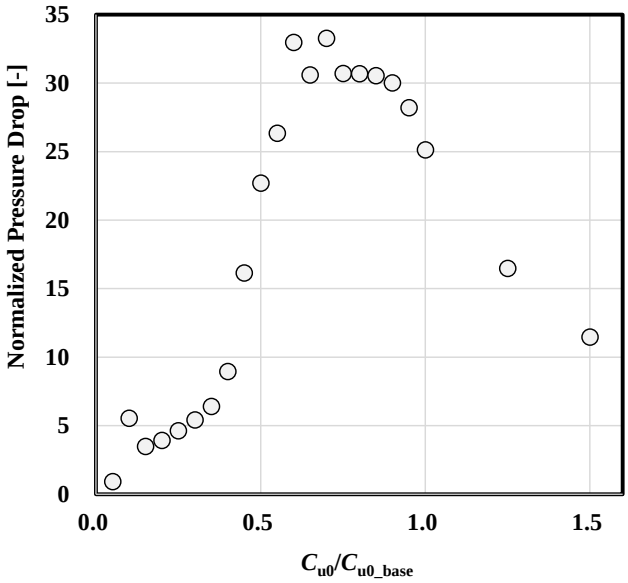

(b) Normalized pressure drop

Figure 4.13. Effects of circulation given at inlet boundary on pressure drops at center on cross section at Z = 60 mm ($0.4D_b$).

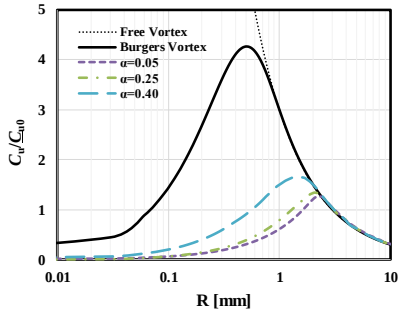

(a-1) C_u with α of 0.05, 0.25 and 0.40

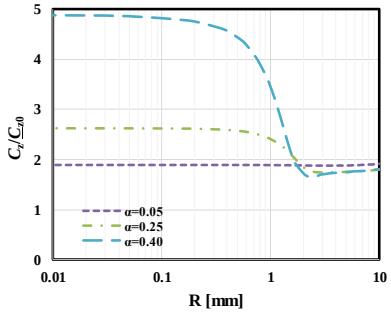

(b-1) C_z with α of 0.05, 0.25 and 0.40

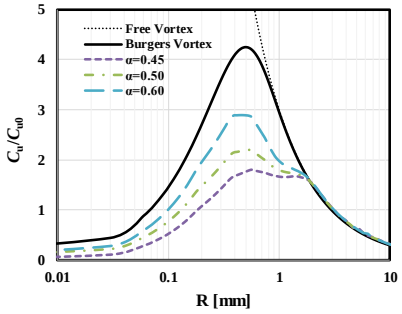

(a-2) C_u with α of 0.45, 0.50 and 0.60

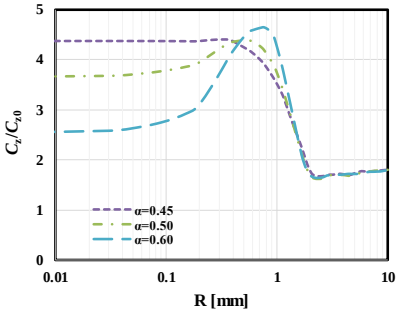

(b-2) C_z with α of 0.45, 0.50 and 0.60

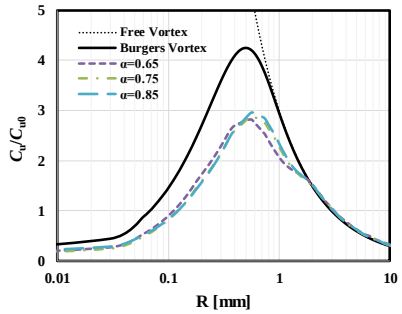

(a-3) C_u with α of 0.65, 0.75 and 0.85

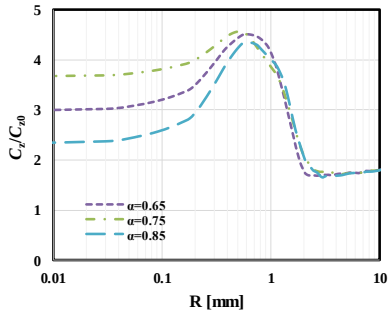

(b-3) C_z with α of 0.65, 0.75 and 0.85

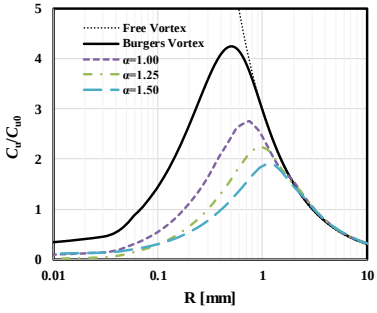

(a-4) C_u with α of 1.00, 1.25 and 1.50

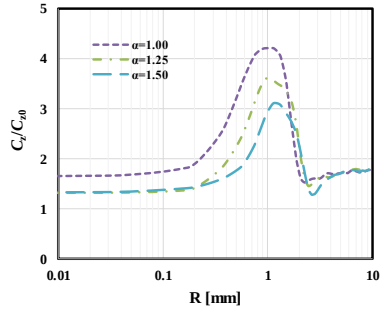

(b-4) C_z with α of 1.00, 1.25 and 1.50

Figure 4.14. Comparisons of radial distributions of tangential (left) and vertical (right) velocities on horizontal plane at height of 60 mm ($0.4D_b$) in Case H.

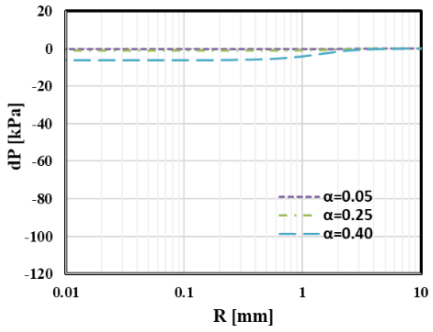

(a-1) dP with α of 0.05, 0.25 and 0.40

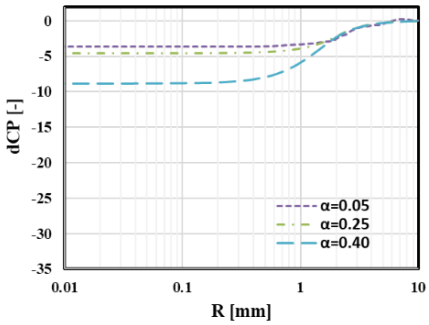

(b-1) dC_P with α of 0.05, 0.25 and 0.40

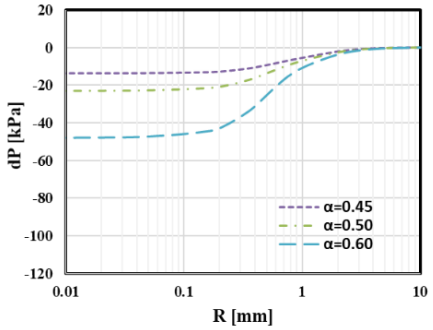

(a-2) dP with α of 0.45, 0.50 and 0.60

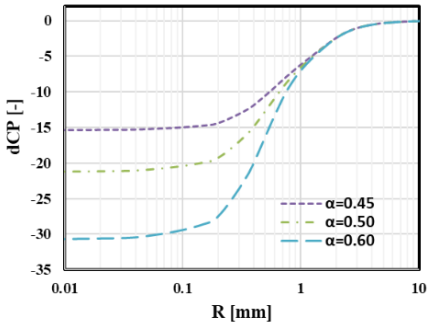

(b-2) dC_P with α of 0.45, 0.50 and 0.60

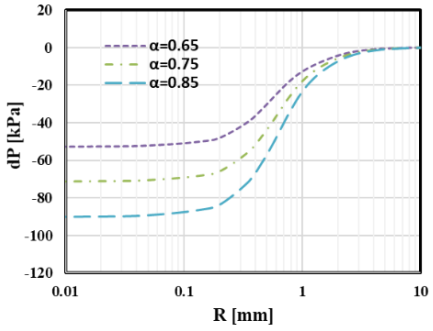

(a-3) dP with α of 0.65, 0.75 and 0.85

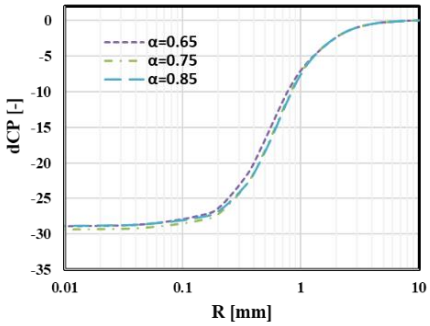

(b-3) dC_P with α of 0.65, 0.75 and 0.85

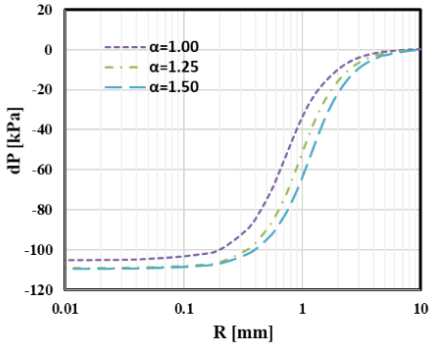

(a-4) dP with α of 1.00, 1.25 and 1.50

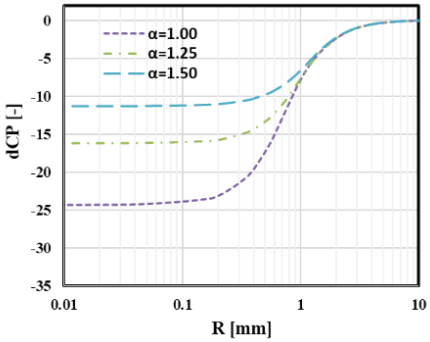

(b-4) dC_P with α of 1.00, 1.25 and 1.50

Figure 4.15. Comparisons of radial distributions in pressure drop (left) and normalized pressure drop (right) on horizontal plane at height of 60 mm ($0.4D_b$) in Case H.

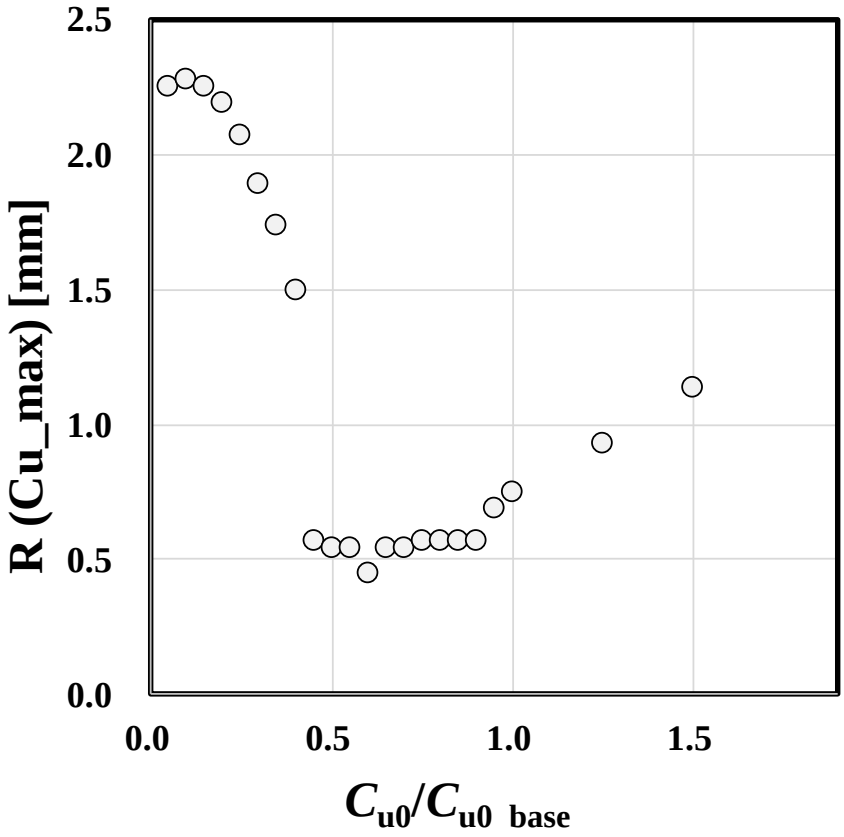

Figure 4.16. Radius of vortex core computed on horizontal plane at the height of 60 mm ($0.4D_b$) in case H.

4.7 Effects of Axial Velocity on Growth of Vortex

In case I, the vertical velocity C_{z0} given at the inlet boundary is varied while the maximum tangential velocity C_{u0} and the radius of the vortex core R_0 are kept constant. While both swirl number and Reynolds number change in Case H described in the previous subsection, only the swirl number changes in Case I. Therefore, the effects only of the swirl number on the dynamics of the vortex should appear in this case, which will be described in this subsection.

Figure 4.17 plots, against the swirl number, S, the normalized pressure drop on the horizontal plane at the height of 60 mm ($0.4D_b$). The results from Case H and those from Case I fall in a line. The agreement of the normalized pressure drop in the two cases indicates that the normalized pressure drops are little affected by the Reynolds number in the range investigated in this study, and it is determined solely by the swirl number. With decreasing vertical velocity given at the inlet boundary, which corresponds to increase in the swirl number, the normalized pressure drop rapidly increases until the swirl number reaches 1.25. Beyond this swirl number, the normalized pressure drop starts to decrease. In Case I, the equilibrium-state condition identified in Case H is not clearly observed. However, it is confirmed from both results from Case H and Case I that the vortex is in precession motion accompanied by alternative vertical stretch and shrink in a relatively narrow range of the swirl number from 1.25 to 3.0. Only when this condition is met, the vortex grows and as a result, the static pressure at the vortex core substantially decreases.

Finally, in actual pump sumps, cavitation is likely to occur in the vortex core, which is not considered in the present study. When cavitation occurs in its core, the vortex becomes presumably weakened because the larger mass of water moves outward. The narrow peak of the normalized pressure drop shown in Figure 4.17 may also be changed due to the cavitation. Unsteady motions of the submerged vortex subject to cavitation phenomena will be investigated in the future study.

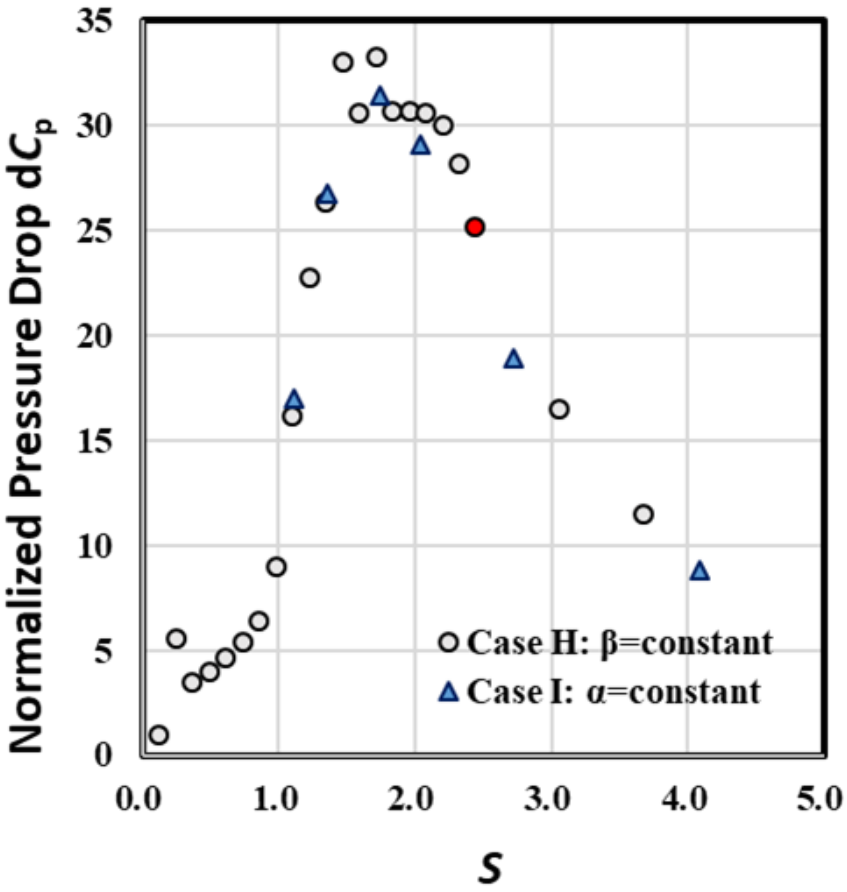

Figure 4.17. Normalized pressure drop plotted against swirl numbers in case H and case I. Mark in red indicates baseline case 2.

4.8 Stretch of Vortex Core due to Unsteady Vortical Motion

In subsection 4.6, it is shown that a sudden pressure drop takes place when the vortex starts unsteady motion. The unsteady motion of the vortex that leads to the enhanced pressure drop will be investigated in detail in this subsection. Figure 4.18 shows the frequency spectra of the normalized axial-velocity fluctuation at the center of the plane at the height Z=60 mm ($0.4D_b$) in Case H. The frequency spectrum with $\alpha = 0.3$, for which the vortex is still steady, has no significant power. The frequency spectra with $\alpha = 0.4$ and 0.6 begin to have significant power. Especially, the frequency spectrum with $\alpha = 0.6$ obeys the -5/3 power law in the frequency range of 100 Hz and 4 kHz, which is the theoretical decay of the turbulence kinetic energy in the inertial subrange. The frequency spectra with α =0.75 and 1.0 in Figure 35 (b) also obey the -5/3 power law. This indicates the vortex with α equal to, or larger than, 0.6 is in a turbulent motion. Figure 4.19 shows instantaneous distributions of the tangential and radial velocities at height Z=60 mm ($0.4D_b$) with $\alpha = 0.6$. The vortex is not homogeneous in the tangential direction. Figure 4.20 shows distributions of the fluctuating tangential and radial velocities with $\alpha = 0.6$. The fluctuating velocity is defined by the difference between instantaneous and time-averaged velocities. A negative correlation between the fluctuating tangential and radial velocities is confirmed at around R=0.6 mm ($0.4D_b$). Namely, there is an inward flow ($C_r < 0$) where the tangential velocity C_u is larger than the average. On the other hand, there is an outward flow ($C_r > 0$) where the tangential velocity C_u is smaller than the average. These negative correlations indicate that the angular momentum is transported inward at this instance. Figure 4.21 shows the radial distribution of the product of the fluctuating tangential and radial velocities. The radial distribution is computed by taking an average over the tangential direction at each radius, and it is normalized by the maximum RMS (Root Mean Square) of the tangential and radial velocities, which are also computed in the tangential direction. Figure 4.22 shows the radial distributions of RMS of the tangential and radial velocities. The maximum values in the RMS of the tangential and radial velocities are, respectively, 0.19 m/s and 0.50 m/s. The tangentially averaged product of the fluctuating

tangential and radial velocities has a negative cross correlation peaked at around R = 0.6 mm ($0.004D_b$). This negative cross correlations between the tangential and radial velocities transports the angular momentum inward, just as in a turbulent boundary layer, turbulent eddies transport streamwise momentum towards the wall, which in this case leads to a remarkable growth of the vortex core.

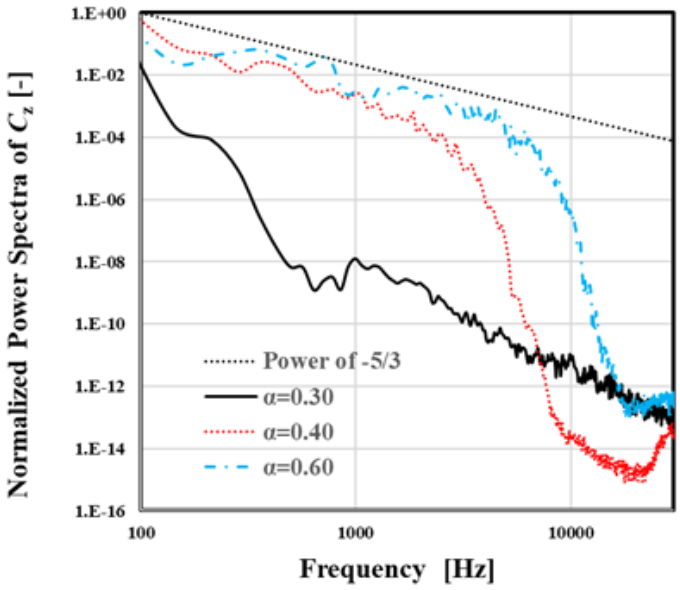

(a) $\alpha = 0.3, 0.4, 0.6$

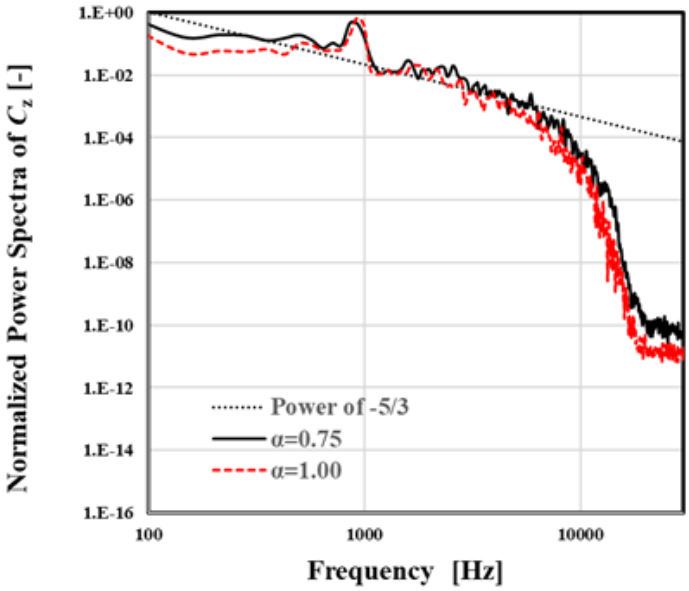

(b) $\alpha = 0.75, 1.0$

Figure 4.18. Frequency spectra of normalized axial-velocity fluctuation at center on horizontal plane at height Z = 60 mm ($0.4D_b$) with α of 0.3, 0.4, 0.6, 0.75 and 1.0.

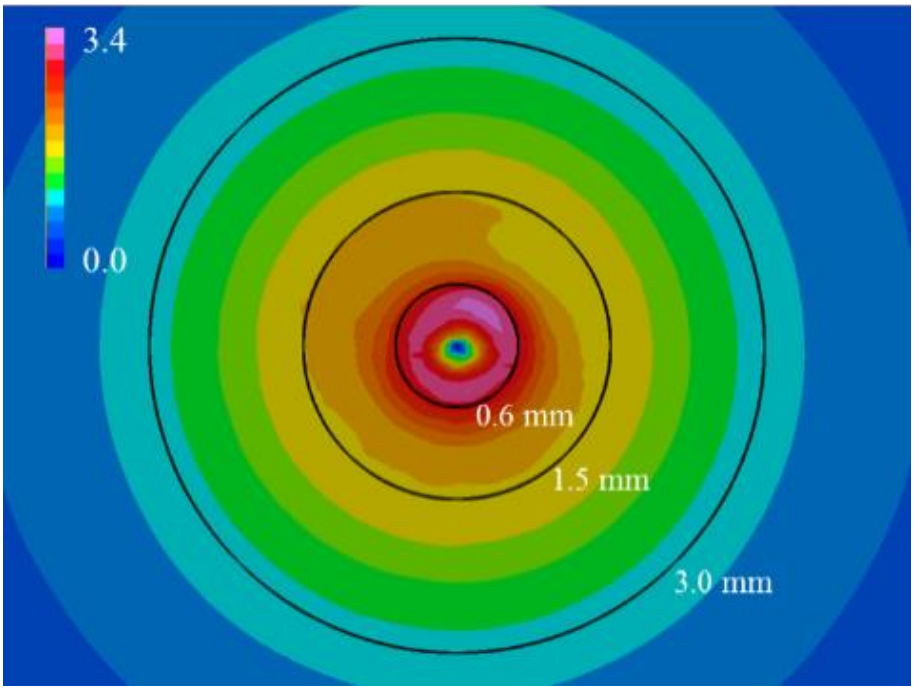

(a) Tangential velocity C_u

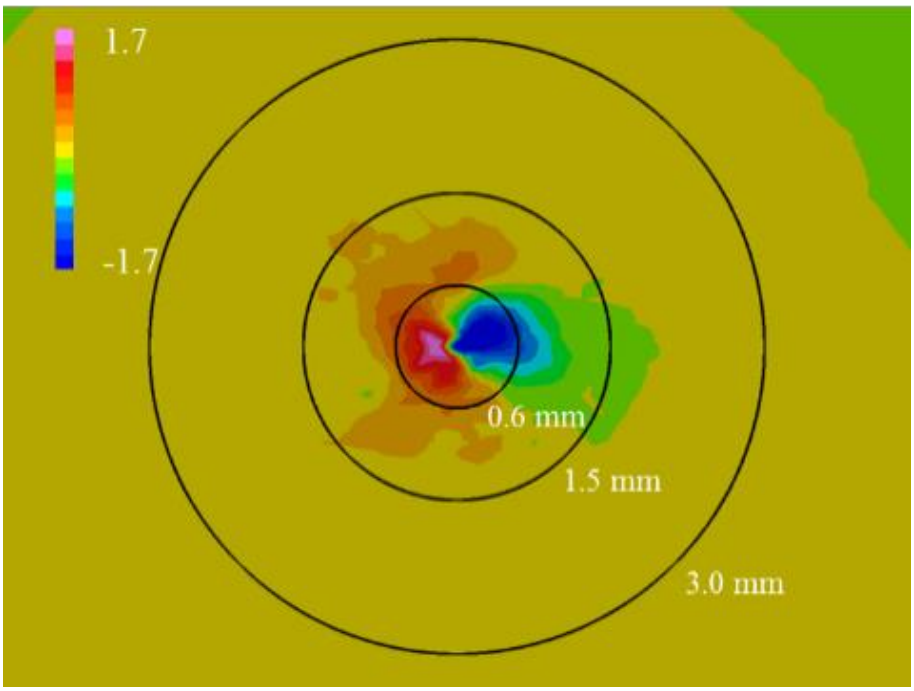

(b) Radial velocity C_r

Figure 4.19. Instantaneous distributions of tangential and radial velocities on horizontal plane at height Z = 60 mm ($0.4D_b$) with α of 0.6.

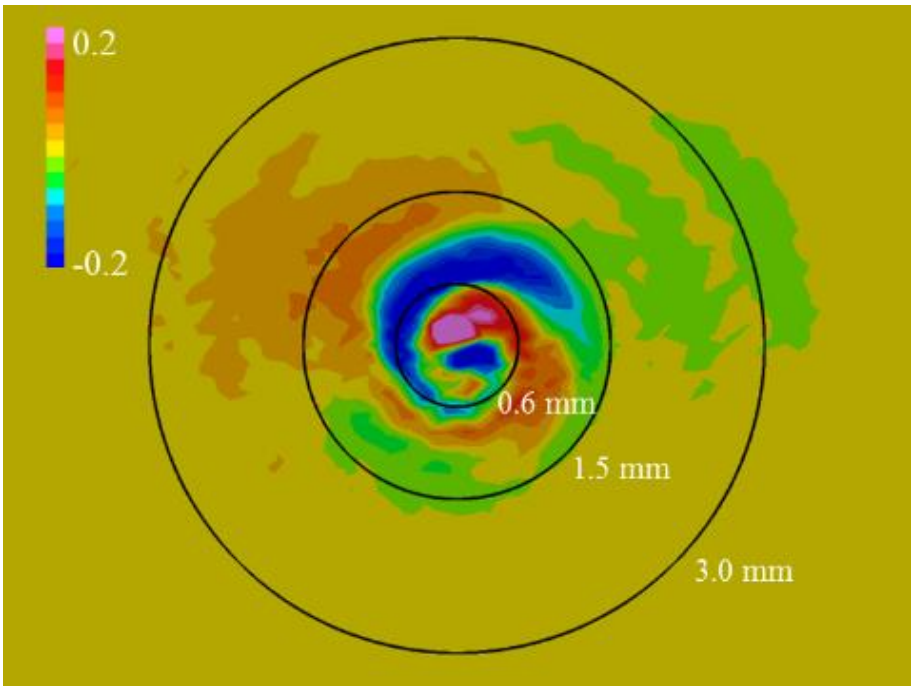

(a) Tangential velocity dC_u

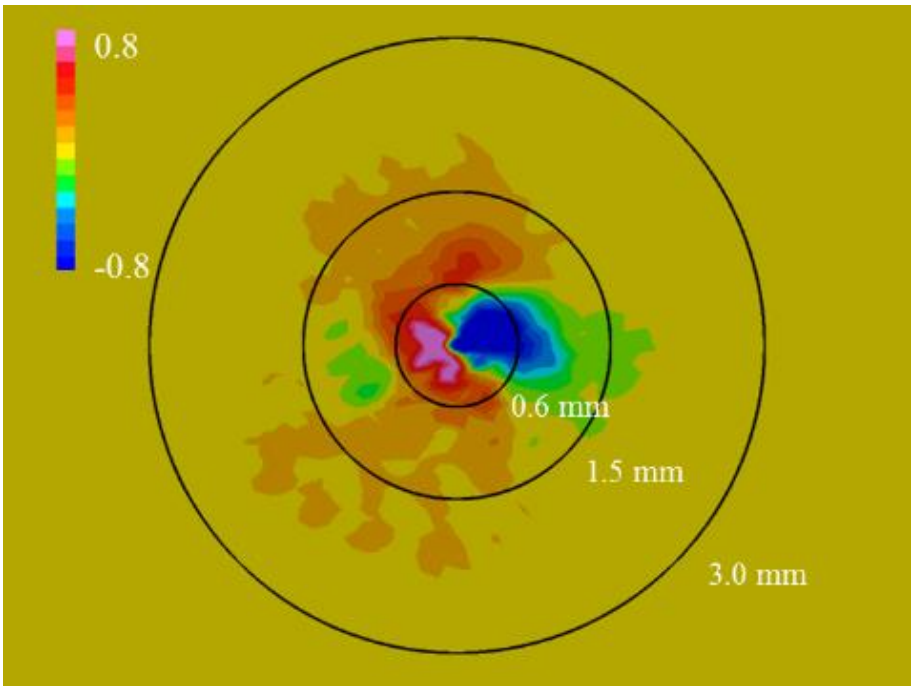

(b) Radial Velocity dC_r

Figure 4.20. Instantaneous distribution of fluctuating tangential and radial velocities on horizontal plane at height Z = 60 mm ($0.4D_b$) with α of 0.6.

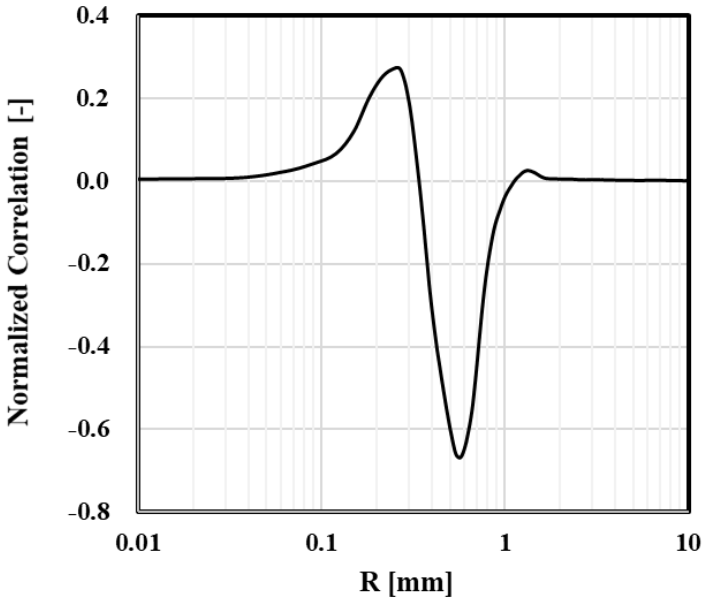

Figure 4.21. Tangentially averaged product of fluctuating tangential and radial velocities on horizontal plane at height Z = 60 mm ($0.4D_b$) with α of 0.6.

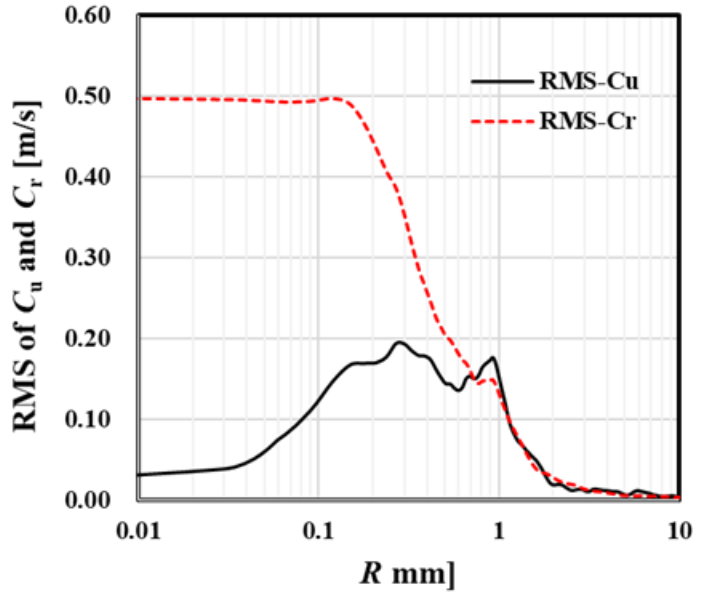

Figure 4.22. RMS of tangential and radial velocities on horizontal plane at height Z = 60 mm ($0.4D_b$) with α of 0.6.

Chapter 5. Conclusions

To identify the origin of the suction vortices that are formed in a pump sump, wall-resolved LES is performed for a whole pump-sump model with three different wall boundary conditions for the approaching boundary layers to the suction pipe. These large-eddy simulations reveal that the fundamental origin of a submerged vortex is the vorticity in the mean shear of the approaching boundary layer. The computation continued for a long period of time period has identified the formation mechanism of a submerged vortex: the vorticity in the approaching boundary layer with its axis originally aligned in the lateral direction changes its axis to the radial direction around the projected center of the suction pipe due to the geometrical asymmetry of the pump sump, and then, it further changes its axis in the vertical direction in the flow converging to the inlet of the suction pipe, and finally, by the vertical acceleration of the flow, the vortex is stretched and, as a result, a strong submerged vortex is formed. On the other hand, the origin of an air-entrained vortex has been identified as the vertical vorticity in the separated flow behind the suction pipe. When it is sucked toward the inlet of the suction pipe, the vortex is stretched in the axial direction, and as a result, an air-entrained vortex is formed.

While the origin and formation process of suction vortices have been identified in the LES applied to the whole pump-sump model, the computed pressure drop of the submerged vortex is about 5kPa, which is too small to explain the occurrence of cavitation as observed in the model test. To overcome this underprediction of the pressure drop, LES of the internal flows in a simplified computational model are performed by using computational grid with a sufficiently fine resolution. The dynamics of the vortex core, including its pressure drop, has been clarified by the case studies where the tangential velocity and/or vertical velocity given at the inlet boundary of the computational model are varied. The pressure drop of the submerged vortex, computed by prescribing the maximum tangential velocity of 2.94 m/s at the radius of 30 mm ($0.2D_\mathrm{b}$) at the inlet boundary, which corresponds to the initial condition found in the pump-sump model LES, exceeds 100 kPa. Grid resolution equal to, or finer than, 0.015 mm ($1.0 \times 10^{-4} D_\mathrm{b}$) is needed for computing dynamics of the vortex with the core size of about 0.5 mm ($0.0033D_\mathrm{b}$). Flow structures of a submerged vortex can be classified by the

swirl number near the bottom wall, defined by the ratio of the angular momentum to the product of the axial momentum and the radius of the vortex core. The vortex keeps a steady state for the swirl number smaller than 0.98, resulting in a large core size and a small pressure drop. The vortex starts precession motion with the swirl number larger than 1.25. This precession motion leads to alternative vertical stretching and shrinking, which results in a sudden increase of the pressure drop normalized by the dynamic pressure corresponding to the maximum tangential velocity given at the inlet boundary. The negative peak of the cross-correlation of tangential and radial velocities that appears near the vortex core reveals that fluctuating velocities near the vortex core transport angular momentum inward. For the swirl number between 1.59 ~ 2.08, the radius of the vortex core as well as the pressure drop normalized by the maximum tangential velocity given at the inlet boundary keep unchanged since the effects of the vortex stretch and the centrifugal force by the vortex rotation are balanced with each other. For the swirl number larger than 2.45, the vortex core becomes larger and the normalized pressure drop suddenly decreases again.

References

[1] Ansar, M. and Nakato, T., 2001, "Experimental Study of 3d Pump-intake Flows with and without Cross Flow," Journal of Hydraulic Engineering, **127** (10), pp. 825-834.

[2] Ansar, M., Nakato, T. and Constantinescu G. S., 2002, "Numerical Simulations of Inviscid Three-Dimensional Flows at Single- and Dual-Pump Intakes," Journal of Hydraulic Research, **40** (4), pp. 461-470.

[3] Constantinescu, G. S. and Patel, V. C., 2000, "Role of Turbulence Model in Prediction of Pump-Bay Vortices," Journal of Hydraulic Engineering, **126** (5), pp 387-391.

[4] Okamura, T., Kamemoto. K. and Matsui. J., 2007, "CFD Prediction and Modeling Experiment of Suction Vortices in Pump Sump," Proc. 9th AICFM (Jeju, Korea), No. AICFM9-053.

[5] Shin, B., 2018, “Numerical Study of Effect of Flow Rate on Free Surface Vortex in Suction Sump,” Transaction of JSCES, Paper No. 20180010.

[6] Wu, P., Munoz, D. H., Constantinescu, G. and Qian, C., 2019, “Two-phase flow DES and URANS simulations of pump-intake bay vortices,” Journal of Hydraulic Research, DOI: 10.1080/00221686.2018.1555552.

[7] Strasser, W., 2007, “Discrete Particle Study of Turbulence Coupling in a Confined Jet Gas-Liquid Separator,” ASME, Journal of Fluids Engineering, **130** (1), pp. 011101.

[8] Tokyay, T. E., and Constantinescu, S. G., 2006, “Validation of a large eddy simulation model to simulate flow in pump intakes of realistic geometry,” Journal of Hydraulic Engineering, **132**, no. 12, pp. 1303-1315.

[9] Nakayama, A. and Hisasue, N., 2010, “Large eddy simulation of vortex flow in intake channel of hydropower facility,” Journal of Hydraulic Research, **48** (4) 415-427.

[10] Chuang, W. L., Hsiao, S. C., and Hwang, K. S., 2014, "Numerical and Experimental Study of Pump Sump Flows," Mathematical Problems in Engineering, Volume **2014**, Article ID 735416.

[11] Pan, Q., Zhao, R., Wang, X., Shi, W., and Zhang, D., 2019, “LES study of transient behavior and turbulent characteristics of free-surface and floor-attached vortices in pump sump,” Journal of Hydraulic Research, **57** (5), 733-743.

[12] Germano, M., Piomelli, U., Moin, P. and Cabot, William H., 1991, "A Dynamic Subgrid-Scale Eddy Viscosity Model," Physics of Fluids, **A3**, pp. 1760-1765.

[13] Lilly, D. K., 1992, "A Proposed Modification of the Germano Subgrid Scale Closure Method," Physics of Fluids, **A4**, pp. 633-635.

[14] Yan Zang, Robert L. Street, and Jeffrey R. Koseff, 1993, "A dynamic mixed subgrid-scale model and its application to turbulent recirculating flows," Physics of Fluids A: Fluid Dynamics **5**, pp. 3186.

[15] Hong Zhao and Peter R. Voke, 1996, "A Dynamic subgrid-scale model for low-Reynolds-number channel flow," International Journal for Numerical Method in Fluid **23**, pp. 19-27.

[16] Kato, C., Kaiho, M. and Manabe, A., 2003, "An overset finite-element large-eddy-simulation method with application to turbomachinery and aeroacoustics," Transactions of ASME, Journal of Applied Mechanics, **70**, pp. 32–43.

[17] Kato, C., Yamade, Y., Wang, H., Guo, Y., Miyazawa, M., Takaishi, T. and Takano, Y., 2005, "Numerical prediction of sound generated from flows with a low Mach number," Computers & Fluids, **36** (1), pp. 53–68.

[18] Fambri, F. and Dumbser, M., 2016, "Spectralsemi-implicitandspace–time discontinuous Galerkin methods for the incompressibleNavier–Stokes equations on staggered Cartesian grids," Applied Numerical Mathematics **110**, pp. 41–74.

[19] Lele, S. K., 1992, "Compact Finite Difference Schemes with Spectral-like Resolution," Journal of Computational Physics, **103**, pp. 16-42.

[20] Yamanishi, N., Fukao, S., Qiao, X., Kato, C., and Tsujimoto, Y., 2007, "LES Simulation of Backflow Vortex Structure at the Inlet of an Inducer," Journal of Fluids Engineering, **129**, pp. 587-594.

[21] Pacot, O., Kato, C., Guo, Y., Yamade , Y., and Avellan, F., 2016, "Large Eddy Simulation of the Rotating Stall in a Pump-Turbine Operated in Pumping Mode at a Part-Load Condition," Journal of Fluids Engineering, **138** (11), pp.111102-1-111102-11.

[22] Makihara, T., Kitamura, T., Yamashita, T., Maeda, K., Kato, C., Takayama,T., Yamamoto,K, Yamade , Y., and and Suzuki, Y., 2016, " Identification of Vortical Structure that Drastically Worsens Aerodynamic Drag on a 2-Box Vehicle using Large-scale Simulations," SAE Int. J. Passeng. Cars - Mech. Syst. **9** (2): doi:10.4271/2016-01-1585.

[23] Yamashita, T., Makihara, T., Saito, Y., Kato, C., Takayama, R. Takayama, T., and , Yamade , Y., 2018, "Effects of Moving Ground and Rotating Wheels on Aerodynamic Drag

of a Two-Box Vehicle," SAE Int. J. Passeng. Cars - Mech. Syst. **11**(5), pp. 415–428, doi:10.4271/2018-01-0730.

[24] Nishikawa, T., Yamade, Y., Sakuma, M., Kato, C., 2013, "Fully Resolved Large Eddy Simulation as Alternative to Towing Tank Resistance Tests- 32 Billion Cells Computation on K computer," 16th Numerical Towing Tank Symposium (NuTTS'13), Duisburg, Germany.

[25] Nishikawa, T., Yamade, Y., Sakuma, M., Kato, C., 2012, "Application of Fully-resolved Large Eddy Simulation to KVLCC2 －Bare Hull Double Model at Model Ship Reynolds Number-," Journal of the Japan Society of Naval Architects and Ocean Engineers, 16, pp. 1-9.

[26] Akiyama, O. and Kato, C., 2017, "Numerical Investigations of Unsteady Flows and Particle Behavior in a Cyclone Separator," Journal of Fluids Engineering, **139**, pp. 091302-1-091302-11, doi: 10.1115/1.4036589.

[27] Howarth, L., 1938, "On the solution of the laminar boundary layer equations," Proc. Roy. Soc. London A, **164** pp. 547–579.

[28] Burgers, J. M., 1948, "A mathematical model illustrating the theory of turbulence," Advances in Applied Mechanics, **1**, pp. 171-199.